The Physics of Condensed Plasmoids (CPs) and Low-Energy Nuclear Reactions (LENR)

Lutz Jaitner, February 2020, lutz.jaitner@t-online.de, www.condensed-plasmoids.com

Abstract

LENR researchers have long been puzzled about the basic questions: How can nuclei fuse at low temperature, i.e. how can they overcome the Coulomb barrier without having high kinetic energies? Why is the observed excess heat not accompanied with gamma radiation? Why is LENR producing helium-4 from deuterium, whereas D-D hot fusion is mainly producing helium-3, tritium, protons and neutrons? How can LENR be technically optimized for commercial use?

To answer these questions, the author has built a quantum-mechanical model of the nuclear active environment in LENR. This environment is an ultra-dense plasmoid, i.e. a "condensed plasmoid". The computed properties of CPs are so exotic that CPs qualify as a previously unknown aggregation state of matter.

This document is first in describing the properties of CPs, the microscopic evidence of CPs in LENR experiments, how the properties of CPs help explaining a wealth of remarkable findings in LENR experiments, examples of nuclear reaction routes possibly enabled by CPs, the quantum-mechanical model of CPs, the computational results derived from this model, verifiable predictions derived from the theory on CPs and a technology assessment on potential dangers of LENR. The mechanism, which suppresses gamma radiation in CPs, will also be described in this document.

The quantum-mechanical model of CPs is based on the cylindrical symmetry of a very thin (i.e. about 40 pm) plasma "wire" (The quantitative properties given in the abstract are depending on the configuration of the CP; these are just examples). The electrons of a CP are fully delocalized and decoupled from the nuclei. They are moving with high velocity (10 to 80% of light speed) against the nuclei. This results in an intrinsic current of about 9 kA in the CPs, with a mean current density of approximately 2.5 A per square picometer.

The magnetic field from this current reaches 50 megatesla and creates a confinement pressure of more than 10^{21} Pa. The electrons are compressed by a z-pinch condition to a mean density of about 0.15 electrons per cubic picometer.

The creation of a CP is an endothermic process (i.e. it takes in energy from an external source), which typically requires discharges with high voltages and high currents. Once created, CPs enjoy a lifetime, which can extend to hours and beyond. This longevity is likely not a result of the CP's stability, but is rather based on a self-sustained feedback of nuclear energy, countering the otherwise inevitable decay of the CP.

The minimum distance of hydrogen nuclei in a CP is only about 2 pm, which enables tunneling through the Coulomb barrier. The barrier is also much screened by the dense electrons.

Nuclear energy feedback to the electrons can potentially produce a negative resistivity of sparks and a self-sustained growth of CPs. This can lead to high-voltage oscillations in the electrodes and a dangerous and sudden release of nuclear energy, if the electrode circuitry is not damped resistively and the reaction rate is not properly fuel-limited.

Table of Content

Table of Figures

Table of Tables

1 General Description

1.1 Definition, Topologies

The term "condensed plasmoid (CP)" is coined in this document for the first time, thus a definition is given here. A CP is defined to be a plasmoid (i.e. a self-consistent structure of a current-carrying plasma and magnetic fields), which is meeting all of the following criteria:

- The plasmoid is compressed by a strong z-pinch condition. "Strong" in this sense means that the internal current is larger than 200 A, the radius of the plasma channel is less than 200 pm and the length of the plasma channel is at least several micrometer. These numbers are based on the computational results of the current modeling. For yet unknown reasons CPs might exist with lower intrinsic currents.
- All electrons of the containing atoms (not merely the outer electron shells) are delocalized, i.e. the electrons are all contributing to the current and they can freely move between the atomic nuclei. The delocalization is caused by the small inter-nucleic distance (i.e. less than 10 pm in case of hydrogen).
- The electrons are residing in orbitals, which are at (or near) the quantum-mechanical ground state of the CP. For this to be true, the temperature of the CP must be low enough that the thermal pressure of the plasma is smaller than the magnetic pressure enforced on the moving electron gas by the Lorentz force.

A direct consequence of this definition is that CPs are representing mesoscopic objects of matter. "Mesoscopic" means "in between quantum-mechanical and macroscopic". The properties of CPs therefore do not always follow the conventional wisdom of plasma physics. For example, cooling down a CP will not produce electron-ion recombinations and ordinary molecules.

CPs exist in different topologies:

- The open-ended configuration of a CP exists under transient conditions in the presence of a strong electric field. An open-ended CP loses electrons at the negative end. The positive end of an open-ended CP is often connected to a cathode, which replaces the electrons lost at the other end.
- The closed-loop configuration of a CP is the long-lasting form, where the internal current is flowing in a circular manner. Closed-loop CPs can exist even in absence of an external electric field. Based on the microscopic evidence, there are various mechanisms by which closed-loop CPs can develop. These mechanisms are typically supported by the electrostatic attraction between the electrons and the cations. The positive and negative charges will rapidly find a path to meet if the loop is not yet closed. Along this path the plasmoid then condenses. Another mechanism would be, if a CP is spawning a closed loop by overlapping with itself.

1.2 Historic Terms

CPs have been observed/described numerous times in physical experiments and in nature during the course of the last hundred years. They have been called by many different names:

- Large natural occurrences of CPs are called "**ball lightning**", as they are sometimes accompanying thunderstorms. These CPs are in a closed-loop configuration.
- CPs also occur as "**Precursors**" (aka "**leaders**") in lightning. These are very long, relatively slowly expanding objects, which are opening a conductive channel before the main discharge of a flash of lightning runs through. The conductive channel is commonly believed to be just a collection of ions. In reality, the channel is consisting of

an open-ended CP (or a bundle of several CPs). The author recommends viewing them in a slow-motion video [2], because this is very revealing for the understanding of CPs.

- Winston H. Bostick in his research on magnetically pinched high-current plasmoids discovered filamentary structures, which he called "**vortex filaments**" (aka "**current filaments**" in plasma focus devices). These filaments were open-ended CPs. Bostick was puzzled by these objects, because their electron concentration violated the space charge law, because they were able to bore holes through exposed materials (metals, dielectrics), and because they could explode with large force.
- Building upon the work of Bostick, Ken Shoulders were intensely experimenting with CPs and describing their properties in great detail. Shoulders called these objects "**EVs** (*electrum validum*)", "**EVOs** (exotic vacuum objects)", or "**high-density charge clusters**" [1] [2].
- Takaaki Matsumoto observed and photographed "ball-lightning-like" objects in LENR electrolysis experiments. These objects were closed-loop CPs. He called them "**Ring clusters**". He observed that CPs can penetrate glass walls and can transmute elements.
- Irina Savvatimova and B. Rodinov exposed x-ray films inside and outside of the reaction chamber during high-current glow discharge LENR experiments. The films showed very peculiar patterns. Some of them had the helical shape, which is so characteristic of CPs. The objects causing the patterns apparently were able to penetrate the 5mm-thick steel walls of the chamber. Savvatimova and Rodionov published in 2005 [6] patterns on the surface of the palladium cathodes exhibiting similarities with the structures seen on X-ray films. Leonid Urutskoev found similar patterns on nuclear emulsions several meters away from a sealed reaction chamber housing a titanium foil explosion experiment. The same type of patterns were found, when the emulsion was exposed to the debris of the foil explosion up to 24 hours after the experiment. The said patterns have been called "**Caterpillar tracks**", "**strange radiation**", "**Urutskoev tracks**", or "**magnetic monopoles**" in the literature.
- Mark L. LeClair and Sergio Lebid discovered that reentrant jets from the collapse of cavitation bubbles have hexagonal facets and possess tremendous electrostatic charge. They were calling these objects "**water crystals**". The leading end of the jets was found to be positively charged and the tail was negative, allowing the jet to form observed closed loops. They found that the jets were causing all sorts of transmutations, emitting x-rays, carving long trenches in high melting point ceramics (e.g. aluminum oxide) and removing far more material than could be accounted for by the kinetic energy of the jets. Remnants of these objects were causing tracks on plastics surfaces, which provided microscopic evidence for CPs.
- A. Klimov analyzed hydrogen-containing plasmoids and found CPs, which he called "**erosive metal clusters**" [31]. His advanced documentation contains pictures of the CPs, the erosion pattern at the cathode, material deposition on the anode, optical emission spectra, x-ray emission spectra of CPs and more.
- Gennady A. Mesyats called them "**Ecton processes**", when describing the fast processes at the cathode during vacuum discharges [54].
- CPs are called "**Cathode spots**" in vacuum discharge research.

CPs were historically called by many more names. They have played a key role in experiments with underwater arc explosions, dusty plasma, and high-current glow discharge, among others. A more comprehensive collection of historical experiments involving CPs can be found at the author's web site [19].

1.3 Creation of CPs, Condensation of a Z-Pinched Plasmoid

There are two known ways of producing CPs with high reproducibility: Electrical discharges and cavitation. Both phenomena involve the creation of plasmoids, which then condense to a CP.

Cavitation forms plasmoids, when the reentrant jet of collapsing bubbles hits materials at supersonic speed. During the impact matter is ionized and electrons are stripped from atoms, leaving cations. The electrons tend to decelerate quicker than the created cations, leading to a strong current through plasma, i.e. a plasmoid is forming.

However, not all plasmoids will readily condense. For example, an electric arc (driven by DC or AC current) is often too hot and the ionized channel is often too wide for the condensation to take place. The continuing current is heating the plasmoid by resistive losses in the plasma, which negatively affects the ability of the plasmoid to condense.

In order of a z-pinched plasmoid to condense, several conditions are instrumental:

- The current pulse should be very short, i.e. less than a microsecond in duration.
- The current needs to be strong enough, i.e. more than several hundred amps.
- Elements with large Z should be present in the plasma channel, because they increase both Bremsstrahlung and X-ray line radiation as a cooling mechanism during the condensation phase
- The plasmoid should be cooled, i.e. by running the discharge along a dielectric surface or under water.

- Dense matter should be available, which can rapidly feed the forming plasmoid. Typically either the cathode, or the surrounding gas or the dielectric surface will supply the matter that forms the plasmoid.
- A magnetic field in parallel to the electric field will steer the electrons in the right direction

If the above conditions suffice, the plasmoid will condense. The condensation is promoted by the radial pressure of the magnetic field.

The azimuthal component of the magnetic field at the surface of the plasmoid is inversely proportional to the radius of the conducting channel. Therefore, the more the magnetic field compresses the plasmoid, the stronger the magnetic field becomes and the stronger the plasmoid is compressed. It's a **positive feedback mechanism**: When the current divided by the plasmoid radius increases beyond a critical threshold, there will be a rapid compression of the plasmoid.

If the temperature is kept low enough, only **the degeneracy pressure of the electron gas will hinder a total collapse of the matter**. The degeneracy pressure is a quantum-mechanical result of the Pauli Exclusion Principle. It increases with increasing electron density.

The main idea of this theory on CPs is as following: A quantum-mechanical model of CPs had to be established in order to compute the equilibrium radius (and other properties) of a CP (This is referring to the equilibrium between the magnetic pressure and the quantum-mechanical pressure of the electron gas). The scope of the model is to describe the stationary state after the compression of the plasmoid, rather than modeling the dynamic aspects of the compression.

The **formation of a CP is an endothermic process**. Therefore, CPs will never form spontaneously. There is always energy required from external sources (e.g. an electric discharge) to accelerate at least hundred million electrons to collinear movement, before a CP can form.

A bigger part of the energy from the electric discharge will be stored in the CP as kinetic energy of the electrons. Another part of the energy will create broad-band emissions of electromagnetic radiation. The radiation is the result of electron relaxation (i.e. the electrons are entering orbitals with the lowest possible energy). The spectrum is broad-band (i.e. it is not based on sharp lines), because the electrons are fully delocalized and densely packed.

During condensation the matter density increases dramatically and the scattering probability of the electrons decreases to almost zero. Electron scattering in CPs differs from electron scattering in ordinary plasmoids by the fact that most of the lower-energy orbitals of CPs are already occupied and there is no energy available for scattering electrons into higher-energy orbitals. In result, the resistivity of the CP drops to levels very close to zero (this phenomenon is not necessarily related to superconductivity).

The behavior of high-current plasmoids under z-pinch conditions has been studied intensely over the course of the last 80 years in conjunction with dense plasma focus devices and other experiments (e.g. electrical explosion of thin wires).

Initially thought out as a concept for hot fusion research, the resulting plasmoids in plasma focus devices show clear evidence of condensation to CPs: From the viewpoint of conventional plasma physics the plasma current sheaths in these devices should be homogeneous in azimuthal direction. In reality however, the current sheaths are inhomogeneous and have a filamentary structure [33] [44]. Each plasma filament seems to carry currents in the order of tens to hundreds of kiloampere. The filaments are known to have a helical sub-structure and are producing an axial magnetic field component, similar to CPs.

1.4 Radiative Collapse of a Pinched Plasmoid in Light of Plasma Physics

It was derived by W. H. Bennett in 1934 [47] that there is an equilibrium between the thermal pressure of a plasma channel and the magnetic pressure of a pinched plasmoid, if the so called Bennett relation is met:

(1) $k_B\left(N_e T_e + N_i T_i\right) = \frac{\mu_0}{4\pi} I^2$, where N_e is the number of electrons per unit length of the plasma channel, N_i is the number of ions per unit length of the plasma channel, I is the total current, μ_0 is the vacuum permeability, k_B is Boltzmann's constant, T_e is the electron temperature and T_i is the ion temperature

This relation assumes that the velocity distribution of the electrons and ions obey the Boltzmann statistics of an ideal gas. This assumption is invalid in case of CPs, because their plasma is fully degenerate (Fermi gas) and the temperature is low.

The possibility of radiative collapse in pinched linear discharges was first studied independently by Pease [48] and Braginskii [49] [50] in 1957 for pure hydrogen or deuterium plasmas. When radiation losses by bremsstrahlung are exceeding Ohmic heating at high currents, they predicted shrinking of the plasma channel, which may even result in a collapse of the channel to extremely high densities. They derived a critical current value (i.e. the Pease-Braginskii current) that has to be exceeded for achieving a collapse:

(2) $\frac{I_{PB}}{MA} \approx 0.27\sqrt{\ln\Lambda}\left(1+\frac{1}{Z}\right)$, where $\ln\Lambda$ is the Coulomb logarithm, MA stand for megaampere and Z is the charge of the ions

Formula (2) is assuming an infinitely long plasma channel and $T_e = T_i$. It is based on Spitzer resistivity (first formulated by Lyman Spitzer [51] in 1950), where the resistivity of the plasma channel is proportional to $T_e^{-3/2}$.

There were many later attempts in the literature to refine the original formula of Pease and Braginskii, but the issues at low temperatures were not addressed, as far as the author is aware of:

Spitzer resistivity is built upon classical electron-ion collisions (this can be seen as a high-temperature approximation), whereas at low temperatures the scattering behavior of the electrons can only be understood by a quantum-mechanical analysis. With Spitzer resistivity one would conclude that the plasma channel becomes non-conductive (and Ohmic losses would diverge) when the temperature approaches zero. In reality the resistivity of a CP is the lowest at the lowest temperatures. The physical reason for this discrepancy is that electron-ion scattering is energetically hindered at low temperatures in CPs. Instead the resistivity of a CP is mainly based on electron-phonon scattering, which also becomes negligible at very low temperatures.

Also, the Pease-Braginskii formula is merely considering Bremsstrahlung as the cooling mechanism, where in reality line radiation of heavier atoms, heat transport by delocalized electrons, stimulated cyclotron radiation, and direct thermal conduction to the environment are contributing to the cooling during the condensation phase.

The Pease-Braginskii current is typically computed as being in the order of 1.5 MA for hydrogen. It decreases to about 100 kA for elements like Ar, Kr and Xe, because line radiation dominates over Bremsstrahlung and the radiative cooling thus becomes more efficient.

With peak currents in the range of 150 - 200 kA evidence for radiative collapse has been found [52]: Low-inductance vacuum sparks produced by discharging a capacitance of 10 - 30 μF (charged to 10 - 20 kV) through a circuit inductance of 50 - 100 nH achieves pulse lengths of 1.5 - 2 μs. The sparks are producing small, pointlike regions in the plasma that are called plasma points, bright spots, or hot spots (Similar observations have been made in plasma focus devices and in gas puffs).

The first phase of the discharge is creating the plasma with material eroded from the electrodes. In the next phase of the discharge the current increases as prescribed by the electrode voltage and the inductance of the circuit. On top of the smoothly rising current there appear short (< 100 ns) single or multiple dips in the current. These current dips are accompanied by intense bursts of x-rays with photon energies of 5 - 150 keV. The current dips are correlated with the appearance of plasma points. The points are often less than 10 μm in size.

It is remarkable that the maximum x-ray photon energy is much higher than the theoretical maximum energy of the electrons traversing the electric field between the electrodes. The maximum photon energy also exceeds the K-shell energy of the plasma ions. These high photon energies can be explained by electron relaxation in CPs, which have a Fermi energy (i.e. the energy difference between the highest and the lowest occupied orbital) of up to 200 keV.

The observed current dips can be interpreted as the condensation phase of the CPs: When the radius of the CPs is shrinking the magnetic flux of the CPs is compressed. This is electromagnetically inducing a high voltage counter to the externally applied voltage. During the current dips compression work is applied to the CPs by means of the external field. At the end of the compression phase (i.e. the end of the current dip) the current continues to rise and the generated CPs continue to exists, but the electron relaxation is mostly complete and the x-ray emission fades.

The fact that sometimes multiple current dips have been observed during the same discharge can be interpreted to mean that several CPs have been created in parallel, which successively condensed. This could be due to a filamentation instability of the initial plasmoid.

J. Va'vra *et al.* determined the smallest possible spark current, which is still consistent with the X-ray production and the development of plasma points [53]. Their generator used a spark gap operating at low pressure (0.1 to 1 Torr) and low discharge voltages between 0.8 and 2.1 kV. The charging capacitance was 75 nF, the circuit inductance was about 1000 nH, the stored energy amounted to 0.024-0.17 J per pulse, the peak spark currents was 200 - 500 A and the total capacitor charge was between 4×10^{14} and 10^{15} electrons. The spark gap was 1 mm.

The observed X-ray energies were between 2 and 10 keV even at the lowest sparking voltage of about 0.8 kV (depending on the gas). The maximum observed X-ray energy (~10 keV), generated at the lowest voltage (~0.8 kV), is above K-shell energy of typical gases used in the tests, and materials used in the spark electrodes. The X-ray production persisted even for the carbon electrodes which have the smallest K-shell energy (0.284 keV).

The spark current and the electrode voltage were measured as following:

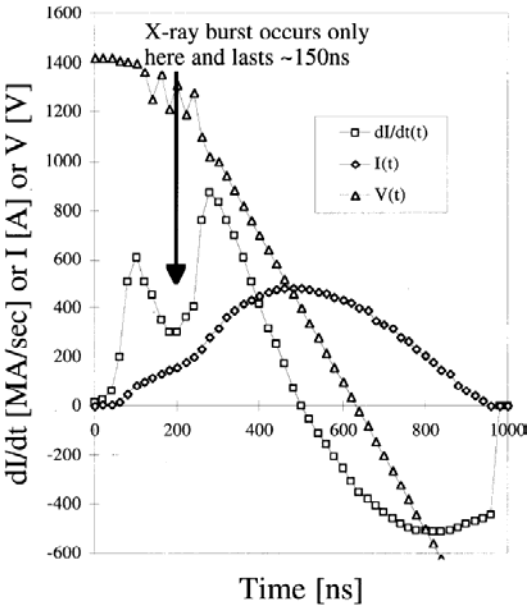

Figure 1 Current and voltage develpopment in a low-pressure spark discharge according to J. Va'vra *et al.* [53]

The radiative collapse of the plasmoid (which can be equated with the condensation of a CP) occurred during the dip of the dI/dt(t) curve, which lasted about 150 ns. It is very interesting that this collapse occurs already at a current of about 200 A.

1.5 Main Properties of CPs

This chapter is based on a combination of experimental findings from other researchers and theoretical conclusions from the theory on CPs. Reasons are provided, where they are related to the theory, but some proof points from external references were omitted, as to not convolute this general description.

CPs can exist in many different configurations. The configuration of a CP mostly depends on the conditions during the creation of the CP. For example, the length, the magnetic flux, the internal current, the formation energy, the density, the total charge, the axial velocity of the electrons, and the elemental composition all depend on the initial conditions.

After their creation CPs can change their configuration only slowly, because the magnetic flux is preserved in CPs due to a lack of resistive losses.

CPs are at least five orders of magnitude longer than their radial extent. In some cases, CPs can fork their channel and rejoin the branches after some distance. Several CPs can bundle together, attracted by magnetic forces.

CPs in an open-ended configuration are emitting fast electrons at their negative end with kinetic energies up to tens of keV. Open-ended CPs are also luminous, i.e. they are emitting bluish-white light, UV radiation and other frequencies.

CPs in a closed-loop configuration can be dark, depending on their temperature and configuration. Closed-loop CPs can absorb light, i.e. they can really look dark or grey [13]. If closed-loop CPs are heated up (e.g. by internal nuclear reactions), they become luminous, i.e. they will emit fast electrons, bluish-white light, UV radiation and other frequencies.

Closed-loop CPs can suddenly break into pieces. These fragments will temporarily be in an open-ended configuration. The fragments can shoot with high speed several meters through the air (dangerous!). One reason for this sudden acceleration is the high axial velocity of the electrons: Electrons will shoot out of the negative end, forming an electron cloud, which attracts ions. The cloud with the ions then re-condenses, extending the CP towards the negative end. The ions left devoid of electrons at the positive end will flow along the CP to reach the negative end. This process in effect looks like the CP is moving with high speed in the direction pointed to by the negative end.

There is a minimum length of a CP, which is believed to be a few micrometers. Based on this length CPs contain at least hundred million electrons.

There is no maximum length, i.e. CPs can be made arbitrarily long.

In the following, ranges of values are specified for some of the properties. These ranges correspond to a range of the linear nuclear charge density λ_n from 100 to 600 elementary charges per picometer. With the current modeling there is uncertainty, which density is representing the most stable configuration of CPs, see chapter 5.4.

The radius of CPs ranges from 130 pm through 35 pm, depending on configuration.

The mean expectation value of the electron density inside CPs is in the range of 0.003 per cubic picometer through 0.2 per cubic picometer, depending on configuration. For the highest-density configurations this translates to a matter density, which can be hundred thousand times higher than the density of ordinary matter. In the highest-density configurations hydrogen nuclei can come closer than 2 pm distance (statically).

Forming a CP is endothermic, requiring from 10 keV to 120 keV of energy per electron.

The total intrinsic current of a CP ranges from 800 A through 12 kA, depending on configuration. This translates to current densities of up to 4.5 A per square picometer for the highest-density configurations.

The mean axial velocity of the electrons (relative to the nuclei) is 16 to 40 percent of the speed of light, depending on configuration.

The maximum strength of the magnetic field ranges from 1.4 to 75 MT (megatesla), depending on configuration. This field creates a magnetic pressure of up to $5 \times 10^{21} Pa$ for the highest-density configurations. This pressure is five orders of magnitude higher than the pressure in the middle of the solar core!

The dense electron gas is strongly screening the Coulomb potential of the nuclei inside of a CP. The author used Thomas-Fermi screening and a CP configuration with a mean electron density of 0.15 electrons per cubic picometer to compute the following numbers:

- The screening length is about 5.5 pm
- The screening potential for protons is about 250 eV. For palladium nuclei it is about 12 keV.

The lifetime of CPs ranges from milliseconds to tens of hours, depending on environmental conditions.

The number of electrons in the core of a CP exceeds the number of nuclear charges by several percent. The excess negative charge of the core is often compensated by a “halo” of cations surrounding the core of the CP. The strength of the electrical field between core and halo can exceed thousand volts per picometer.

The minimum electric potential of the CP core is in the range of -7 to -60 kV. Electrons leaving the core will be accelerated away from the core. This way, they can reach kinetic energies of up to tens of keV. Interaction of these fast electrons with surrounding matter will cause broad-band bremsstrahlung and significant levels of ionization outside of the halo zone. The recombination of ions with electrons from this ionization is causing x-rays and light emission, exhibiting the line spectrum of atoms/molecules.

The measurable energy of the electrons emitted from a CP depends not only on the electric potential of the CP core, but also on the energy losses occurring in the halo and the surrounding matter. Experimentally, electron energies from about 2 keV to 10 keV have been reported [1] [2].

In contrast, nuclei leaving the core will be attracted by the core. They will recombine with electrons in the vicinity of the CP and can thus hardly be detected as free particles (Ken Shoulders falsely concluded from the lack of detectable ions that the EVs/CPs almost entirely consist of electrons).

The high electric field between core and halo is capable of ionizing matter in the vicinity of the CP and re-condensing it at other places. This ionization is non-thermal and non-dissipative (i.e. it consumes no energy). The effect of this is that all sorts of material can be “etched away” and be re-deposited by a CP. From the amount of etched material one should not falsely conclude, how much energy the CP was providing to “melt/evaporate” the material, because the ionization energy is recycled upon re-condensation. In reality, ionization and re-condensation are two sides of an equilibrium reaction.

There are also two other ionization mechanisms occurring at CPs, which are non-thermal, but dissipative: Fast electrons and x-rays emitted by CPs will cause ionization in the surrounding matter. These emissions are non-nuclear and have energies up to tens of keV. According to the spallation hypothesis (see chapter 1.10) there are emissions of spallation/fission products, i.e. protons, alpha particles and heavier nuclei with energies up to some tens of MeV. This is another source of ionization, which has a nuclear origin.

The ionizing and re-condensing capability of CPs is responsible for one of the most perplexing properties of CPs: CPs are able to bore holes several millimeters deep through even the hardest materials. Thus CPs can escape all sorts of enclosures. This is rather problematic, because CPs are harmful to biological tissue and pose a serious health risk. Thin-walled vacuum chambers will probably leak gas after intense exposure to CPs.

However, there are methods of shielding available, which are based on the magnetic properties of CPs: The high intrinsic current of CPs creates a large magnetic moment. Magnetic materials (preferably iron below its Curie temperature) can trap CPs, providing an effective shield. After several days CPs trapped in an iron shield will have decayed and ceased to exist.

The shielding properties of various materials are often counterintuitive: CPs pass most easily through porous materials, such as cardboard and porous ceramics, because CPs "like" to follow thin pores and tiny cracks. Even thick layers of porous materials will not stop CPs. The shielding efficiency is often not increasing exponentially (i.e. less than exponentially) with the thickness of the shield, as would be expected for corpuscular radiation. In fact, a batch of many thin layers of an electrically tight insulator interspersed with thin metal foils have a much higher shielding effect than a homogenous sheet of insulator with the same aggregate thickness. A strong electric field perpendicular to a sheet of an insulator will either weaken or strengthen the shielding effect, depending on polarity. Neither the hardness, nor the density, nor the melting point of the shield correlates well with its shielding effect. Hydrogen-rich materials (e.g. plastics) may under certain conditions boost CPs, rather than shielding against them (dangerous!).

The high electric field between core and halo is also responsible for the preference of CPs for surfaces: CPs often electrostatically attach to surfaces and run along surfaces (also in thin cracks and capillaries). This way, some of the cations of the halo can be replaced by polarization charges at the surface, whereby the total energy of the CP is lowered.

Ken Shoulders expressed the preference of CPs to surfaces in the words: *"I found the demon EV* [i.e. a CP] *loved to run in grooves and hide in cracks, the smaller the better. It even prefers running in totally enclosed structures, such as in tubes and between plates, to running in the open. At this point I was convinced EVs were female because of the way they are always looking at their mirror image* [i.e. the induced charge] *in dielectrics."* [2]

Most of the electromagnetic radiation observable in LENR is stemming from the electrons of CPs, rather than from excited nuclei. Electron transitions between orbitals of CPs are causing the characteristic broad-band emissions of CPs with high intensity in the soft-X-ray and vacuum UV ranges. The emission are broad-band (i.e. no line spectrum), because of the high electron density and the delocalization of the electrons.

The axial kinetic energy of the electrons in CPs is up to 100 keV. If the current flow of a CP is suddenly disrupted, the axial kinetic energy of the electrons will be released to the environment. In this case the CP will explode with an audible "bang". Time-correlated with this bang, there will be an intense flash of bremsstrahlung (maxing out at about 100 keV), light emission, x-ray emission, and radio frequency emission. The latter is stemming from the fact that the magnetic moment of the CP suddenly "dies".

When a CP is approaching the anode of a discharge gap, three very different outcomes can happen:

- In the first possible case, the CP electrically connects with the anode, a current from cathode to anode is flowing through the CP, much of the kinetic energy of the electrons and much of the matter inside the CP core is dumped on the anode. The CP is destroyed in this process. As microscopic evidence for this outcome, one can observe little droplets of cathode material deposited by the CP on the surface of the anode.
- In the second possible case, the CP will not connect electrically with the anode. This can happen, if the CP has already disconnected from the cathode and is now in a closed-loop configuration. The CP can then attach itself to the anode for some time. The microscopic evidence will be the edging damage ("track" or crater), which the CP leaves on the surface of the anode.
- In the third case, the CP prior to having contact with the anode will "spray" so many electrons on the anode that its electric potential reverses. The CP is then electrostatically repelled from the anode and changes course in some other direction, e.g. returning to the cathode. This "funny behavior" of CPs to miss the anode has been observed by Ken Shoulders many times.

Commonly used detectors for radioactive radiation are also sensitive to CPs. In fact, CPs can easily be confused with radioactivity. The latter has happened a number of times in conjunction with the interpretation of LENR experiments in the literature.

For example, CPs are leaving tracks in the Wilson cloud chamber. They are producing patterns in x-ray films and nuclear emulsions, although these patterns look different from those caused by elementary particles. CPs are also creating pulses in a Geiger-Müller tube, but they might disable the tube for a while due to continuous ionization (the window of a Geiger-Müller tube will become leaky after passage of a CP, which permanently damages the tube). CPs are creating patterns in CR-39 nuclear track detectors, although these patterns look different from those caused by elementary particles. The patterns from CPs can sometimes been seen in the microscope, before the CR-39 has been developed in alkaline solution. CPs might cause light pulses in scintillation detectors and fluorescence screens, but these pulses can be longer-lasting. Also, the scintillation detectors might be damaged by CPs.

CPs are chemically very active. The effect of this activity can be compared to bombarding the surrounding material with an electron beam or an ion beam. Chemical bonds will be randomly broken by CPs, many free radicals will be

created, new bonds will be formed, and energetic compounds can be created, e.g. ozone, nitric oxide and hydrogen peroxide. Moist air, which was exposed to CPs, has a characteristic acid-fresh smell, a bit like nitrous acid.

1.6 Secondary Structure

The primary structure of CPs has a cylindrical shape, i.e. it is a plasma "wire", which is long, very thin and rotational symmetric. Most, but not all, properties of CPs can be derived from the cylindrical model, i.e. the primary structure.

The ultra-strong magnetic field of CPs is deforming the plasma-wire, leading to a secondary structure: CPs are tending to coil up in two-layered closed-loop solenoids as following:

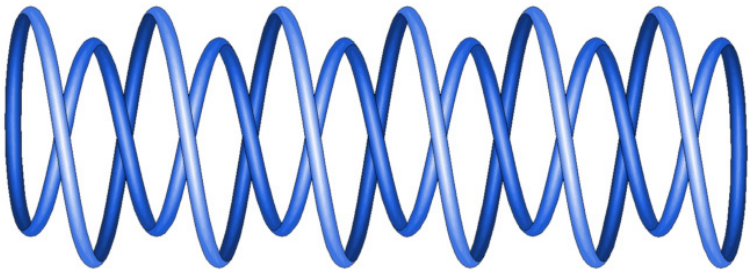

Figure 2 Drawing of a CP coiling up in a two-layered closed-loop solenoid via magnetic self-interaction

In reality, there are many variances of this basic solenoid structure. The variances are often the result of CP interaction with solid surfaces (see chapter 2).

Open-ended CPs are also tending to coil up, in this case to a single-layer solenoid structure.

The secondary structure has important consequences:

- There is a magnetic field component in direction of the solenoid axis (with a strength of up to about 1 kT). This field component provides a strong magnetic dipole moment to the CP, which can interact with external magnetic fields. In open-ended CPs the secondary structure creates a magnetic field component in parallel to the external electric field.
- CPs are attracted by magnets, i.e. they behave like ferromagnetic material. CPs tend to increase the strength of an externally applied magnetic field, like ferromagnetic material does. CPs can maintain their pseudo-ferromagnetic behavior well above the Curie temperature of all known ferromagnetic materials.
- Electric energy can be transferred by electromagnetic induction between CPs and an external magnetic coil. A sudden increase of the electric current in the coil will reduce the current in the CPs, which is potentially destroying them. A sudden decrease of the electric current in the coil will enlarge the current in the CPs, which is helping them to grow.
- There is an electron velocity component perpendicular to the solenoid axis. This was already experimentally evident to Winston Bostick, which is why he called these objects "vortex filaments". In open-ended CPs the electrons move (paradoxically) mostly perpendicular to the external electric field. The length of the plasma wire between cathode and anode is much prolonged by the solenoid structure.

The helical structure of CPs is quasi-periodic. As such, it strongly influences the lobe and direction of electromagnetic emissions. CPs with enough excited electrons can behave like a free-electron x-ray laser: The quasi-periodic structure of CPs (acting like an "undulator") amplifies the emission of radiation by constructive interference and collimates the beam towards the axis of the CP. The radiation stimulates the simultaneous emission from many electrons, i.e. short, intense bursts of coherent x-ray emissions can occur (this has been observed by Alexander Karabut [9]).

The axes of the CPs are aligning in parallel to externally applied magnetic fields. In this case, the laser pulses are directed in parallel to the magnetic field lines.

1.7 CPs as the Nuclear-Active Environment of LENR

The term "nuclear-active environment (NAE)" has been coined by Edmund Storms [5] in an attempt to characterize the location and chemical composition of the zone, where the nuclear reactions of LENR actually happen.

Based on experimental evidence Edmund Storms found out that:

- The reaction occurs in the surface region of the heat-producing material, rather than in the bulk
- The reaction is not happening in beta-PdD, as other researchers were assuming

The concept of a NAE is useful, because transmutations observed in LENR experiments were always occurring in "hot spots", rather than being uniformly distributed in the material. So, the environment in these spots must be somehow different from the rest of the volume.

Taking this concept to the next step, the NAE is equated here with CPs. This way, some of the most peculiar features of LENR (e.g. overcoming the Coulomb barrier at low temperatures, lack of gamma radiation) can be traced back to the environment, in which the nuclear reactions occur.

This will be done in the following in a qualitative manner. More research is required for backing these claims with quantitative analysis.

1.8 Coulomb Tunneling Hypothesis

It is known from muon-catalyzed fusion that the distance between two hydrogen nuclei bound by an electron and a muon is about 0.5 pm. This is about one fourth of the shortest distance between hydrogen nuclei achievable in CPs.

In muon-catalyzed fusion it takes only about half a picosecond, before hydrogen nuclei of a muon-electron-bound d-t-molecule fuse by tunneling through the Coulomb barrier. The quantum mechanical tunneling probability depends roughly exponentially on the average separation between the nuclei. This can be used to estimate the tunneling rate of nuclei (not merely hydrogen) in CPs. However, a quantitative analysis of the tunneling process is beyond the scope of this document.

As a hypothesis it is assumed here that the tunneling probability between adjacent nuclei in a CP enables nuclear fusion of all sorts of elements, not merely D-D fusion. This is really "**cold fusion**", because the nuclei require no kinetic energy for passing through the Coulomb barrier.

Some examples for fusion via Coulomb tunneling are given here:

(3) $2\times{}^{2}H \rightarrow {}^{4}He + 23.85MeV$ (unlikely to occur due to spallation)

(4) ${}^{1}H + {}^{9}Be \rightarrow {}^{10}B + 6.59MeV$

(5) $2\times{}^{12}C \rightarrow {}^{24}Mg + 13.93MeV$ (less likely to occur due to spallation)

(6) $2\times{}^{14}N \rightarrow {}^{28}Si + 15.53MeV$ (less likely to occur due to spallation)

(7) $2\times{}^{16}O \rightarrow {}^{32}S + 16.54MeV$ (less likely to occur due to spallation)

(8) ${}^{4}He + {}^{12}C \rightarrow {}^{16}O + 7.16MeV$

(9) ${}^{4}He + {}^{28}Si \rightarrow {}^{32}S + 6.95MeV$

(10) ${}^{1}H + {}^{16}O \rightarrow {}^{17}F + 600keV$ (unlikely to occur), ${}^{17}F + e^{-} \rightarrow {}^{17}O + \nu_e + 2.76MeV$

(11) ${}^{4}He + {}^{16}O \rightarrow {}^{20}Ne + 4.73MeV$

(12) ${}^{1}H + {}^{27}Al \rightarrow {}^{28}Si + 11.58MeV$ (less likely to occur due to spallation)

(13) ${}^{1}H + {}^{28}Si \rightarrow {}^{29}P + 2.75MeV$ (unlikely to occur)

(14) ${}^{24}Mg + {}^{32}S \rightarrow {}^{56}Ni + 13.95MeV$, ${}^{56}Ni + e^{-} \rightarrow {}^{56}Co + \nu_e + 2.14MeV$,
${}^{56}Co + e^{-} \rightarrow {}^{56}Fe + \nu_e + 4.57MeV$

(15) $2\times{}^{28}Si \rightarrow {}^{56}Ni + 10.92MeV$, ${}^{56}Ni + e^{-} \rightarrow {}^{56}Co + \nu_e + 2.14MeV$,
${}^{56}Co + e^{-} \rightarrow {}^{56}Fe + \nu_e + 4.57MeV$

(16) ${}^{1}H + {}^{56}Fe \rightarrow {}^{57}Co + 6.03MeV$, ${}^{57}Co + e^{-} \rightarrow {}^{57}Fe + \nu_e + 0.84MeV$

(17) $^{1}H + ^{58}Ni \rightarrow ^{59}Cu + 3.42MeV$, $^{59}Cu + e^{-} \rightarrow ^{59}Ni + \nu_e + 4.80MeV$,
$^{59}Ni + e^{-} \rightarrow ^{59}Co + \nu_e + 1.07MeV$

(18) $^{1}H + ^{62}Ni \rightarrow ^{63}Cu + 6.12MeV$

(19) $^{1}H + ^{40}Ca \rightarrow ^{41}Sc + 1.08MeV$ (unlikely to occur), $^{41}Sc + e^{-} \rightarrow ^{41}Ca + \nu_e + 6.50MeV$,
$^{41}Ca + e^{-} \rightarrow ^{41}K + \nu_e + 0.42MeV$

(20) $^{4}He + ^{40}Ca \rightarrow ^{44}Ti + 5.13MeV$, $^{44}Ti + e^{-} \rightarrow ^{44}Sc + \nu_e + 0.27MeV$,
$^{44}Sc + e^{-} \rightarrow ^{44}Ca + \nu_e + 3.65MeV$

(21) $^{2}H + ^{105}Pd \rightarrow ^{107}Ag + 13.12MeV$

(22) $^{27}Al + ^{27}Al \rightarrow ^{54}Fe + 21.86MeV$

(23) $^{16}O + ^{48}Ti \rightarrow ^{64}Zn + 12.78MeV$

(24) $^{2}H + ^{48}Ti \rightarrow ^{50}V + 13.87MeV$

(25) $^{2}H + ^{50}V \rightarrow ^{52}Cr + 19.33MeV$

(26) $^{1}H + ^{48}Ti \rightarrow ^{49}V + 6.76MeV$, $^{49}V + e^{-} \rightarrow ^{49}Ti + \nu_e + 0.60MeV$

(27) $^{1}H + ^{49}Ti \rightarrow ^{50}V + 7.95MeV$

(28) $^{1}H + ^{50}V \rightarrow ^{51}Cr + 9.52MeV$, $^{51}Cr + e^{-} \rightarrow ^{51}V + \nu_e + 0.75MeV$

(29) $^{1}H + ^{51}V \rightarrow ^{52}Cr + 10.50MeV$

All nuclear reactions depicted in this document are merely examples. The examples are not meant to suggest that these reactions are more probable than other reactions not shown. However, these sample reactions were selected in many cases based on experimental findings. They may therefore be helpful for interpreting the outcome of various LENR reactions.

Reaction (22) may provide some insight, how the simple device of the Correas [20] [21] was able to produce electrical energy from just aluminum (with minute amounts of air). This reaction could become an interesting proof point for the Coulomb tunneling hypothesis, because the "fuel" consists of just one isotope (i.e. Al-27) and creates another element (Fe-54), which is easy to detect magnetically and chemically. The Fe-54 isotope has a low natural abundance and can easily be distinguished from natural iron. However, there is an alternative reaction route with the same fuel shown in (61), which produces chromium instead of iron.

Reactions (5), (6), (7) and (14) together might explain, why arcing between pure carbon rods in air can produce silicon and iron [25] (The actual reaction paths might be more complicated considering the spallation possibilities of (45), (46) and (47)).

Reaction (10) shows the hypothetical transmutation of oxygen by fusion with protium. This reaction is unlikely to occur in LENR because of the low energy output. If light water is the "fuel" of a LENR reactor, oxygen is the most abundant starting element available for creating heavier elements via fusion. This process is probably initiated by fusion with helium (produced by spallation, see chapter 1.10), as is depicted in equation (11), rather than by fusion with protium.

Consecutive fusion reactions of ^{20}Ne (from equation (11)) with protium are supposed to result in ^{21}Ne, ^{22}Ne, ^{23}Na, ^{24}Mg, ^{25}Mg, ^{26}Mg, ^{27}Al and ^{28}Si (After some of these fusion steps subsequent electron capture is letting the product flip back to the previous element). Experimental results from many different experiments and research groups are suggesting that this row of fusion reactions is accumulating the element silicon. This can be understood by the relatively small energy release according to equation (13), which makes further fusion to phosphorus unlikely.

Remarkably, also the elements ^{24}Mg and ^{27}Al are showing up more abundantly in LENR "ash" than other elements. This is supposedly caused by reaction (48), which is producing ^{24}Mg instead of ^{28}Si. Therefore the protium fusion chain

oscillates several times between magnesium and aluminum before finally advancing to silicon, resulting in more abundant ^{24}Mg and ^{27}Al.

Starting with ^{32}S produced by reaction (7) and (9) there is also a protium fusion chain through ^{33}S, ^{34}S, ^{35}Cl, ^{36}Ar, ^{37}Cl, ^{38}Ar and ^{39}K, which is accumulating as ^{40}Ca. Also ^{40}Ca is unlikely to fuse with protium, because the energy would be unusually small according to (19). This isotope is also consistently showing up as a prominent "ash" product of LENR. According to equation (20), fusion with ^{4}He can lift ^{40}Ca beyond this barrier.

There seems to be also an increased abundance of ^{36}Ar, ^{38}Ar, ^{37}Cl and ^{39}K due to the loop back by equation (50).

The most prevalent "ash" product of LENR is ^{56}Fe. This is at least partially the result of several prominent LENR reaction paths leading directly to the most stable ^{56}Fe isotope, e.g. (14), (15) and (62). Also, this iron isotope seems to be accumulated by another protium fusion chain (again partially with electron capture): ^{41}K, ^{42}Ca, ^{43}Ca, ^{44}Ca, ^{45}Sc, ^{46}Ti, ^{47}Ti, ^{48}Ti, ^{49}Ti, ^{50}Ti, ^{51}V, ^{52}Cr, ^{53}Cr, ^{54}Cr, ^{55}Mo, ^{56}Fe, ^{57}Fe, ^{58}Fe, ^{59}Co.

There seems to be an increased abundance of ^{52}Cr in LENR residues due to the loopback cycle in equation (51).

According to (16) the output energy after fusion of ^{56}Fe with protium has the usual size, i.e. fusion with protium seems to be not inhibited. But due to the loop back in equation (52) the fusion chain is probably stuck between ^{56}Fe and ^{59}Co for a while before advancing to ^{60}Ni and beyond.

^{16}O, ^{28}Si, ^{27}Al, ^{56}Fe and ^{40}Ca (in that order) are the most abundant isotopes in the earth's crust. Interestingly, except maybe for ^{16}O the same isotopes are the most abundantly produced by LENR (additionally LENR is producing lots of ^{4}He by spallation). This similarity is hardly coincidential as both, the cosmic nucleosynthesis and LENR reactors are mostly based on fusion of elements with protium.

Reactions (24) and (25) are describing the transmutation of titanium to vanadium and chromium by means of fusion with deuterium. Several similar transmutation paths exist with protium as is described by equations (26), (27), (28) and (29). The latter could explain together with reaction (23) how the electrical explosion of titanium foils under water can form zinc, vanadium and chromium from ^{48}Ti, as has been documented by Lochak and Urutskoev [7].

1.9 Nucleon Tunneling Hypothesis

Tunneling of entire nuclei through the Coulomb barrier may not be the only route for nuclear reactions in CPs. As a hypothesis it is suggested here that the small distances between adjacent nuclei in a CP also enable the tunneling of nucleons or groups of nucleons from one nucleus to the other. The potential barrier in this case is mostly formed by the strong interaction.

Here are examples of nucleon tunneling reactions in CPs:

(30) $^{2}H + ^{105}Pd \rightarrow ^{1}H + ^{106}Pd + 7.34MeV$

(31) $^{7}Li + ^{61}Ni \rightarrow ^{6}Li + ^{62}Ni + 3.35MeV$

(32) $^{7}Li + ^{60}Ni \rightarrow ^{11}B + ^{56}Fe + 2.37MeV$

(33) $^{58}Fe + ^{60}Ni \rightarrow ^{62}Ni + ^{56}Fe + 492keV$

In reactions (30) and (31) a neutron is tunneling from the lighter element to the heavier element.

Reaction (32) would be a demonstration that LENR can also produce lighter elements (e.g. iron) from heavier elements (e.g. nickel) by tunneling an alpha particle into the "fuel" nucleus (e.g. lithium).

In reaction (33) an alpha particle is tunneling from the nickel nucleus to the iron nucleus. Reaction (65) in conjunction with (33) would produce ^{56}Fe and ^{62}Ni from ^{58}Ni and ^{60}Ni. This would fit into the picture that the isotopic analysis of the Rossi "ash" of the fuel powder was showing the depletion of the abundant nickel isotopes in favor of the most stable nickel-62 isotope [43].

1.10 Spallation Hypothesis

After a nuclear reaction occurred, the product nucleus is usually in an excited state. The excitation energy somehow has to leave the nucleus, before a stable isotope is produced. At least three de-excitation channels compete with each other:

- Emission of a gamma quantum, which typically takes in the order of one picosecond (Only in rare cases of metastable excited states, the gamma decay takes much longer).

- Spallation, i.e. the emission of nucleons or nuclei. This case amounts to a fusion-fission reaction. A big portion of the excitation energy is converted to kinetic energy of the fragments. For highly excited nuclei (i.e. E > 15 MeV) this process takes only in the order of 0.1 femtosecond.
- "Cooling" of the excited nucleus by electron-nucleus near-field interaction (see chapter 0). It is believed that this route is faster than gamma emission, but slower than spallation.

It is the fastest of these channels that "wins", i.e. the probability of a particular channel to function is depending primarily on the duration for such reaction.

As a hypothesis it is assumed that gamma radiation is the slowest of these channels, because the coupling of the oscillating moments of the excited nuclei to the electromagnetic far-field is relatively weak.

This leaves room for spallation to occur, as for example:

(34) $^{1}H + {}^{7}Li \rightarrow {}^{8}Be^{*}(17.25MeV) \rightarrow 2\times{}^{4}He + 17.35MeV$

(35) $^{2}H + {}^{6}Li \rightarrow {}^{8}Be^{*}(22.28MeV) \rightarrow 2\times{}^{4}He + 22.37MeV$

(36) $^{1}H + {}^{11}B \rightarrow {}^{12}C^{*}(15.96MeV) \rightarrow 3\times{}^{4}He + 8.68MeV$

(37) $^{1}H + {}^{15}N \rightarrow {}^{16}O^{*}(12.13MeV) \rightarrow {}^{4}He + {}^{12}C + 4.97MeV$

(38) $^{1}H + {}^{17}O \rightarrow {}^{18}F^{*}(5.61MeV) \rightarrow {}^{4}He + {}^{14}N + 1.22MeV$

(39) $^{1}H + {}^{19}F \rightarrow {}^{20}Ne^{*}(12.84MeV) \rightarrow {}^{4}He + {}^{16}O + 8.11MeV$

(40) $2\times{}^{7}Li \rightarrow {}^{14}C^{*}(26.79MeV) \rightarrow n + {}^{13}C + 18.61MeV$

(41) $2\times{}^{6}Li \rightarrow {}^{12}C^{*}(28.17MeV) \rightarrow 3\times{}^{4}He + 20.90MeV$

(42) $2\times{}^{9}Be \rightarrow {}^{18}O(23.48MeV) \rightarrow n + {}^{17}O + 15.43MeV$

(43) $2\times{}^{11}B \rightarrow {}^{22}Ne^{*}(25.36MeV) \rightarrow {}^{4}He + {}^{18}O + 15.69MeV$

(44) $2\times{}^{11}B \rightarrow {}^{22}Ne^{*}(25.36MeV) \rightarrow n + {}^{21}Ne + 15.00MeV$

(45) $2\times{}^{12}C \rightarrow {}^{24}Mg^{*}(13.93MeV) \rightarrow {}^{4}He + {}^{20}Ne + 4.61MeV$

(46) $2\times{}^{14}N \rightarrow {}^{28}Si^{*}(15.53MeV) \rightarrow {}^{4}He + {}^{24}Mg + 5.55MeV$

(47) $2\times{}^{16}O \rightarrow {}^{32}S^{*}(16.54MeV) \rightarrow {}^{4}He + {}^{28}Si + 9.59MeV$

(48) $^{1}H + {}^{27}Al \rightarrow {}^{28}Si^{*}(11.58MeV) \rightarrow {}^{4}He + {}^{24}Mg + 1.61MeV$

(49) $^{1}H + {}^{31}P \rightarrow {}^{32}S^{*}(8.86MeV) \rightarrow {}^{4}He + {}^{28}Si + 1.91MeV$

(50) $^{1}H + {}^{39}K \rightarrow {}^{40}Ca^{*}(8.33MeV) \rightarrow {}^{4}He + {}^{36}Ar + 2.60MeV$

(51) $^{1}H + {}^{55}Mn \rightarrow {}^{56}Fe^{*}(10.18MeV) \rightarrow {}^{4}He + {}^{52}Cr + 2.57MeV$

(52) $^{1}H + {}^{59}Co \rightarrow {}^{60}Ni^{*}(9.53MeV) \rightarrow {}^{4}He + {}^{56}Fe + 3.24MeV$

(53) $^{1}H + {}^{65}Cu \rightarrow {}^{66}Zn^{*}(8.92MeV) \rightarrow {}^{4}He + {}^{62}Ni + 4.34MeV$

(54) $^{1}H + {}^{69}Ga \rightarrow {}^{70}Ge^{*}(8.52MeV) \rightarrow {}^{4}He + {}^{66}Zn + 4.43MeV$

(55) $^{2}H+^{105}Pd\rightarrow^{107}Ag^{*}(13.12MeV)\rightarrow^{4}He+^{103}Rh+10.32MeV$

(56) $^{2}H+^{105}Pd\rightarrow^{107}Ag^{*}(13.12MeV)\rightarrow^{1}H+^{106}Pd+7.34MeV$

(57) $^{7}Li+^{58}Ni\rightarrow^{65}Ga^{*}(17.34MeV)\rightarrow^{28}Si+^{37}Cl+7.93MeV$

(58) $^{6}Li+^{104}Pd\rightarrow^{110}In^{*}(11.17MeV)\rightarrow n+^{54}Cr+^{55}Mn+31.27MeV$

(59) $^{2}H+^{104}Pd\rightarrow^{106}Ag^{*}(10.68MeV)\rightarrow n+^{51}V+^{54}Cr+24.81MeV$

(60) $^{2}H+^{104}Pd\rightarrow^{106}Ag^{*}(10.68MeV)\rightarrow^{48}Ca+^{58}Fe+30.10MeV$

(61) $^{27}Al+^{27}Al\rightarrow^{54}Fe^{*}(21.86MeV)\rightarrow 2\times^{1}H+^{52}Cr+6.45MeV$

(62) $^{12}C+^{48}Ti\rightarrow^{60}Ni^{*}(15.98MeV)\rightarrow^{4}H+^{56}Fe+9.69MeV$

(63) $^{16}O+^{48}Ti\rightarrow^{64}Zn^{*}(12.78MeV)\rightarrow^{1}H+^{63}Cu+5.07MeV$

(64) $^{16}O+^{48}Ti\rightarrow^{64}Zn^{*}(12.78MeV)\rightarrow^{4}He+^{60}Ni+8.82MeV$

The intermediate term in the middle of equations (34) through (64) is showing the excited nucleus with the excitation energy in parentheses. The excitation energy is then leading to fission of the excited nucleus into the products shown at the right hand side.

The spallation hypothesis contributes to explain, why no hard gamma radiation is being observed in conjunction with LENR experiments: The excitation energy is mostly converted to kinetic energy, rather than gamma radiation.

In the early days of LENR research, much effort was invested to measure ^{4}He production in relation to the measured excess heat. These calculations were narrowly focused on the d-d fusion hypothesis of Martin Fleischmann and Stanley Pons. In reality, there are very many more routes to produce ^{4}He from deuterium (and from protium), as can be seen in many of the equations above. These reactions are producing a lot more helium per MeV and per deuteron than the classical reaction candidate in equation (3). It is not certain, how probable the various routes are, but there is conclusive experimental evidence [26], [27], [28], [29] that ^{4}He is not the only reaction product of the Fleischmann-Pons reaction.

Spallation usually emits mostly protons, neutrons and alpha particles and a few heavier fission products. The spallation hypothesis could explain the proton and alpha tracks, which were observed via CR-39 track detectors in some experiments. The scarcity of neutron emissions may be caused by effects discussed in chapter 1.12. In case of fusion with protium the lack of neutron emission is also caused by a proton excess in the product nucleus.

The spallation hypothesis is compelling as an explanation for the observed relative abundance of LENR product isotopes like ^{12}C, ^{24}Mg, ^{27}Al, ^{28}Si, ^{39}K, ^{52}Cr, ^{56}Fe, ^{62}Ni and ^{66}Zn, which is at least partially caused by reactions (37) and (46) through (54). Especially, the spallation loop at (53) would let ^{62}Ni be the main "surviving" nickel isotope upon continued protium fusion, as is evidenced in the Lugano report [43].

If one compares (37) and (48) through (54), there is a trend: Spallation to ^{4}He (subsequent to fusion with protium) requires the less energy the heavier the spalled nucleus is. This is because of the electric repulsion of the helium nucleus is increasing with the nuclear charge. From the high abundance of ^{56}Fe in LENR "ash" one can conclude that isotopes lighter than ^{56}Fe tend to advance to heavier isotopes upon consecutive fusion with protium, whereas isotopes heavier than ^{56}Fe tend to regress towards lighter isotopes. This would also explain why nuclei heavier than gallium are only rarely produced by LENR.

Reaction (56) "converts" a deuteron to a proton, like in reaction (30). However, only in reaction (56) is energy released as kinetic energy of the spallation fragments.

Equations (57), (58), (59) and (60) are describing fusion-fission reactions with two large daughter nuclei. The reactions involving palladium (or other heavy elements) tend to produce neutron-rich isotopes and can emit in some cases free neutrons. It is entirely possible that reactions (58), (59) and (60) do not occur in reality, because the excitation energy is so high that more fragments (e.g. neutrons and alpha particles) will be produced.

Reactions (63) and (64) could explain how the electrical explosion of titanium foils under water can form copper and nickel from ^{48}Ti, as has been found by Lochak and Urutskoev [7].

1.11 Near-Field Electron-Nucleus Interaction Hypothesis

Two of the most intriguing features of LENR are

- the almost total absence of hard gamma radiation, including the absence of positron-electron annihilation radiation from beta plus decay,
- and the almost total absence of radioactive isotopes in the "ash" of the reaction.

The spallation hypothesis on itself cannot fully explain this characteristic, because the spallation fragments sometimes might still be in an excited state, even though the excitation energy is much lower than without spallation. Also, some reactions are probably simple fusion events with no spallation. So, how is the remaining excitation energy "cooled down" without emitting gamma quanta?

As a hypothesis, the answer is believed to be found in near-field interaction between fast and dense electrons and the oscillating electric and magnetic moments of the excited nuclei:

After nuclear fusion occurred, the nucleon wave functions of the excited nuclei become time dependent, resulting in oscillating electric and magnetic moments of the nuclei.

An electron will be accelerated a bit, if it is passing an excited nucleus with high velocity at a distance smaller than the electromagnetic wave length of the oscillation. This is a **non-resonant** transfer of energy, because the electron "behaves" like a free electron to the frequency of the nucleus. No electromagnetic quantum is exchanged. Instead the velocities of the electrons are increased a bit by the energy of the nucleus. In other words, the big energy quantum of the excited nucleus is **down-converted** to millions of small amounts of energy taken away by the electrons, when they pass the oscillating nuclei.

One might wonder why the electrons are accelerated, but not decelerated by the near-field interaction. This is, because deceleration is mostly inhibited in CPs by the Pauli Exclusion Principle. The slower orbitals in a CP are mostly occupied already, leaving acceleration as the only option.

The acceleration of the electrons by the nuclear energy increases the magnetic flux over time. This is the basis of the self-sustained grow hypothesis, see chapter 1.13.

For example, a gamma quantum with an energy of $E = 3MeV$ has a wave length of $\lambda = hc/E = 0.41pm$.

A circle around the excited nucleus with radius λ has the surface $S = \pi\lambda^2 = 0.54pm^2$. Electrons flowing through this circle can interact with the near-field of the oscillations of the excited nucleus.

If the mean current density in a CP is 2.5 A/pm^2, the "cooling" current flowing through the surface S is $I = \bar{J}_z S = 1.3A$. This current represents a stream of 8.4 million electrons per picosecond passing through the near-field of the excited nucleus.

If each of the passing electrons on average is carrying away 100 eV from the excitation energy, the nucleus would arrive at its ground state in 3.6 femtoseconds. In effect, the excited nuclei were "cooled" so fast that the emission of a gamma quantum would be very unlikely, because the latter takes about one picosecond.

Of course, this "**if**" is requiring a careful quantitative analysis, which is beyond the scope of this document, though.

1.12 Altered Weak Interaction Hypothesis

It is a known fact in nuclear physics that the electron density around a nucleus can effect the electron capture rate of radioactive nuclei, which tend to decay via electron capture or beta plus.

As a hypothesis, this could mean for the extreme electron densities in CPs that beta plus decay is always suppressed in favor of electron caption. Reaction (7) is an example of this. This hypothesis would provide an elegant explanation, why the 511 keV positron-electron annihilation radiation is so rarely seen in LENR experiments.

The high electron density in CPs might enable double electron capture reactions, which are impossible under normal conditions, as for example:

(65) $^{58}Ni + 2 \times e^- \rightarrow {}^{58}Fe + 2 \times \nu_e + 1.93MeV$

(66) $^{64}Zn + 2 \times e^- \rightarrow {}^{64}Ni + 2 \times \nu_e + 1.10MeV$

Similar reactions can be expected from ^{36}Ar, ^{40}Ca, ^{50}Cr, ^{54}Fe, ^{74}Se, ^{84}Sr, ^{92}Mo, ^{96}Ru, ^{102}Pd, ^{106}Cd, ^{108}Cd, ^{120}Te, ^{112}Sn, ^{126}Xe, ^{132}Ba, ^{136}Ce, ^{138}Ce, ^{144}Sm and some heavier isotopes.

Interestingly, reactions (65) and (66) are releasing nuclear energy without fusion or fission and without overcoming a Coulomb barrier. In both reactions only a single isotope will be produced as "ash", because no other reaction routes are possible.

Reactions (65) and (66), if they indeed occur, would be an excellent verification of the theory on CPs. Such verification experiment could use short-pulsed high-current vacuum arcs between electrodes made of pure nickel or zinc for an extensive amount of time. If a subsequent chemical analysis finds transmutations from nickel to iron or from zinc to nickel, there would be hardly any alternative explanation available, other than the effect of the high electron density of CPs.

Speculatively one could think that the high electron density and current density in CPs also effect/accelerate beta minus decay. However, the mechanism of such reaction is not understood. CP-accelerated beta minus decay could help to explain, why so few radioactive isotopes and neutrons are produced by LENR.

The accelerated beta minus decay, if it indeed occurs, can be verified by exposing indium to CPs for extensive amounts of time and analyzing the reaction products, if there are any:

(67) $^{115}In \rightarrow {}^{115}Sn + e^- + \overline{\nu}_e + 499keV$

Alternatively one could try to induce double beta minus decay by exposing observationally stable isotopes to CPs:

(68) $^{104}Ru \rightarrow {}^{104}Pd + 2 \times e^- + 2 \times \overline{\nu}_e + 1.30MeV$

(69) $^{110}Pd \rightarrow {}^{110}Cd + 2 \times e^- + 2 \times \overline{\nu}_e + 2.00MeV$

(70) $^{114}Cd \rightarrow {}^{114}Sn + 2 \times e^- + 2 \times \overline{\nu}_e + 540keV$

(71) $^{116}Cd \rightarrow {}^{116}Sn + 2 \times e^- + 2 \times \overline{\nu}_e + 2.81MeV$

(72) $^{128}Te \rightarrow {}^{128}Xe + 2 \times e^- + 2 \times \overline{\nu}_e + 868keV$

(73) $^{130}Te \rightarrow {}^{130}Xe + 2 \times e^- + 2 \times \overline{\nu}_e + 2.53MeV$

Similar reactions might be possible with other neutron-rich isotopes, such as ^{46}Ca, ^{70}Zn, ^{80}Se, ^{86}Kr, ^{94}Zr, ^{98}Mo, ^{122}Sn, ^{124}Sn, ^{134}Xe and some heavier isotopes.

Of course, the altered weak interaction hypothesis needs to be backed by thorough quantitative analysis, but this is beyond the scope of this document.

1.13 CP-Stimulated Alpha Decay Hypothesis

The Irion & Wendt experiment [22] was producing helium by electrical decompositions of a tungsten filament. The experiment has been reproduced successfully by other researchers [23] [24]. The emission of fast neutrons had been detected. The findings are indicating CP-stimulated alpha decay of tungsten:

(74) $^{182}W \rightarrow {}^{178}Hf^* + {}^4He + 1.77MeV \rightarrow 2\times{}^{88}Kr + {}^4He + 2 \times n + 92.57MeV$,
$^{88}Kr \rightarrow {}^{88}Rb + e^- + \overline{\nu}_e + 2.92MeV$, $^{88}Rb \rightarrow {}^{88}Sr + e^- + \overline{\nu}_e + 5.31MeV$

(75) $^{183}W \rightarrow {}^{179}Hf + {}^4He + 1.68MeV$

(76) $^{184}W \rightarrow {}^{180}Hf + {}^4He + 1.66MeV$

(77) $^{186}W \rightarrow {}^{182}Hf + {}^4He + 1.12MeV$

The CP-stimulated alpha decay (if it occurs at all) is energetically possible with all natural isotopes of osmium, tungsten, hafnium, ytterbium, erbium and with the lighter isotopes of dysprosium. This means that not only tungsten (or osmium) could produce helium by this type of reaction, but also its alpha decay products.

Equation (74) is showing an example, where the excitation energy of the alpha decay is causing a subsequent fission of hafnium with a release of two neutrons. The latter might explain, why fast neutrons were observed in Irion-Wendt type of experiments. From a practical standpoint the neutron release (and related radioactivity) might be unwanted, which means that LENR reactor designs should avoid using fissionable elements.

This hypothesis is speculative. The mechanism of CP-stimulated alpha decay is not well understood. It might be caused by the high axial kinetic energy of the electrons, which can be up to about 100 keV in a CP.

1.14 Nuclear Energy Feedback Hypothesis

There is experimental evidence from multiple sources that LENR devices can enter a self-sustained mode, where heat, radiation and even electricity is continuously being produced, while no external energy is supplied [20] [45] [46].

As a hypothesis it is assumed that the nuclear energy produced in a CP is providing a mechanism of continuous acceleration of its electrons and of self-sustained growth for the CP. In detail:

As was said in chapter 0, the energy of excited nuclei is assumed to be capable of increasing the velocity of the electrons in the CP. This process slowly increases the magnetic flux and the intrinsic current of the CP. It also vacates some electron orbitals corresponding to low axial velocities.

The vacated orbitals can then be backfilled by electrons from the environment. This only works, if there are external electrons available, which have some momentum in the right axial direction, otherwise these electrons would be repelled from the CP.

This momentum of the external electrons can come from different sources:

- Glow discharge produces fast electrons moving in all directions.
- The electromagnetic radiation of the CP can cause fast electrons via ionization.
- When CPs catalyze nuclear reactions, some of the energy is released in form of kinetic energy of fission products, such as alpha particles and protons. These particles also create fast electrons via ionization of the surrounding matter.
- A nuclear-active CP is emitting fast electrons in radial direction. Some of these electrons can scatter in the surrounding matter, such that they change their momentum to an axial direction. In this case, the emitted electron can become reabsorbed by the CP.

Finally, if fast electrons have been attracted to the CP, its electric potential is getting lower. This will attract cations from the environment to enter the CP. A high working temperature or a glow discharge may be instrumental for delivering cations to the CP growth process. This would explain why the excess heat production of LENR devices often increases drastically with temperature or in the presence of a glow discharge.

In total, the energy release from nuclear reactions can increase the current density and the size of the CPs, which amounts to self-sustained existence (or growth) of the CP. This would explain, how the PDFL technique of B. Yu. Bogdanovich [45] can produce plasmoids, which can continuously glow for over two days without external energy supply.

Another consequence is that the resistivity of a spark can be negative during the acceleration phase, which means the spark can produce electrical energy supplied to the attached electrodes. This would explain how the PAGD apparatus of the Correas [20] and the Energoniva reactor of Anatoly Vachaev [46] are able to produce electrical energy directly from LENR (no moving parts and no thermoelectric generator involved).

Much practical and theoretical analysis will be needed, to fully understand and quantify the nuclear energy feedback mechanism.

A well-designed LENR reactor would probably attempt to promote the self-sustained CP existence (or growth), because the creation of new CPs would produce more unwanted x-rays and would consume more input energy. In order to stop a LENR reactor, one has to stop creating new CPs and one has to remove the conditions required for self-sustained growth. One could even attempt to generate electrical energy directly from LENR, which would remove some of the complexities and expenses involved by converting heat to electricity.

The observed longevity of CPs in some experiments (e.g. heat after death) may be primarily an indication of self-sustained CP existence from nuclear energy feedback, rather than stemming from any inherent stability of CPs. Thus, for sustained existence CPs must be continuously fed with energy and matter, otherwise they shrink by loosing matter and finally extinguish.

A direct consequence of self-sustaining CP growth is that LENR can enter run-away conditions with uncontrolled and sudden release of large amounts of nuclear energy. Such conditions have in the past lead to rare cases of accidents, where electrolysis experiments exploded or powder-based LENR reactors destroyed themselves in a meltdown.

In order to build safe LENR reactors one has to ensure that the reaction rate is fuel-limited under all possible conditions. For example, a low-pressure glow discharge device can be made fuel-limited (the gas being the fuel), whereas electrolysis is typically not fuel-limited (the electrolyte being the fuel). For more details, see chapter 7.3.

However, the observed accidents could also be interpreted by a mechanism different from self-sustained CP growth: If the negative resistivity of CPs was causing high-voltage oscillations in the connected electrodes, the sudden energy release could have been caused by subsequent discharges from these self-sustained oscillations. An indication for this possibility is that the Energoniva reactor of Anatoly Vachaev [46] and the PAGD apparatus of the Correas [20] are able to operate permanently under these conditions. A possible protection against unwanted electrical oscillation and excessive energy release could be implemented by proper resistive damping of the electrode circuitry.

1.15 Time for a Paradigm Change?

As an experimental physicist one always has to have a working hypothesis of the underlying physics of the analyzed subject, otherwise there is no way to interpret and improve the experiments. If many scientists work on the same subjects and try to replicate each others experiments (as has happened with LENR), there is inevitably some sharing of the working hypotheses needed.

Over time, the working hypotheses are solidifying into a paradigm. The paradigm can be fruitful at times for achieving progress in a chosen direction of research. After a while, the established paradigm also hinders new thought and approaches. This has happened also in LENR research. Only if there are too many gaping inconsistencies between the current paradigm and the experimental findings, there is a chance to change the paradigm by some fresh thought.

It is probably fair to say that after roughly 30 years of research, there is still no consensus about the basic physics underlying LENR. However, there are widely accepted paradigms, which are guiding the experiments in certain directions. The point being made here is that the chosen direction commanded by the widely accepted paradigms of LENR may be insufficient for a successful LENR commercialization.

More concretely, the LENR research historically went through different phases and paradigms:

1.) The era with no paradigm

The “golden era” of physics (1900-1930) was mentally wide open for new things and had not yet developed the rigid orthodoxy of modern institutional physics. For example, Joseph John (“J.J.”) Thomson, who discovered the electron and invented mass spectrometry, was certain (from his experiments) that electric currents in plasma could cause elemental transmutation. In 1912 Thomson and Ramsay created the yet unknown gases He-3 and tritium via glow discharge, calling them “X3” because of the atomic mass.

In 1922 Gerald L. Wendt & Clarence E. Irion extended Thompson's work with high currents. They published that decomposition of tungsten via high-current discharges were producing helium.

In the 1960s and 1970s George Ohsawa observed transmutation of carbon and oxygen into silicon and iron by arching carbon in air.

In 1986 Paulo & Alexandra Correa created a device which generates electricity based on Pulsed Abnormal Glow Discharges (PAGD) in air between aluminum electrodes at low pressure. The output pulses have reached >30 kW, with mean power inputs of 50 to 100W and mean outputs of 200 to 600W.

The experiments of Irion&Wendt, Ohsawa and the Correas are simple to replicate. They would give valuable insights into LENR reactions, where no hydrogen and no transition metals (except for the Irion&Wendt experiment) are involved.

At these former times, there was no established paradigm, how the observed transmutations or excess energy could have occurred. However, there is much to be learned from the pre-Fleischmann experiments on LENR, precisely because there was no established paradigm narrowing down the interpretations during the experiments.

For a more detailed history of LENR discoveries, see [19].

2.) The Fleischman paradigm

Martin Fleischmann and Stanley Pons were not the first researchers, who created nuclear fusion via electrolysis of heavy water with palladium electrodes. Before them, John Tandberg in 1927 did the same. Ivan Stepanovich Filimonenko in 1957 did it with high-temperature electrolysis.

But only after the publication of Fleischmann and Pons, there was world-wide attention. The replication attempts of many laboratories and the influential personality of Martin Fleischmann were creating the "Fleischmann paradigm", which can be summarized in the belief that deuterium nuclei loaded into palladium metal are fusing which each other to produce helium-4 in the lattice of palladium.

This paradigm was later extended by the credo that the loading factor (i.e. the number of deuterium atoms per palladium atom) need to be close to one or higher. Also the current density during electrolysis needs to be very high.

Experimentally, there is still no evidence available that hydrogen fuses in the lattice of a metal crystal. To the contrary, the Piantelli-type LENR reaction achieves excess heat with protium (which cannot fuse with itself) and nickel (which loads only very insignificant amounts of hydrogen into the bulk metal).

The Fleischmann paradigm persists until today so strongly that some researchers simply ignore or deny the fact that neither deuterium nor transition metals nor a lattice are required for creating LENR.

3.) The nano-particle paradigm

Over time, a new paradigm has gradually emerged. This "nano-particle" paradigm says that bulk metal is not active for LENR. Inspired by Edmund Storms' concept of the nuclear active environment and by the Pd/ZrO_2 nano-powder experiments of the late Yoshiaki Arata, the new belief is that the LENR effect comes from locations at the surface. Many attempts were made, to increase the surface to the extreme by using fine metal powder or palladium nano-particles dispersed in ceramics powder.

The commercialization attempts of Brillouin Energy Corporation and Leonardo Corporation are both influenced largely by this paradigm. A recent experiment of Tadahiko Mizuno is also centered on Pd nano-particles [34]

However, it is not proven that nano-particles or metal powder are exhibiting a stronger LENR effect than solid sheets or rods of material. In all cases the available surface area will be mostly inactive, except for some tiny spots at the surface.

For example, loading palladium black (a spongy powder with a large specific surface area) under high pressure with deuterium is not producing noticeable amounts of excess heat. On the other hand, LENR devices with a very high COP, like the one from Klimov et al. [31], have not used powder or gaseous hydrogen at all.

Nonetheless the nano-powder paradigm persists strongly and is probably quite misleading for the subsequent improvement of LENR devices.

4.) The forming of the plasmoid paradigm

At the horizon, something new is forming, which can become the next paradigm in LENR research. More and more researchers understand that high-current plasmoids are required to trigger the heat generation of LENR. For example, Brillouin is using sparks to treat their nickel powder *in situ*, high-current glow discharge is well-known for its strong LENR effect, Mizuno-type plasma electrolysis produces large excess heat, the many LENR devices constructed by Randal Mills (Brilliant Light Power Inc.) are mostly starting with plasmoids (Mills denies that this is LENR, though). There are many more successful LENR devices, which could be listed here, all involving plasmoids (sometimes unbeknownst to the researcher, as is the case with the original Fleischmann-Pons experiment).

In light of the theory on CP, this theme makes a lot of sense. The author would argue that it may be time to establish this theme as the new paradigm in order to achieve a high COP and good reliability for the commercial route.

1.16 Reinterpretation of the Fleischmann-Pons Electrolysis Experiment

So, if the functioning of LENR requires high-current plasmoids, how could the Fleischmann-Pons electrolysis experiment have produced excess heat? Was there any plasma? The answer is "yes", although many observers might have overlooked it:

In Fleischmann-Pons electrolysis of heavy water there is a thin sheath of electrolyte around the palladium cathode, which is depleted of ions by the electric field. The cations are pulled towards the cathode and become neutralized by electrons from the cathode. The anions are pushed away from the cathode. In consequence, there is a "cathode fall" were a good portion of the cathode-anode voltage drops in the thin sheath of mostly water, which surrounds the cathode.

When the electrolyses voltage is made high enough (presumably to achieve the required current density), there will be frequent electrical discharges ("microsparks") from the cathode through the depletion sheath into the electrolyte. These discharges are creating little plasmoids with very high current pulses, because the depletion sheath acts as the dielectric of a supercapacitor formed by the cathode and the electrolyte. The microspark discharges are creating a lot of radio frequency noise, acoustic noise and they are clearly visible as frequent little flashes of heat, when being observed with an infrared camera (they also emit visible light). Much of this was already known by Takaaki Matsumoto in 1995. His article is rather revealing and is recommended to read [39].

The plasmoids will then condense to closed-loop CPs and fall back to the cathode surface. There, the CPs will produce heat and will ionize craters into the surface of the cathode, as can be seen in the following:

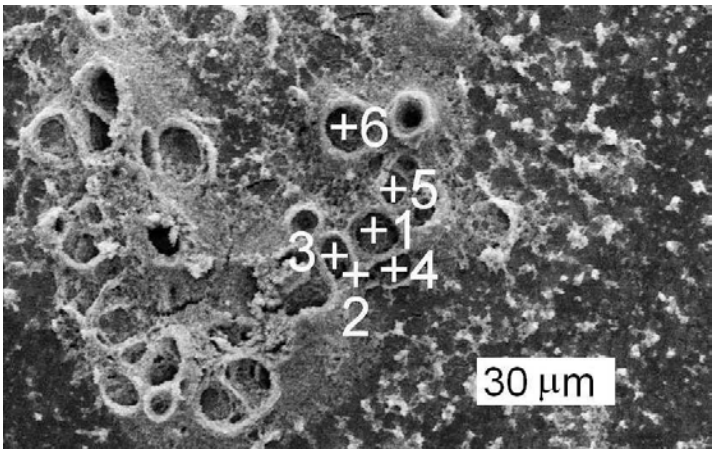

Figure 3 Volcano-like structures found at the palladium cathode surface after electrolysis of heavy water, W.-S. Zhang and J. Dash [32]

Note that the craters are surrounded by re-crystallized palladium. This is the material edged away by the CPs out of the palladium bulk. The craters are important for the excess heat production, because they are stabilizing and housing CPs for a longer period of time.

Often, when the electric field rises again, the dormant CPs will break to an open-ended configuration and start the next discharge through the depletion sheath. This gives them "the next shot in the arm" for successive growth. With this complicated process in mind, it becomes clear, why

- There is typically a long "incubation time", before the cathode will begin to produce excess heat.
- There is "heat after death", i.e. when the cathode is lifted out of the water, it sometimes continues to produce heat for maybe up to an hour. During this "afterglow", the CPs in their craters of the cathode are continuing to cause nuclear reactions, until they finally decay.
- A cathode, which was producing high amounts of heat in a previous run of experiments, can be up-started much quicker than freshly produced cathodes (even after several days) for a new run of experiment. At least the craters persist between the runs, if not the CPs inside.
- The excess heat and nuclear "ash" is produced at the surface of the cathode, rather than in the bulk material.

Without going into details here, there are many more LENR experiments, were the existence of plasmoids has either been overlooked by the researchers or the role of the plasmoids was meant to be a just "cleaning of the surface" [34]. Often, thin films have been *plasma*-sputtered on the active surface of the reactor. In all cases one should keep the possibility in mind that the plasmoids were creating long-living CPs, which subsequently were creating the observed excess heat.

LENR is creating a lot of "dirt" i.e. transmuted elements and remains from erosion. What is the point, anyway, to clean a surface in a LENR reactor?

1.17 Discrepancies and the Question of Superconducting CPs

The computational results from the current model of CPs do not in all cases agree with experimental findings. For example:

- Ken Shoulders was using a 1 kΩ resistor in series with the cathode for his "pico-pulser" to launch CPs. The intrinsic currents computed for CPs are way higher than what could possibly pass through such resistor.
- The computed formation energies are 10 to 90 keV higher than what would be required for the length stability of condensed plasmoids.
- The appearing of CPs in LENR experiments, where no strong current pulses were applied, would suggest much lower formation energies.
- The electron-phonon coupling may be too high for the observed lack of resistive losses in CPs, but this has not yet been calculated.

One (remote) possibility to remove the said discrepancies would be to assume that CPs are superconducting or are containing a superconducting phase of the electron gas. No detailed analysis is available yet.

In order to lend some plausibility to superconducting CPs, one would have to compute the strength of electron-phonon coupling in CPs (this would be useful to know, anyway). With the result one would need to compute the binding energy of a cooper pair. The binding energy needs to be high enough to enable Bose-Einstein condensation at 1500 degrees Celsius or above. If that is fulfilled, one has to find out the maximum strength of the magnetic field, which the condensate can withstand. Only if all these prerequisites fit to CPs, it is worth developing a detailed model of superconducting CPs.

Pretending that superconducting CPs exist, there were some interesting consequences:

- Many electrons could share the same quantum-mechanical state in the Bose-Einstein condensate, thereby lowering the mean kinetic energy of the electrons by maybe 10 to 100 keV
- The magnetic field, the axial current and the mean axial velocity of the electrons would be much lower
- The density of CPs could still be the same, because both, the degeneracy pressure of the electron gas and the magnetic pressure of the z-pinch are reduced jointly

Additional research is required for both, addressing the said discrepancies and exploring the possibility of superconducting CPs (if one were to consider the latter seriously).

Another possibility is that the Hamiltonian used for computing the current results needs to be augmented by an attractive energy term of yet unknown origin. This term would need to lower the formation energy with increasing densities for removing the said discrepancies.

1.18 Are CPs Ubiquitous in the Environment?

Keith A. Fredericks analyzed mysterious "tracks" on photographic films and nuclear emulsion, which were not exposed to LENR experiments or electrical discharges [36] [37]. He found and documented the same type of patterns, which showed up on the x-ray films and nuclear emulsions used for documenting the "strange radiation" of LENR experiments [7] [14] [16] [6]. This is rather startling: Patterns previously thought to be specific to LENR environments have been observed in the absence of LENR.

There are several alternative ways to interpret the findings of Fredericks:

- Inadvertent electrostatic discharges in conjunction with the film handling have created CPs, which exposed the films. If this were true, the creation of CPs would require much lower currents, than the intrinsic CP currents computed via the current modeling.
- CPs could be ubiquitous and long-living in the natural environment. If this were true, one would need to be critical with the observations of "strange radiation" by Urutskoev and other authors. Some of the observed patterns may be stemming from the natural background, rather than from the LENR experiment. Also, the sources of the natural CP background would need to be determined.

There is not yet enough data available to judge upon these alternatives. Nonetheless, the patterns documented by Fredericks will be treated in chapter 2 as imprints of CPs.

2 Visual Evidence of CPs in LENR Experiments

2.1 Common Patterns under Very Different Conditions

Throughout the course of LENR research a large variety of strange patterns ("tracks" and craters) have been found microscopically on the surfaces of the electrodes, x-ray films, nuclear emulsion, mica sheets and plastics surfaces.

These patterns are exhibiting commonalities under a wide range of experimental conditions, such as glow discharge, electric explosion of metallic wires and thin foils, low-energy discharges in water, electrolysis and cavitation. All these environments are capable of LENR.

Another set of patterns was produced by the experiments of Ken Shoulders when studying charge clusters. There is photographic evidence that these charge clusters are of the same nature than the objects, which create the tracks in LENR experiments.

Yet another source of evidence comes from dense plasma focus devices, when the "corrosion" patterns of the anode are analyzed microscopically.

There is a common misunderstanding in conjunction with these "tracks": Researches were interpreting the pattern as tracks of compact (corpuscular) particles moving in a "spiraling" manner over the surface. For example, this has led to the speculation that the "tracks" were caused by magnetic monopoles. In this interpretation the shape of the "tracks" is equated with a trajectory.

In contrast, the theory on CPs is interpreting the "tracks" as ionization imprints of extended objects. In this interpretation the shape of the "tracks" is equated with the shape of the causing objects, i.e. a CP. In other words, the imprinted object was typically not moving at all and the "tracks" are not tracks or trajectories.

In the following a collection of microscopic images is shown, which is rendering imprints left by closed-looped CPs. These images are evidence of mesoscopic objects (i.e. CPs), which were forming in the experiments.

2.2 Bore Holes, Material Damage

In Pd/D co-deposition LENR electrolysis experiments of P.A. Mosier-Boss *et al.* at SPAWAR there were indications of "molten" palladium seen around craters of up to 50 micrometer size. Some SEM images of these features are shown below:

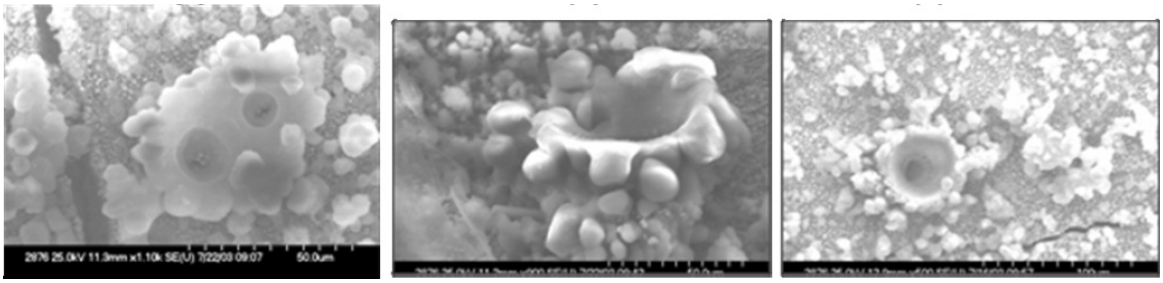

Figure 4 Images of "molten" features observed in Pd/D co-deposition electrolysis [38]

The researchers concluded that about 6×10^{-2} J of energy was created by a sudden nuclear event, which evaporated the palladium in the volume of these craters.

In light of the theory on CPs these craters can be explained differently: Microsparks at the cathode surfaces created CPs (The CPs were potentially amplified by nuclear energy). The CPs were ionizing palladium at the centers of the craters and re-condensing it at the crater rims. The ionization and re-condensation is non-dissipative, i.e. it requires much less energy than evaporating the same amount of palladium.

An indication that indeed a much lower amount of energy is able to produce such craters can be seen below:

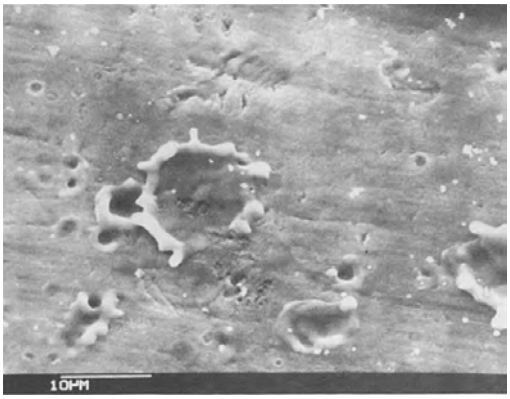

Figure 5 Impact marks of small CPs hitting a titanium target [2]

The above SEM image was provided by Ken Shoulders from "bombarding" a titanium surface with CPs. These CPs were (according to Shoulders) created by less than 10^{-6} J of electrical energy. Clearly, this is not enough energy to evaporate metal. Nevertheless the material at the crater rims has this molten appearance.

The CPs created by Ken Shoulders were able to bore holes through a foil of aluminum:

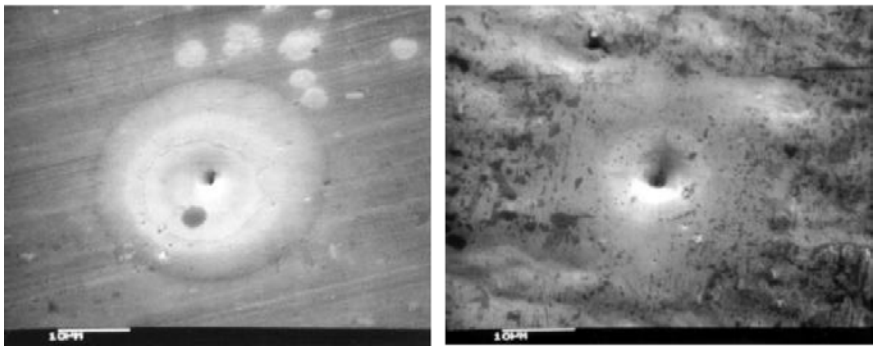

Figure 6 Hole from a CP passing through a 6 micrometer thick aluminum foil. Left: entry side; Right: exit side [1]

Again, there is re-condensed material around the bore hole, which has a molten appearance, but more likely stems from ionization.

The penetration depth of CPs in metals is limited, because:

- There is no electric field, which drives the CPs in a certain direction
- The intrinsic current of CPs tends to short-circuit through the conducting metal, which then dissipates the energy of the CPs via resistive losses

In contrast, the penetration depth of CPs in dielectric substances can be much higher, especially if there is an electric field perpendicular to the dielectric surface. The field is driving the CPs towards the anode. Much deeper penetration occurs, if the dielectric has pores or cracks (no matter how narrow), in which case the CPs will follow the pores/cracks and enlarge them during their passage to maybe 20-micrometer-wide holes.

The following images from Shoulders are showing bore holes from CPs in a 0.5 mm thick alumina plate:

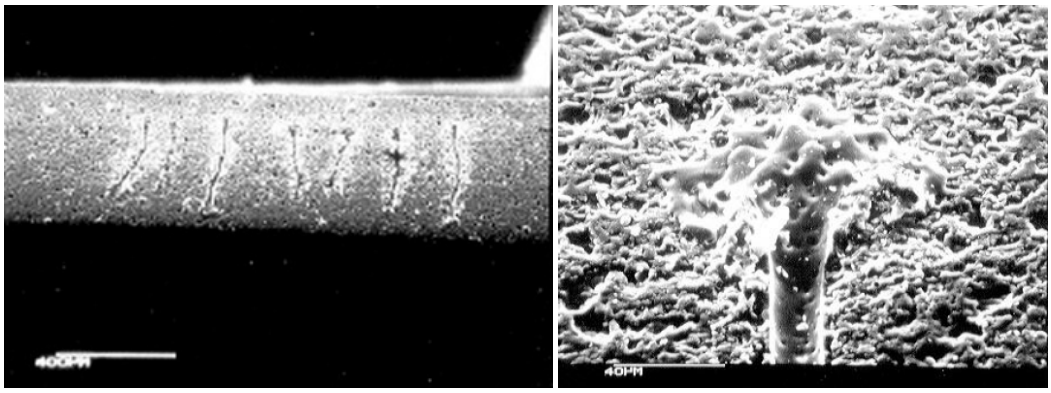

Figure 7 CP bore holes in alumina [1]

Other examples from Shoulders:

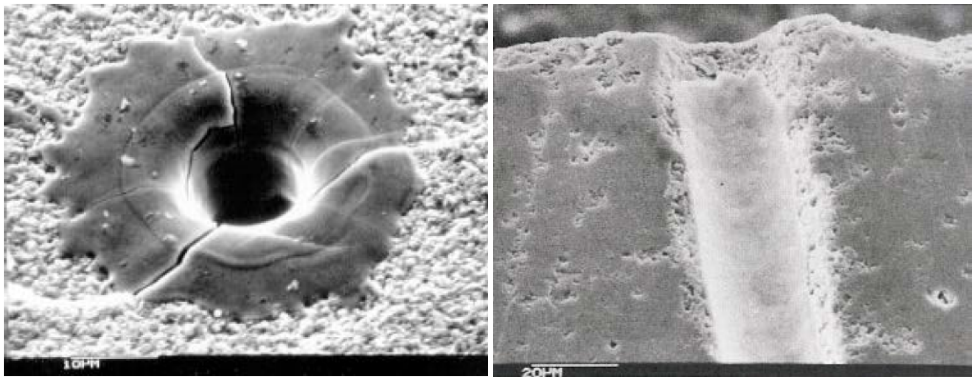

Figure 8 SEM micrograph of CPs boring into lead glass [1] and alumina [2] [15]

At the right image virtually no thermal damage of the solid is visible directly besides the thin re-condensed sheet of alumina. This is a strong indication that the material transport of CPs has indeed a non-thermal origin.

2.3 Lines, Rail Groups, Tapering

CPs in LENR experiments often show up as straight or bent lines. The lines are probably signifying a high electron velocity inside the CPs. In some cases the lines have a periodic sub-structure, but this is not always visible.

One remarkable feature of these lines is their tendency to appear in groups like parallel "rails".

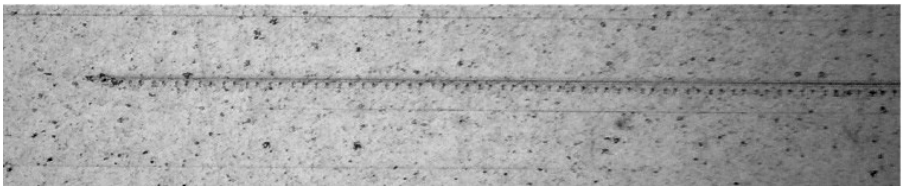

Figure 9 Group of CPs in parallel "rails", length: 1.87mm [16]

Another example of a rail group, in this case with a periodic substructure, is shown below:

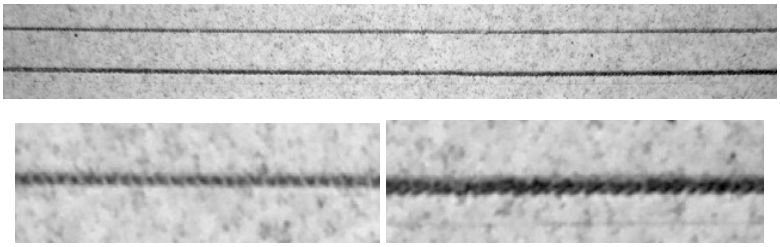

Figure 10 Rail group of CPs and two enlargements, one of the upper track, one of the lower one, looking like left and right helices [16]

Interestingly, the individual lines of a rail group are often following the same curvature (i.e. they maintain the same distance) in case the rails are bent. This can be seen in Figure 11 and Figure 12:

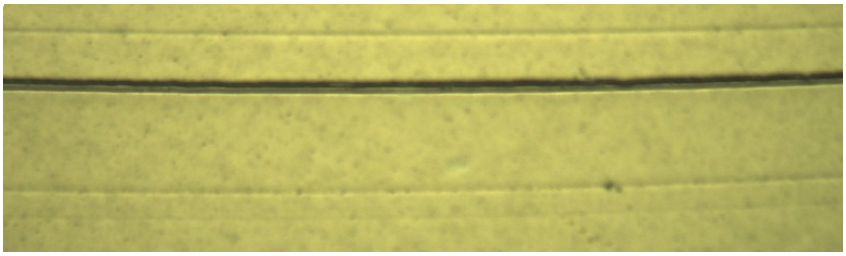

Figure 11 Rail group of CPs on nuclear emulsion [14]

In the most common case rail groups consist of just two lines:

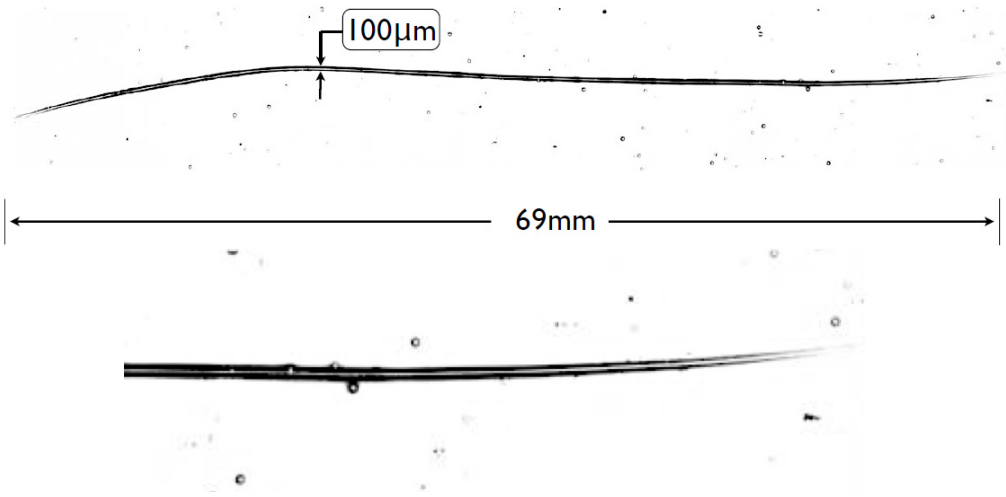

Figure 12 Imprint of a rail group with two lines and tapering [37].
At the bottom an enlargement of the right end of the group is depicted.

As can be seen in Figure 12, the lines often do not end abruptly, but are tapering off. In chapter 2.8 a speculative explanation will be provided for the tapering and why the lines of a rail group maintain a constant distance to each other.

2.4 Aggregation, Branching

There is microscopic evidence that CPs can branch into several paths. This can be interpreted in different ways:

- At a branching point the larger core of the CP forks into two smaller cores
- At a branching point a bundle of separate cores visibly forks to larger distances

There may be cases for both interpretations, depending on the condition of the CP.

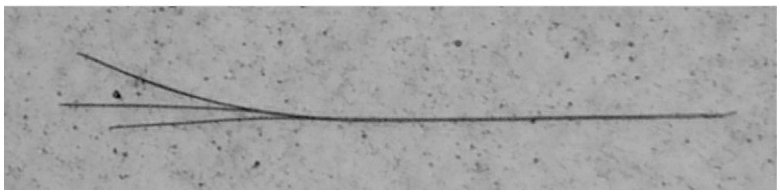

Figure 13 CP with branching points, length: 0.77mm [16]

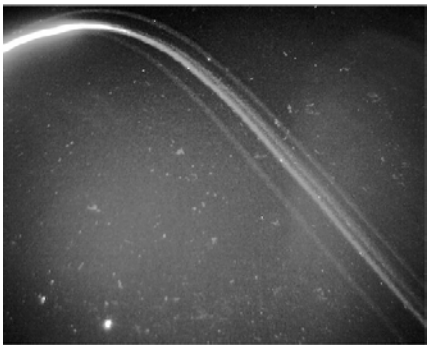

Figure 14 CP branching into a rail group [37]

There are cases, were a CP branches and after a distance rejoins into a common path:

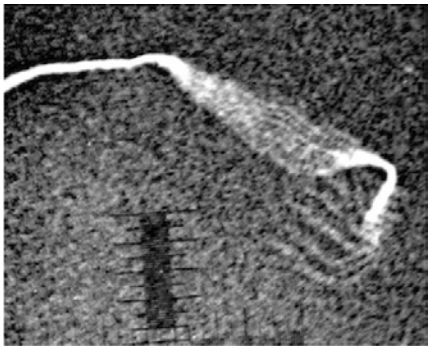

Figure 15 A CP branching, rejoining and branching again [37]

The author believes that the branching/rejoining behavior occurs especially under space-constrained conditions, i.e. CPs squeezing through very narrow cracks.

2.5 Rings, Wiping, Polygons

In the absence of strong electric fields CPs tend to form rings. Ken Shoulders provided the following image of a small CP ring:

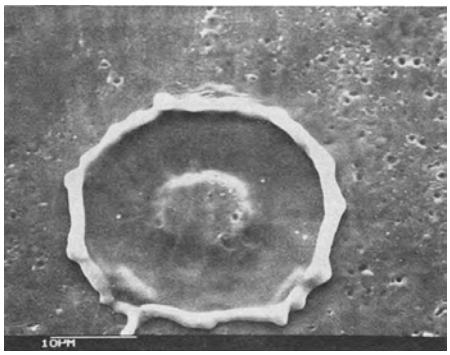

Figure 16 Ring mark of a CP with wiping [2]

The inner rim of this ring imprint is not as steep as the outer rim. This could mean that the ring was increasing its diameter over time and "wiping" over the surface. The author believes that CPs are becoming larger when the intrinsic current is decreasing over time. The reason for the enlargement is not yet well understood.

Another early observer of CP rings was Takaaki Matsumoto in 1995 [39]:

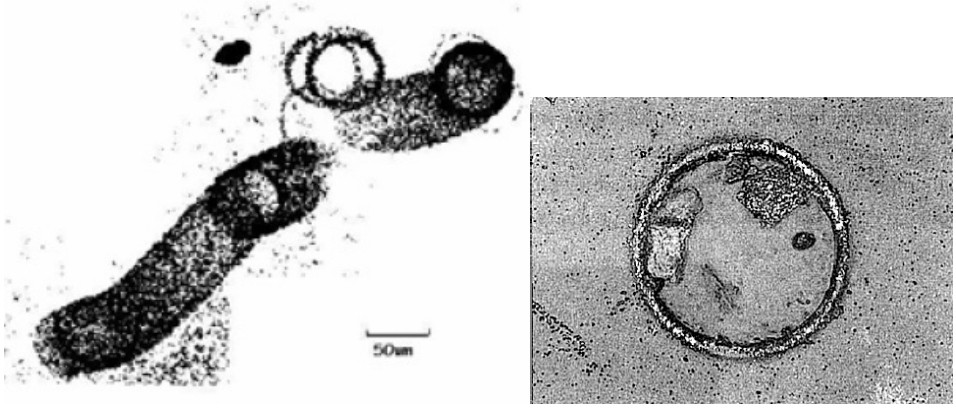

Figure 17 Left: CP ring moving along the surface of an x-ray film; Right: CP ring on an electrode [36] [40]

Matsumoto observed a CP ring on an iron electrode, which enlarged over time and transformed to a polygon:

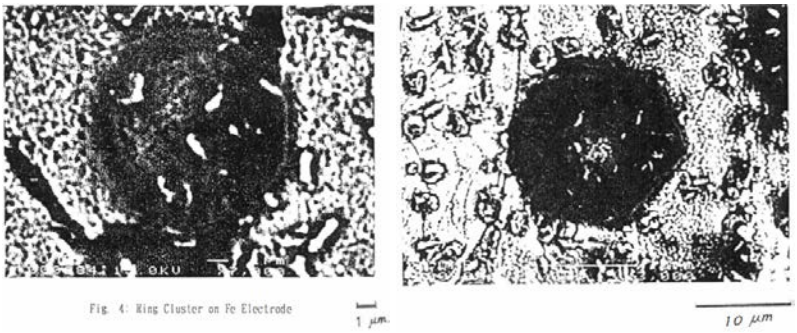

Figure 18 CP ring on an iron electrode, which enlarged over time and transformed to a polygon [39]

The reason for the transformation could be that the intrinsic current of the CP decreased over time. With lower current the mean electron velocity is smaller, allowing the sharp angles to occur at the polygon. There are no reasons, which would dictate that the polygon has to be a hexagon or has to be regular.

Very clear images of CP rings with wiping were provided by Claude Daviau *et al.* and by Rodinov/Savvatimova:

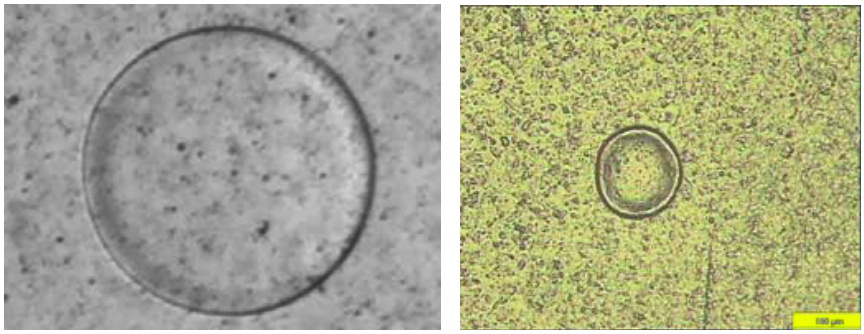

Figure 19 CP rings with wiping on x-ray film, diameter = 0.2 mm [16] [6]

Note that the imprint is not due to exposure of silver grains as is usual with ionizing radiation, but rather consists of a groove dug in the film (via ionization by the CP).

Figure 19 is providing clear indication for wiping. The diameter growth of the CP was initially faster and then slowed down to rest. The result is a gentle slope at the inner side of the groove and a steep slope at the outer side.

The next image is showing the formation of two CP loops from CPs, which originally landed in a linear open-ended configuration on the film:

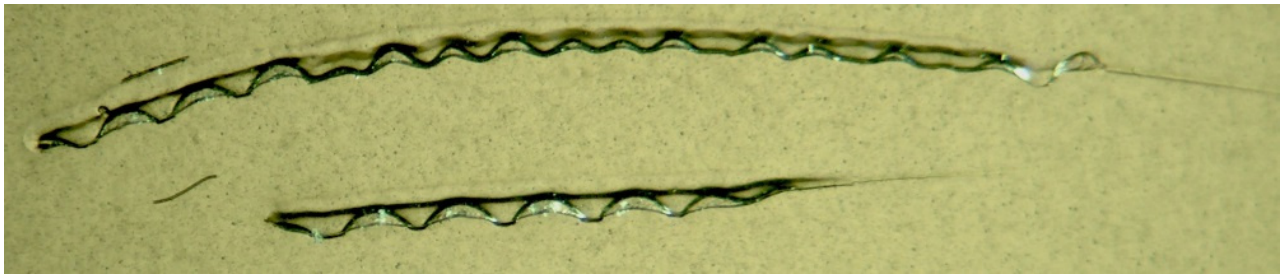

Figure 20 Two CPs transforming from an open-ended configuration to a closed-loop configuration at the surface of x-ray film [14]

It is fortunate for the observer that the CPs at the above image were moving south slightly over time. Therefore, the oldest imprints of the CPs were preserved at the northern border, intermediate imprints can be seen, which are looking like slopes, and the youngest imprints are visible as pairs of meandering black lines. So the image is telling a little history, which will be explained in steps:

At first, two open-ended CPs were piercing through the wraps of the x-ray film and attaching themselves to the surface of the film. At this point in time, the electron velocity was high, the CPs were almost straight with just a slight curvature. In both CPs the electrons were flowing from the right side to the left side of the picture. The nuclei had a negligible velocity.

At the right side of the CPs (i.e. the positive end) the electrons were moving away from the nuclei, leaving them as cations on the surface of the film seeking for a compensation charge. At the left side of the CPs (i.e. the negative end) the electrons were flowing out, which formed negatively charged electron clouds seeking for a compensation charge.

The CPs were surrounded by halos, i.e. cations, which were compensating the excess negative charge of the cores. In the next step the electron clouds were attracted by the halo cations. The electron streams coming out of the left end of the CPs therefore bended south to follow the halo sheet. These bends can be seen at the left end of the CPs.

At the right side the CPs were becoming shorter, because there was a lack of electrons and the vacated nuclei were no longer part of the plasmoids.

The electrons were flowing along the halo attracted by the new positive end, which was somewhat west of the original end. The electron flows were again bending, this time to enter the CP cores at the positive ends. This was closing the loops. The electrons flowing through the halos were condensing with the halo cations to form a new segment of the cores.

In the last step the electrons of the CPs were decelerating a bit. This caused the loops to prolong. The prolongation was causing the meandering of the black lines. The electrons in the two adjacent core lines (belonging to the same loop) were moving in opposite direction, which caused these lines to repel each other magnetically. This is why the lower line is not fully following the meander of the upper line.

One should not confuse the meandering lines of the above CPs with the helical structures described in chapter 2.8. The meanders are caused by CP prolongation. The helical structures are caused by magnetic forces. The CP loops seen in Figure 20 do not have the helical structure depicted in Figure 2.

2.6 Pits and "Sausages" Structures

The probably most stable configurations of CPs are showing up on surfaces like pits (craters) and structures dubbed "sausages" by I. Savvatimova. Pits can grow to sausages, thus they are not fundamentally different. The following two images are from Rodinov and Savvatimova:

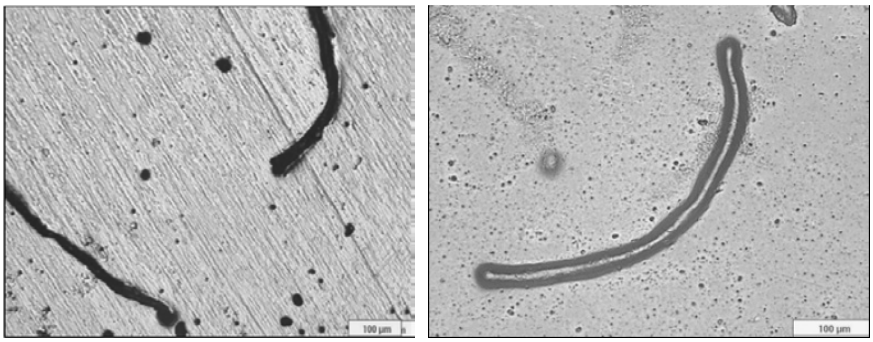

Figure 21 Left: CP pits and "sausages" on the surface of a Pd glow discharge cathode [6].
Right: CP "sausage" on x-ray film. [37]

Sausages are believed to be densely wound two-layer CP solenoids with a basic structure depicted in Figure 2. These configurations are electrically closed loops. They have a strong longitudinal magnetic field and no azimuthal magnetic field. The ends of the sausages are magnetic poles, which are attracting each other.

The magnetic attraction of the sausage ends are often causing these objects to bend, exhibiting anything from a bow to a horse shoe etc. An example of a horse shoe shape was provided by Daviau *et al.*:

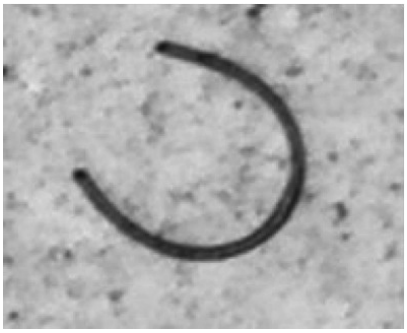

Figure 22 CP sausage bent to a horse shoe shape on x-ray film, width = 0.19 mm [16]

The shape of the sausage in Figure 22 can be interpreted mechanically: The sausage has a certain stiffness stemming from the magnetic attraction of neighboring turns of the solenoid. Also the high electron momentum resists sharp bends of the structure. The magnetic poles at the ends are pulled together. The horse shoe shape is the equilibrium between the magnetic force and the *reactio* force of the stiffness. The lever action of the magnetic force is stronger in the middle of the sausage and weaker at the ends. This is why the curvature radius is smaller in the middle and larger at the ends.

The sausage-shaped CPs are believed to be the main contributors to the excess heat production in LENR devices.

2.7 “Chain of Beads” Structures

When a CP in linear shape prolongs, the additional length sometimes agglomerates to “beads”, which remain connected via lines. An example of such “chain of beads” structure can be seen below at the surface of a Pd cathode:

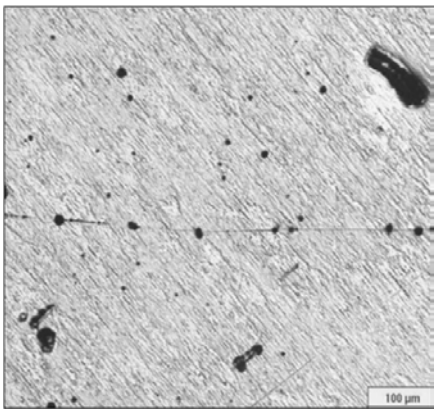

Figure 23 CP in a “chain of beads” structure [6]

It is believed that the chain of beads structure signifies a low electron velocity. Sometimes the lines between the beads are so thin that only the beads are visible. The beads of the chain sometimes form the corners of a polygon.

The following images were made by Ken Shoulders:

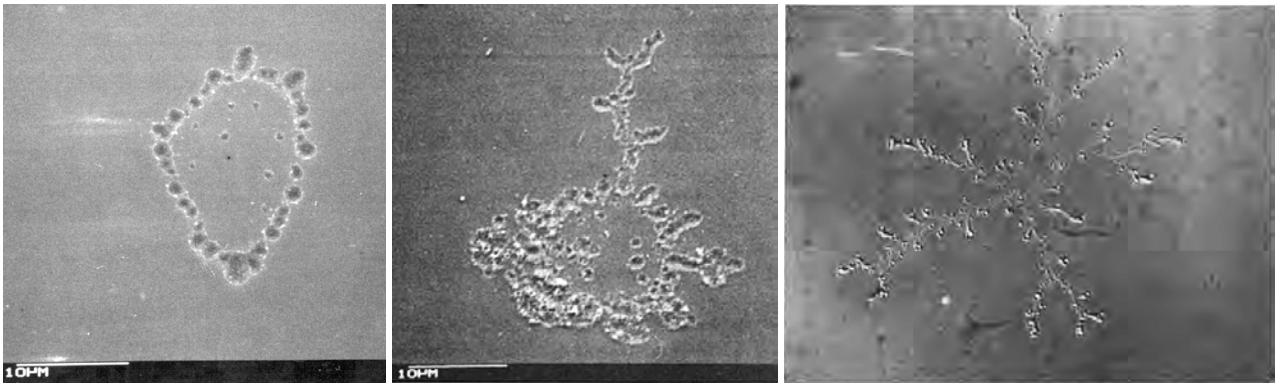

Figure 24 CPs in chain of beads configuration [2]

The different shapes in Figure 24 are variances of the same thing, only the flight time of the CPs through the air was varied. At the left side the flight time was large, so that the CP had enough time to agglomerate to fully developed beads before the CP was hitting the target screen. In the middle the flight time was shorter, therefore the agglomeration is incomplete. At the right side the flight time was shortest and the stringy structure of the CP didn’t agglomerate to beads. The Lichtenberg-figure-like structure of the CP at the right side might also be caused by uncompensated negative charges of the CP core, whereas the CP at the left side looks more an electrically neutral object. In comparison of these three cases it becomes clear that the depicted CPs are contiguous objects with a loop structure, rather than consisting of loose beads.

There is no limit, how big the beads can be. A ball lightning is an example of a very large agglomerated CP.

Ken Shoulders in his experiments didn’t get images of CPs with high electron velocities. This is, because the injected current in his CP “launchers” was limited by a series resistor.

2.8 Quasi-Periodic Structures, “Caterpillar Tracks”

Ken Shoulders was able to view the formation of CPs at a cathode tip by means of a pinhole camera. The camera operated in vacuum and was sensitive to electrons.

When the electric field strength exceeded the threshold voltage for field emission, an electron cloud was forming at the cathode tip. This cloud carried a current from the electrons flowing away from the cathode. The magnetic field of the current was compressing the electron cloud into a narrow channel, which then in conjunction with ions extracted from the cathode tip condensed to a CP.

The said process normally leads to CPs having a bizarre zigzag form. But in some cases, the CPs were forming a helical structure as can be seen below:

Figure 25 Image from the pinhole camera of Ken Shoulders: A bundle of two CPs emitted by a cathode tip at the lower portion of the image is forming a helical pattern. The CPs were emitting electrons in all directions and were continuing their growth at the top of the photo. The length of the depicted structure is about 0.3 mm. [2]

The next image is showing a helical CP imprint on an aluminum foil. The foil was hit by sparks from the rear side, which was causing the holes punched through the foil.

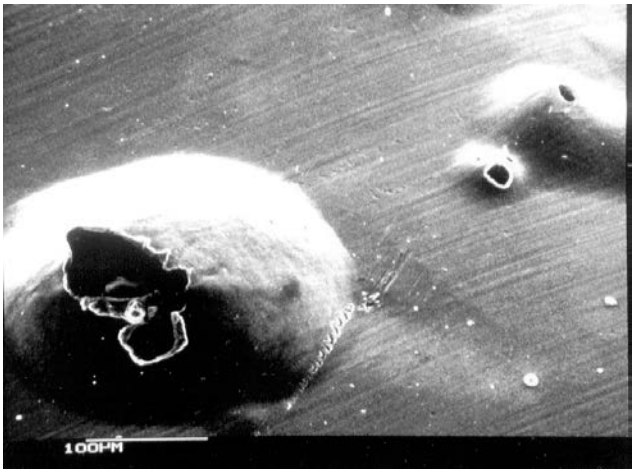

Figure 26 Imprint of a helical CP on the surface of aluminum foil. Source: Ken Shoulders

The helical form of CPs is a common pattern found on surfaces and films exposed to LENR devices. It is believed that these structures are related to high currents and high electron velocities inside the CPs. The basic structure of helical CPs (Figure 2) is essentially the same as with sausages, but the solenoid turns have a much larger interstice.

The periodic patterns left by helical CPs often look, as if the objects were noncontiguous. In reality, the CPs are always contiguous plasma wires. However, their helical structure is three-dimensional and only the bottom part of it is imprinting on the surface, the upper part is running through the air.

The following images are from Rodinov and Savvatimova:

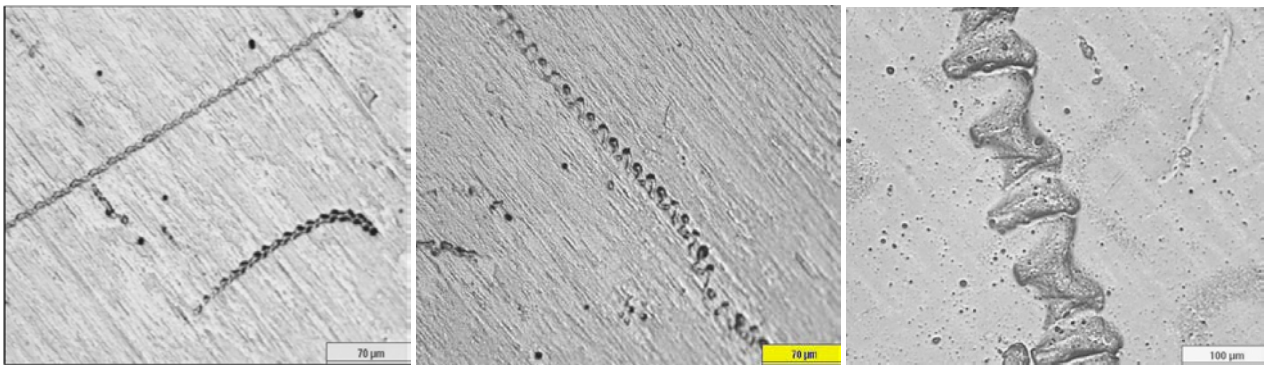

Figure 27 Quasi-periodic patterns from helical CPs produced by glow discharge.
Left and middle: Pd cathode, right: nuclear emulsion [6]

Also Urutskoev has seen these quasi-periodic patterns (sometimes called “caterpillar tracks” or “Urutskoev tracks”):

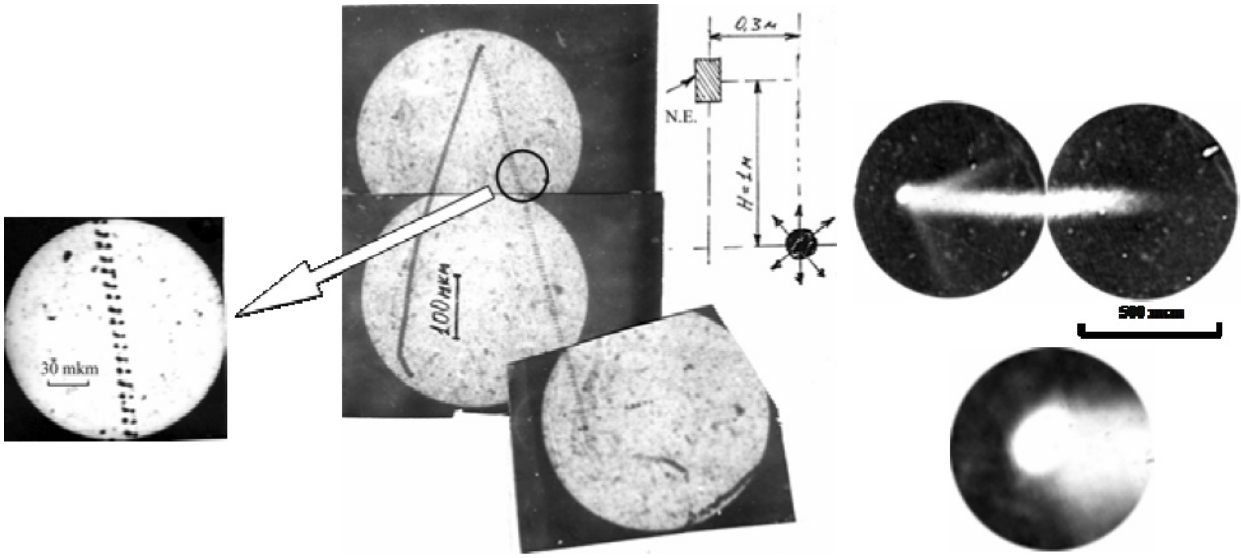

Figure 28 Images of CPs on x-ray film. Left: Quasi-periodic patterns from helical CPs;
Right: Pattern showing up, when a magnetic field perpendicular to the film surface was applied [7]

The quasi-periodic patterns appeared on the film only in the absence of a magnetic field. If a magnetic field was applied, such that the field lines were perpendicular to the film, a different type of pattern was recorded, as can be seen on the right side of Figure 28. This pattern indicates that the CP could pierce through the wrapping of the film, but was hindered by the magnetic field to move freely along the surface.

The author believes that the quasi-periodic type of CPs is responsible for the laser-like x-ray emissions reported by Karabut *et al.* [30]. The periodic structure works like an undulator in a free-electron laser and collimates the emitted x-ray beam in the direction of helix axis.

Keith Fredericks has documented a collection of different quasi-periodic CP patterns:

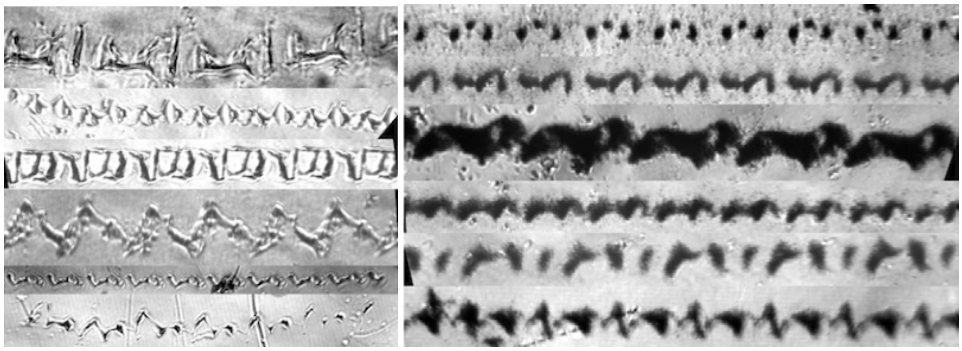

Figure 29 Quasi-periodic patterns on film [36] [37]

As complex as these patterns appear, they can in many cases be related to the basic structure of helical CPs in Figure 2. For this purpose the following drawing was prepared:

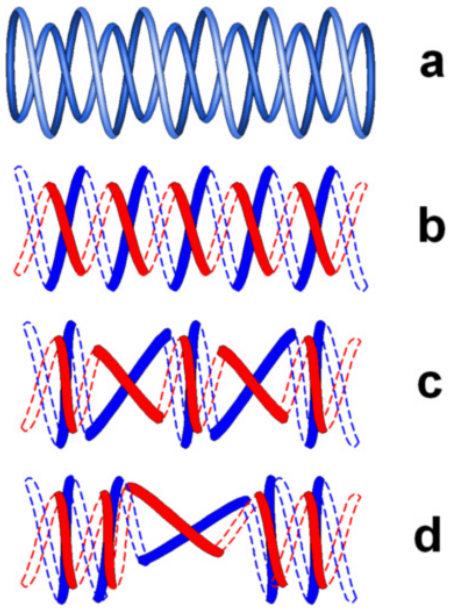

Figure 30 **a**: Schematics of the three dimensional structure of a helical CP;
b: XXXXX-pattern resulting from the imprint of the bottom-half of the CP.
The dotted lines are the invisible paths through the air
c: IXIXI-pattern resulting from a deformation of the basic structure
d: IMI-pattern resulting from a deformation of the basics structure

The deformations, which are responsible for the deviation from the basic structure, are caused by magnetic interaction between the inner (red) and the outer (blue) layer of the solenoid. The currents in the red and blue sections attract each other magnetically. Therefore the CP tends to deform in a way that the red and the blue bars can align in parallel. This is stretching other crossings.

In the following a real-world example of an IXIXI-pattern is analyzed:

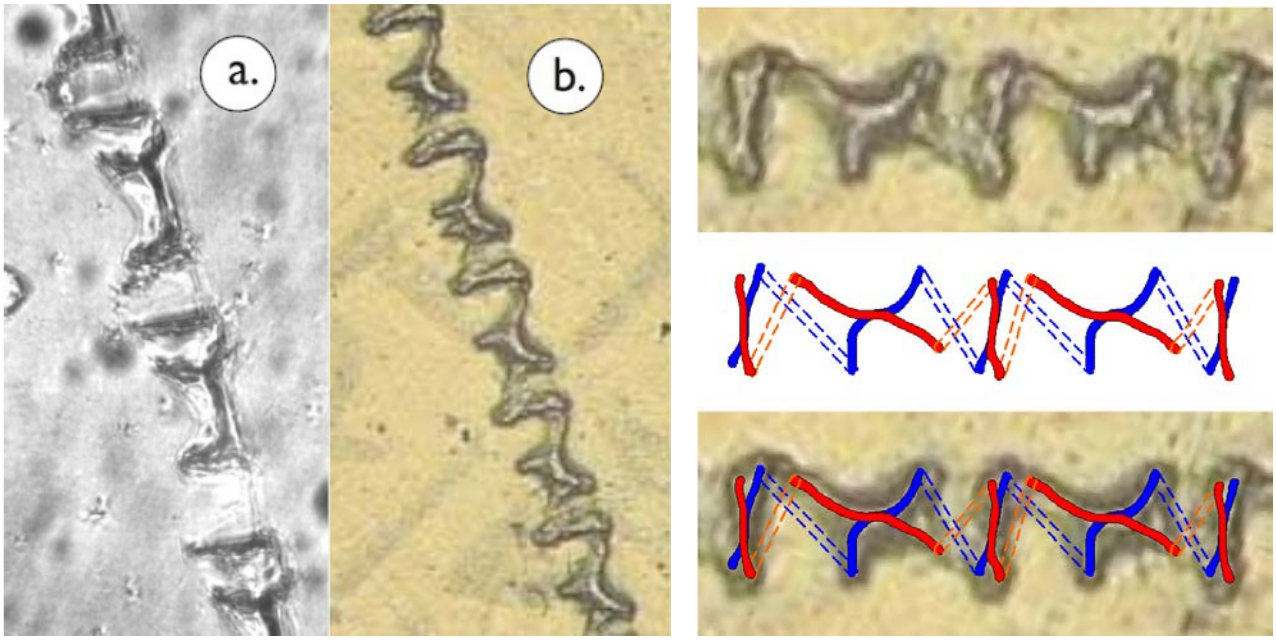

Figure 31 Sample images of CPs exhibiting the IXIXI pattern;
Left: a. Keith Fredericks, b. Rodinov/Savvatimova [36];
Right: Zoom-in from b. and the mapping to the basic structure of helical CPs

The following image is showing an example from K. Fredericks:

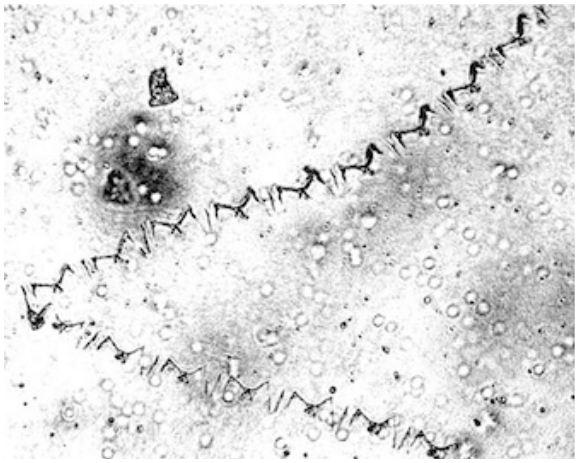

Figure 32 CP exhibiting the IMI pattern [36] [37]

It should be obvious, how Figure 32 is relating to the explanation of the IMI pattern in Figure 30.

Rail groups can transition to quasi-periodic structures, as can be seen below:

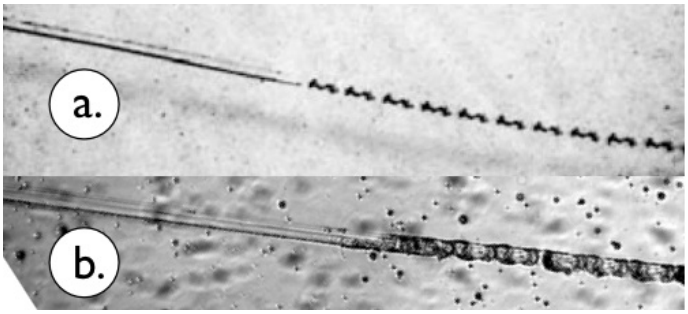

Figure 33 Rail group transitioning to a quasi-periodic structure [37].
a.: N. G. Ivoilov et al. (2006), b.: K. Fredericks

This transitioning can repeat back and forth several times within the same CP (not shown here, but evidenced by a 67-mm-long CP image captured by Bob Geenyer of the Martin Fleischman Memorial Project at a vibration plate of a Ryushin Omasa apparatus).

Figure 33 a. is leading to an important conclusion: The basic structure of quasi-periodic CPs as a two-layered closed-loop solenoid provides for a bidirectional electron transport. If, for example, the electrons move from left to right in the inner layer of the solenoid, they are moving from right to left in the outer layer. When this structure transitions to a rail group with two lines, the electron movement in these lines has to be antiparallel (i.e. in opposite directions), because one line has to carry the current of the inner layer and the other line has to carry the current of the outer layer of the solenoid.

In order to hypothetically explain the features of Figure 12 (i.e. tapering and parallelism) it is assumed that the two lines of the depicted rail group have a single-layer solenoid substructure (wound so fine that the turns are not visible). The current flow in these lines is helical, which is leading to a non-zero azimuthal (in regards to the solenoid axis) component of the magnetic field and a non-zero poloidal component of the magnetic field.

At short distances the repulsive forces of the azimuthal component of the magnetic field is dominating. At larger distances the attractive forces of the poloidal component of the magnetic field is domination. In result there is an equilibrium distance, at which the repulsive and the attractive forces are in equilibrium with each other. The equilibrium between these two forces is the mechanism, which keeps the lines of a rail group at constant distance to each other.

The following figure is illustrating the poloidal component of the magnetic field leading to magnetic attraction of the two lines:

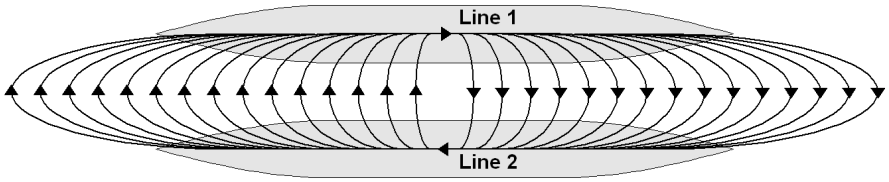

Figure 34 Schematics of a rail group with two lines and tapering.
The curved lines with arrows are depicting the poloidal magnetic field lines.

Hypothetically it is further assumed that the electric current in the two lines is becoming weaker towards the ends of the lines. In other words: Electrons can escape from the two parts of the CP core, are helically moving around the magnetic field lines, and reenter the other line. This way, the electron orbitals are closed loops, even though the two CP cores of the lines are not connected at the ends.

The electrons with the highest axial velocity will travel to the very end of the CPs cores, while the electrons with the smallest axial velocities will take the shortest loop path, because the magnetic trapping of the slow electrons is not strong enough for carrying them to the ends.

The observed tapering is therefore stemming from the reduction of the matter density and the reduced current towards the ends of the lines, which weakened the imprinting on the film.

2.9 Aperiodic Shapes

Sometimes CPs look like the random paths of Brownian motion:

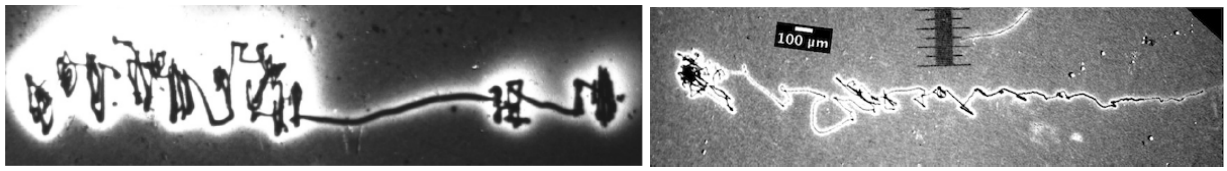

Aperiodic shapes of CPs [36] [37]

It is tempting to assume that the above lines were caused by the erratic movement of compact objects. However, this interpretation is proven wrong by the next image from K. Fredericks:

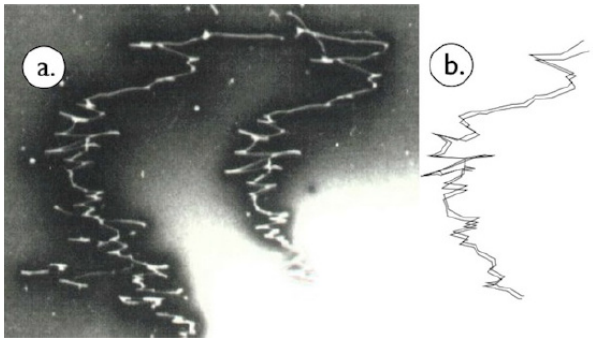

Figure 35 a.) Correlated shapes of aperiodic CPs; b.) Using a graphics editor, the shapes were traced from the original. The shapes when superimposed upon each other reveal very similar though not quite identical structure [36] [37]

The above image is showing a pair of lines, which are shaped almost identical. This can be explained by a CP splitting into two lanes. Both lanes are sharing the same set of quantum numbers of the electrons, which is leading to the observed "entanglement" of the shapes. In other words: The aperiodic lines are not "paths" of something, but are determined by the quantum state of the electrons in the CP.

There is another type of patterns documented by Keith Fredericks [36] [37]. He was calling them "vector swarms". The author cannot imagine that the "vector swarms" have anything to do with CPs. Are these scratches on the film surface?

2.10 Pulsed Anomalous Glow Discharge Device of the Correas

The LENR device built by Paulo and Alexandra Correa [21] [20] stands out in that it can create electrical energy directly from a LENR with no moving parts. This pulsed anomalous glow discharge (PAGD) device is shown below:

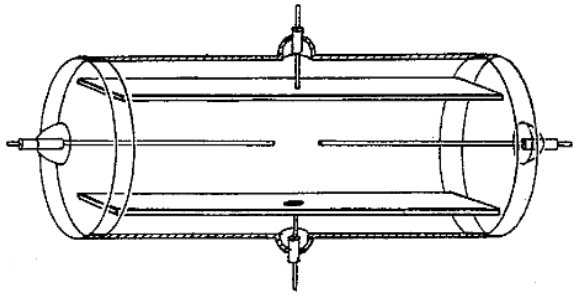

Figure 36 Pulsed anomalous glow discharge device
consisting of an evacuated glass tube with aluminum electrodes [21] [20]

The operating conditions are for example: Cathode surface area 100 cm^2, electrode distance 5 cm, pulsed discharge voltage 600 V, gas pressure 0.01 mbar, 10 pulses per second, input energy 10 J per pulse, output energy 100 J (electric) per pulse.

A snap shot of the glow discharge is shown below:

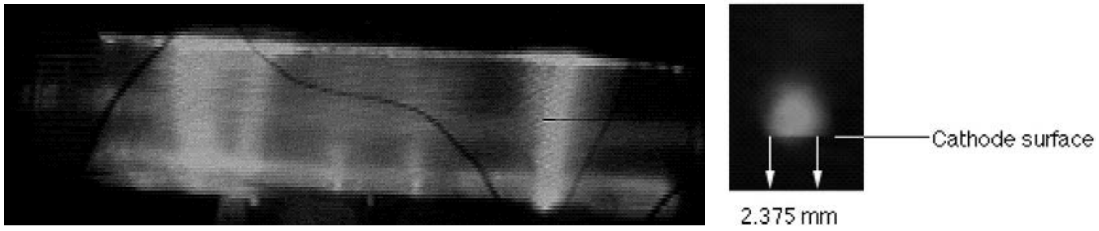

Figure 37 Left: The discharge plasma columns are emanated from small plasma balls at the cathode surface (bottom);
Right: The infrared image of a cathode plasma ball at the position of a cathode crater with a CP

Upon microscopic analysis the Correas found primary CP erosion craters on the cathode, where lots of fine radial lines came out. At the end of each radial line there was a little secondary crater. Additionally there were long smoothly curved lines, which were not always attached to the erosion craters:

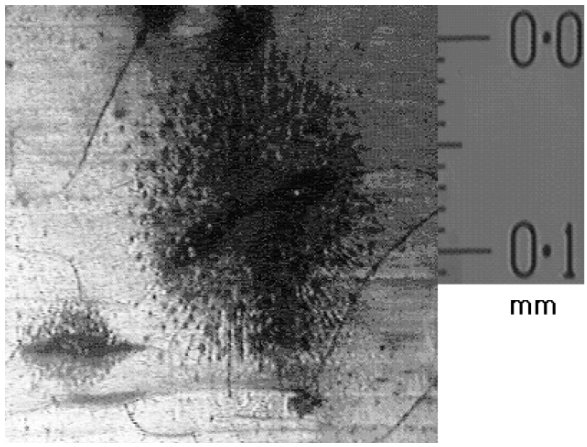

Figure 38 Smoothly curved lines and radial lines coming out of a primary crater on the an aluminum cathode

Some of the primary CP erosion craters were meandering over the surface, which is characteristic for the sausage type of CPs:

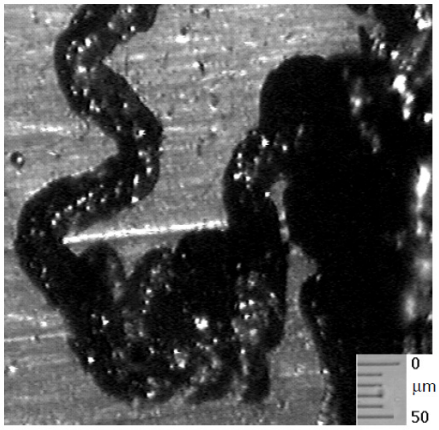

Figure 39 Sausage type CP craters on the cathode

The basic profile of a primary CP erosion crater is depicted below:

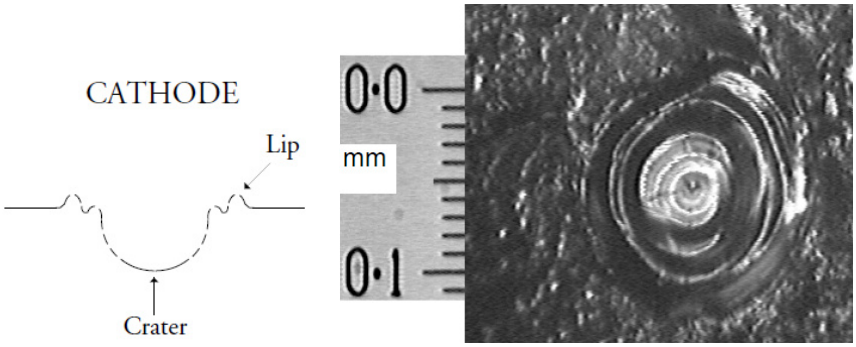

Figure 40 CP erosion crater on the cathode; Left: Cross section; Right: Photo

The material eroded away by the CPs was partially transported as core nuclei to the anode. Deposits on the anode in conjunction with peripheral ionization damage are shown in the following:

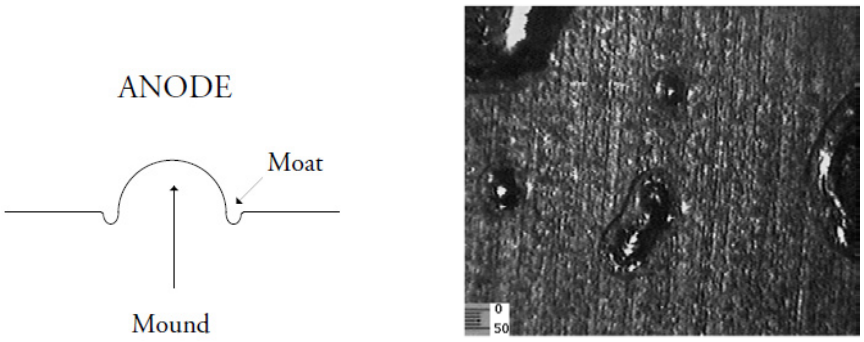

Figure 41 Deposits and ionization moat left by CP impacts on the anode; Left: Cross section; Right: photo

The long lines with smooth curvature visible in Figure 38 are believed to be CPs of the quasi-periodic shape. They could have been branched off of the sausage type CPs.

The many radial lines visible in Figure 38 are the remains of CPs, which were temporarily extending from the cathode to the anode. After each discharge the electric field between the electrodes reverses and the CPs are drifting back to the cathode. At the outer end points of the radial CP lines there are little secondary ionization craters. The radial CP lines probably also have a quasi-periodic shape.

There are two alternative explanations, how the PAGD device could generate electrical energy:

- Via nuclear energy feedback the current of each of the discharge pulses is continuing to flow in the initial direction after the external capacitor has been discharged and the electrode voltage has reversed its polarity. During this phase the discharge channel has a negative resistivity and is generating electric energy. This phase will end, when

the CPs are loosing contact to the electrodes. To repeat the effect, the polarity of the electrode voltage has to be reversed again by the next externally supplied electrical pulse and so on.

- Alternatively (or maybe additionally), the output of electrical energy of a PAGD device is stemming from fast electrons emitted by CPs at the cathode surface. Some of these electrons are reaching the anode and are causing a reversal of the potential between anode and cathode. In this reverse mode a current (and energy) can be extracted form the PAGD device as long as the CPs at the cathode are emitting electrons. After a while a new electric input pulse (in the original polarity) is required for keeping the CPs emitting electrons.

2.11 Cross section of a CP bundle

The next image is stemming from a plasma focus device of Winston Bostick:

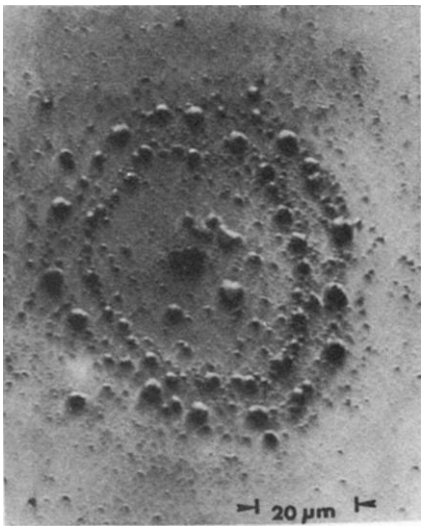

Figure 42 Coaxial structure from the impact of a CP bundle on a plastic target. The target was placed behind an axial aperture in the anode of a plasma focus device [33]

The image can be interpreted as the cross section of a large CP bundle. Plasma focus devices are creating lots of CPs (aka vortex filaments) in parallel, bundling them together in the so called plasma focus and discharging these CPs at the anode. If the anode contains an axial aperture (hole), the bundle can be shot against an arbitrary target, in this case plastics. Each CP of the bundle is depositing cathode material at the target visible as a little bump.

2.12 Plasma Vortex Reactor of Klimov

The research group of A. Klimov *et al.* was experimenting with plasma vortex reactors (PVR). In these reactors a swirl (vortex) of gas or water was producing a low-pressure zone at the axis, which was used as a high-voltage discharge channel for creating plasmoids. There was an AC discharge from a Tesla coil, which maintained a permanent plasma. Additionally, high-current pulsed recurring DC discharges were sent through in the conducting plasma. The DC pulses were creating CPs. The achieved COP was 2 to 10.

The following image is showing the operation of a PVR:

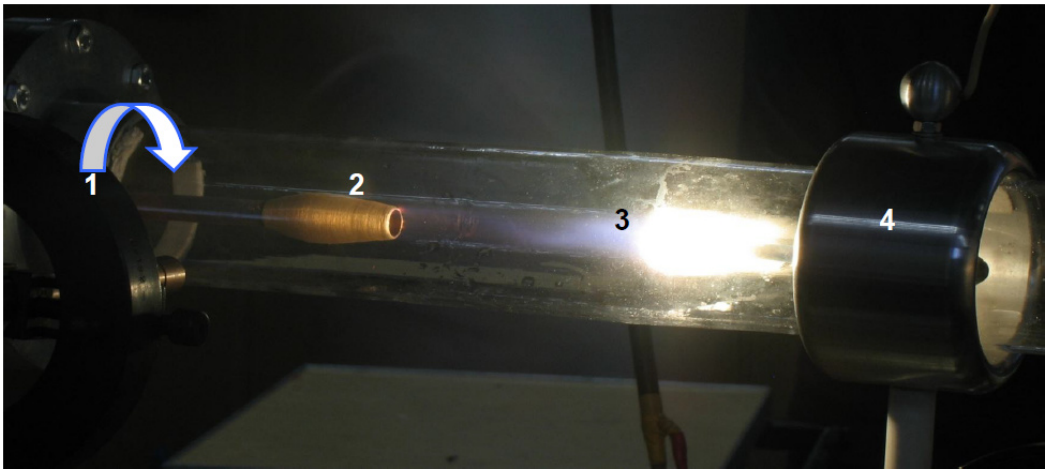

Figure 43 Plasma vortex reactor. Gas mixture Ar : H_20 = 10 :1;
Axial velocity equals tangential velocity of 30m/s, Gas pressure ~1.5 Bar;
1: swirl generator, 2: water steam injector, 3: CPs at the cathode surface, 4: cathode [31]

Each DC discharge pulse is creating a condensed plasmoid in the PVR extending from the cathode to the anode. The CPs can be seen as thin lines at the left side of the images:

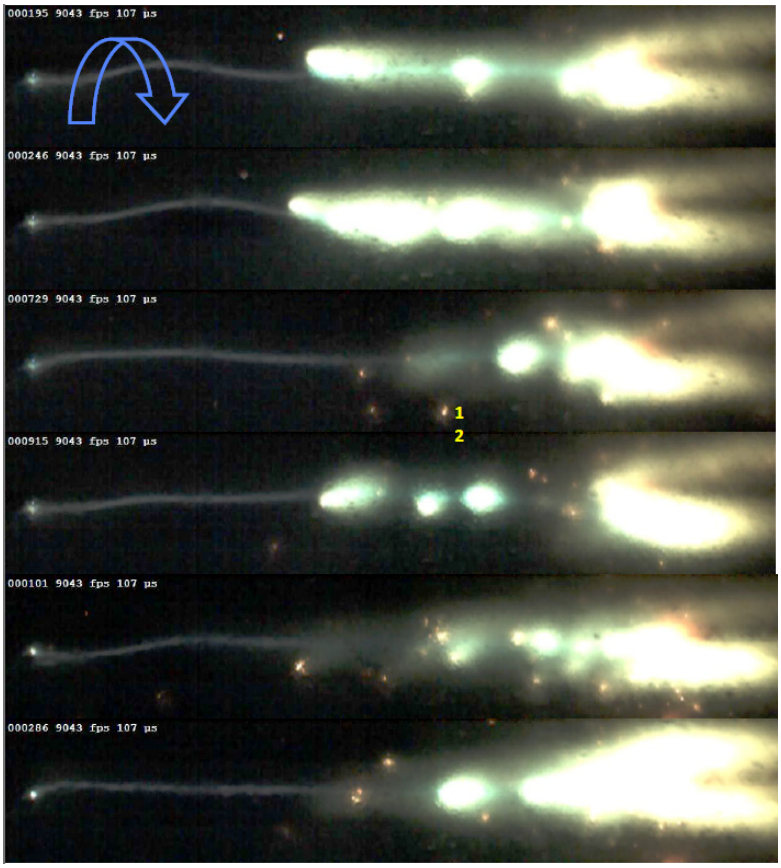

Figure 44 Frames from a high-speed video (2000 frames per second) of the PVR.
The anode was at the left side, the cathode was at the right side.
Open-ended CPs were extending from the cathode to the anode (thin line at the left side),
The CPs were closing to loops after the discharge pulse and were drifting
with the gas stream back to the cathode, which can be seen as glowing white objects.
The CPs were attaching to the cathode, which can be seen as a luminous mantle around the cathode. [31]

At the end of the DC discharge pulse the CPs were changing from an open-ended configuration to a closed-loop configuration and were drifting back and attaching to the cathode.

The CPs were causing the luminous plasma glow, which can be seen above. They were also eroding cathode material (nickel) and transporting some of it to the anode. The following is showing the erosion craters at the cathode:

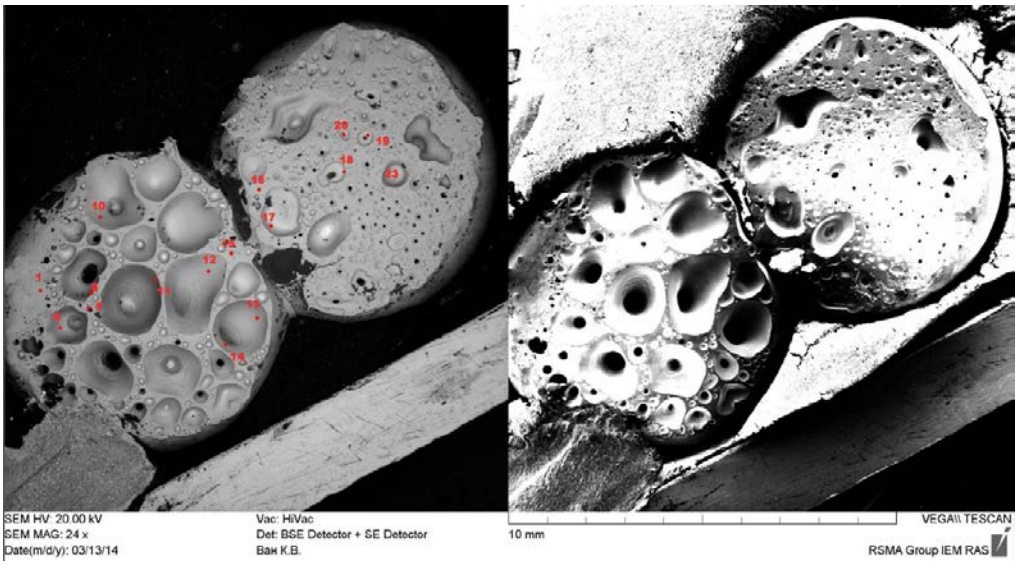

Figure 45 Erosion craters in the nickel cathode of the plasma vortex reactor of A. Klimov et al. [31]

The nickel deposits from CPs at the anode can be seen below:

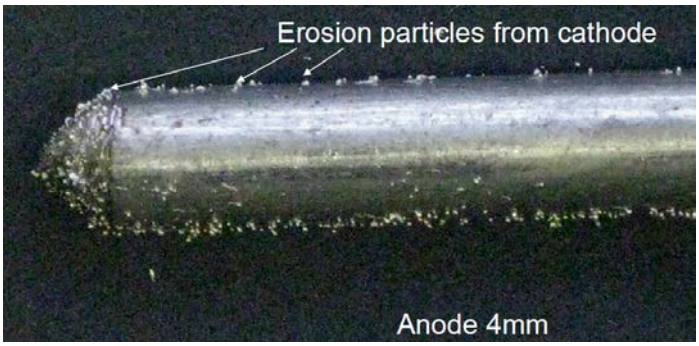

Figure 46 Nickel deposits left by CPs reaching the anode [31]

The CPs at the cathode were emitting the following x-ray spectrum:

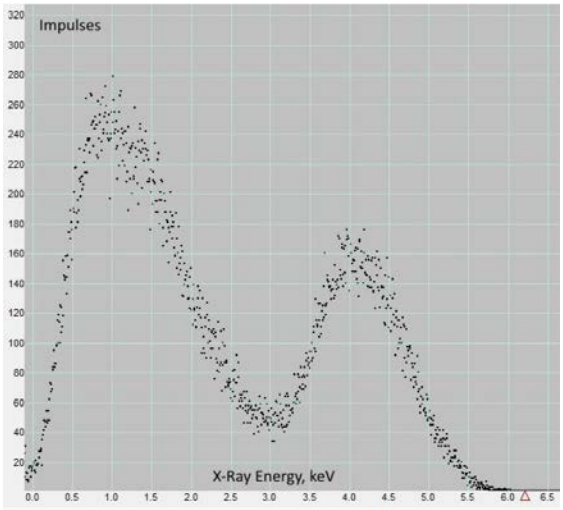

Figure 47 X-ray spectrum of CPs at the cathode [31]

This spectrum is evidence that the observed plasma is not merely a glow-discharge or an electric arc.

3 CP Quantum Mechanics

3.1 Basic Assumptions

Modeling of CPs is based on the following basic assumptions:

(78) CPs contain ensembles of atomic nuclei densely packed in a long and very narrow channel.

(79) The distances between the nuclei are so small that all electrons bound to these nuclei are delocalized along the channel. In other words: Even in their electronic ground state CPs don't consist of individual atoms. CPs rather form a quasi-one-dimensional plasma.

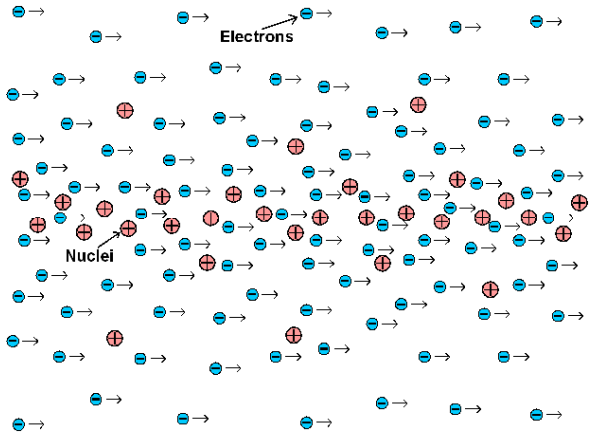

Figure 48 Basic model of a CP. The CP similarly extends to the left and to the right of this picture

3.2 The Cylindrical Model of CPs

The shape and quantum mechanical state of CPs can be very complicated. In order to obtain a simple quantum mechanical description of CPs, the following simplifications are used, which will subsequently be called "the cylindrical model of CPs":

(80) The CP is perfectly straight and cylindrically symmetric, i.e. it is not bent to rings, helices etc. The CP is oriented in parallel to and centered on the z-axis of the modeling cylindrical coordinate system.

(81) The CP has the length $\overline{L}$ and contains a total nuclear charge Q in its core.

(82) The electron wave functions of the CP are confined in the interval $0 \le z < \overline{L}$. At $z = \overline{L}$ these wave functions are continuously extended to their value and gradient at $z = 0$, as if the CP were a ring. However, this is meant to describe only the *circular boundary condition* of the wave functions at $z = \overline{L}$, not the shape of the CP.

(83) No external field is applied to the CP.

(84) A *jellium* model is used for the spatial distribution of the nuclear charge. This means, for the purpose of computing the spatial distribution of the electrons, the positive charges of the nuclei are modeled as a uniform "positive jelly" background, rather than point charges with distances in between. The nucleic charge density is assumed to be constant in axial and azimuthal direction, but it depends on the radial distance.

(85) However, correction terms will be used for computing the long-range Coulomb interaction, which are taking care of the jellium's short-range granularity (i.e. its point charge quality).

(86) The nucleic charge distribution of the jellium is modeled by means of a two-dimensional normal distribution in radial direction (or alternatively, by a distribution function, which is more aligned with the computed electron charge distribution). The standard deviation (or the alternative distribution function) is to be determined by variation, such that the total energy of the CP is minimized.

(87) The core area of the CP (i.e. the space defined by the extent of its electron orbitals) is surrounded by a charge compensation layer ("halo") consisting of cations. The charge of the halo compensates the surplus negative charges of the electrons in the core. The halo is modeled as a cylindrical shell of positive charge. The halo radius has to be larger than the core radius.

(88) The CP is assumed to reside in a vacuum. Interaction of the CP with surrounding matter is thus neglected.

(89) Only stationary states are modeled, as the goal is to describe the ground state of a CP. Consequently, the model assumes there is no electron scattering, i.e. there is no momentum transfer between electrons and the nuclei.

(90) For computing the repulsion energy among the nuclei, short-range corrections to the jellium model have to be made, which account for the granularity of the nuclear charges. In case the CP contains a mixture of different sorts of atomic nuclei, only the mean nuclear charge is taken into account for the corrections, rather than the individual nuclear charges.

(91) The time-independent Klein-Gordon equation is used for modeling the electron wave functions, thereby neglecting the magnetic moments of electron spins. The Klein-Gordon equation is taking care of the sizable relativistic effects occurring in CPs. (Clearly, the Dirac equation would be more adequate for modeling CPs. However, the involved complexities of such approach are avoided here.). For comparing the formulas and simulation results with the ones obtained from a non-relativistic Hamiltonian, also the Schrödinger equation is used.

(92) The magnetic field of the azimuthal electron orbits is neglected.

(93) Magnetic field from nuclear spins is neglected.

(94) The electron wave functions are modeled in an inertial frame of reference, where no magnetic field is created by any collinear movements of the nuclei. This simplification amounts to an approximation in cases where the nucleic velocities are position dependent.

(95) The multi-electron system is approximated by computing a collection of one-electron orbitals, whereby each electron orbital is subjected to the mean electric potential and magnetic vector potential created by the total charge density and total current density of all other occupied orbitals and the nuclei (independent particle model). The Pauli Exclusion Principle is used for determining orbital occupations of the ground state. Exchange and correlation energies are neglected.

(96) Quantum field theory is not engaged. Particle count is conserved.

(97) Eigenstates are excluded from occupation, where the corresponding total energy eigenvalue (including the electron's rest energy) of the electron is negative. This shall ensure that the mass defect per electron doesn't exceed the electrons rest energy.

(98) The kinetic energy of the electrons is always positive, i.e. states with a negative kinetic energy are ignored.

3.3 The Klein-Gordon Equation of a CP

Initial calculations of a CP with the Schrödinger equation have shown that the spectrum of the axial electron velocities can reach 80% of the speed of light. This provided a reason for engaging a relativistic Hamiltonian and a Lorentz-covariant quantum mechanical equation to model CPs.

Generally, the Dirac equation is regarded as the correct Lorentz-covariant equation for modeling fermions, especially when the effects resulting from the particle spin are of concern. Unfortunately, the Dirac equation involves 4-component wave functions and the solution of four coupled differential equations, resulting in sizeable mathematical and computational efforts.

Assuming that the electron spins have only minor effects on the formation energy, charge density, current density and other observables, the Klein-Gordon equation provides a Lorentz-covariant alternative to the Dirac equation for modeling the electrons of CPs. At the non-relativistic limit the Klein-Gordon equation is equivalent to the Schrödinger equation, while both equations share the deficiency of not modeling the spin.

In relativistic electrodynamics with so-called minimal coupling the Hamiltonian (total energy) of a particle with charge q moving in the presence of a static (external) electromagnetic potential is:

(99) $\hat{H} = c\sqrt{\left(\vec{P} - q\vec{A}\right)^2 + m_e{}^2 c^2} + q\Phi$, where c is the speed of light, Φ is the electric potential, $\vec{A}$ is the magnetic vector potential, $\vec{P} = \gamma m_e \vec{v} + q\vec{A}$ is the electron's canonical momentum, m_e is the electron rest mass and γ is the Lorentz factor

By defining $\overline{E} \equiv \hat{H} - m_e c^2$ as being the total energy minus the rest energy and by using $q = -e$ as the charge of an electron, (99) is leading to the following equation for an electron in a static electromagnetic potential:

(100) $\overline{E} = c\sqrt{\left(\vec{P} + e\vec{A}\right)^2 + {m_e}^2 c^2} - m_e c^2 - e\Phi$, where e is the elementary charge

Therefore:

(101) $\left(\overline{E} + e\Phi + m_e c^2\right)^2 = \left(c\vec{P} + ec\vec{A}\right)^2 + {m_e}^2 c^4$

All formulas are written in SI units, unless otherwise noted. Throughout this document, energy symbols with a bar on top (e.g. $\overline{E}$) denote that the energy is measured in Joule. Energy symbols without a bar on top denote that the energy is measured in units of the Hartree energy (192), i.e. the energy is a dimensionless quantity in the respective formula. Likewise, other symbols with a bar (e.g. $\overline{\sigma}$, $\overline{J}_z$, $\overline{p}_z$, $\overline{P}_z$ and $\overline{A}_z$) are in SI units, while its counterparts without the bar are in natural units (i.e. dimensionless).

By quantizing the canonical momentum via the Del operator $\vec{P} \equiv -i\hbar\nabla$ and applying both sides to an electron wave function Ψ, equation (101) transforms to the **stationary Klein-Gordon equation of an electron in a static electromagnetic potential**:

(102) $\left(\overline{E} + e\Phi + m_e c^2\right)^2 \Psi = \left[\left(-i\hbar c\nabla + ec\vec{A}\right)^2 + {m_e}^2 c^4\right] \Psi$, where
$\hbar$ is the reduced Planck constant and $i = \sqrt{-1}$

Due to simplification (96), Ψ is called here a "wave function", rather than a "quantum field".

The term $\overline{E} + m_e c^2$ represents the total energy of the electron. Usually the Klein-Gordon equation is written, such that the total energy is sought as the eigenvalue of this differential equation. However, this document deviates from the customary approach. Instead, the quantity $\overline{E}$ is sought here as the eigenvalue (both approaches are equivalent in their results).

Some authors prefer the term "relativistic Schrödinger equation" for (102), insisting that the Klein-Gordon equation is different. Here, these terms are used interchangeably.

In quantum mechanics a multi-electron system is correctly described by a single wave function $\Psi\left(\vec{r}_1, \vec{r}_2, ...\vec{r}_N\right)$ depending on the positions of the N electrons. The multi-electron wave function is usually formed by a Slater determinant (or a linear combination of several Slater determinants) to ensure anti-symmetry and the Pauli Exclusion Principle.

According to simplification (95) a rigorously simpler approach is used here for modeling CPs, requiring only moderate compute power:

So, instead of using a multi-electron Klein-Gordon equation describing the pair-wise interaction between N electrons, the cylindrical model uses $\boldsymbol{N}$ **single-electron Klein-Gordon equations with** $\boldsymbol{N}$ **wave functions** $\Psi\left(\vec{r}\right)$, each describing a single electron in the **mean potential** of all other electrons and the nuclei.

Of course, this is merely an independent particle approximation. For example, the approach doesn't account for the exchange energy and the correlation energy usually deemed important in quantum chemistry.

At first glance this looks still challenging to compute, because there are N Klein-Gordon equations to be solved. Fortunately, large numbers of these equations can be computed in groups, because they produce nearly the same charge density distributions and current density distributions.

Expanding the right side of (102) and using $\nabla \cdot \vec{A} = 0$ (Lorentz gauge in the static case) yields:

(103) $\left(\overline{E} + e\Phi + m_e c^2\right)^2 \Psi = \left(-\hbar^2 c^2 \nabla^2 - 2i\hbar e c^2 \vec{A} \cdot \nabla + e^2 c^2 \vec{A} \cdot \vec{A} + {m_e}^2 c^4\right)\Psi$

A kinetic momentum operator is defined here as:

(104) $\hat{p} = -i\hbar\nabla + e\vec{A}$

The expectation value of $\hat{p}$ equals $\langle\gamma\rangle m_e\langle\vec{v}\rangle$ (hence the name "kinetic momentum"), $\langle\vec{v}\rangle$ is the expectation value of the electron's group velocity and $\langle\gamma\rangle = \langle 1+(\overline{E}+e\Phi)/(m_e c^2)\rangle$ is the expectation value of the local Lorentz factor.

Using (104) in (103) yields:

(105) $\left(\overline{E}+e\Phi+m_e c^2\right)^2\Psi = \left(c^2\hat{p}^2+{m_e}^2c^4\right)\Psi$, where $c^2\hat{p}^2 = -\hbar^2c^2\nabla^2 - 2i\hbar ec^2\vec{A}\cdot\nabla + e^2c^2\vec{A}\cdot\vec{A}$

According to simplification (91) and (92) the magnetic field of the electron spins and of the azimuthal movement of the electrons is neglected. Thus the only source of the magnetic field is the current carried by the electrons moving in z-direction. Therefore, the vector potential is everywhere oriented in z-direction:

(106) $\vec{A} = \overline{A}_z\vec{e}_z$

The Laplace operator expands in cylindrical coordinates as following:

(107) $\nabla^2 = \frac{1}{\rho}\frac{\partial}{\partial\rho}\left(\rho\frac{\partial}{\partial\rho}\right)+\frac{1}{\rho^2}\frac{\partial^2}{\partial\varphi^2}+\frac{\partial^2}{\partial z^2}$, where ρ is the radial distance from the z-axis, φ is the azimuth and z is the coordinate of the z-axis

Inserting (106) and (107) into equation (103) and dividing both sides by $2m_e c^2$ results in **the stationary Klein-Gordon equation of an electron in the mean potential of a CP's all other electrons and the nuclei**:

(108) $$\left\{\frac{-\hbar^2}{2m_e}\left[\frac{1}{\rho}\frac{\partial}{\partial\rho}\left(\rho\frac{\partial}{\partial\rho}\right)+\frac{1}{\rho^2}\frac{\partial^2}{\partial\varphi^2}+\frac{\partial^2}{\partial z^2}+2\frac{e\overline{A}_z}{\hbar}i\frac{\partial}{\partial z}-\frac{e^2{\overline{A}_z}^2}{\hbar^2}\right]-\frac{m_e c^2}{2}\left(\frac{\overline{E}+e\Phi}{m_e c^2}+1\right)^2+\frac{m_e c^2}{2}\right\}\Psi = 0$$

With simplification (83) the electric potential Φ is depending solely on the electron charge density $\overline{\sigma}_e(\rho)$ and the nuclear charge density $\overline{\sigma}_n(\rho)$. The magnetic vector potential $\overline{A}_z$ is solely depending on the electric current density $\overline{J}_z(\rho)$. The electron charge density and the electric current density are derived from the modulus square of the other electron's wave functions.

This approach has **similarities with the density functional theory (DFT)** used in quantum chemistry modeling, except that the exchange and correlation energies are not accounted for. Equation (108) therefore can be seen as the Kohn-Sham equation. However, the influence of the magnetic field on the co-linear electron-electron interaction is maintained and the Pauli Exclusion Principle will be obeyed during orbital occupation.

3.4 Boundary Conditions for Solutions of the Klein-Gordon Equation

Care must be taken according to simplification (97) that **the total energy $\overline{E}+m_e c^2$ of an eigenstate is always positive**, therefore:

(109) $\overline{E} > -m_e c^2$

Requirement (109) can be fulfilled by **excluding eigenstates with a negative total energy during orbital occupation**.

The wave function amplitude must disappear at infinite radial distances:

(110) $\lim_{\rho\to\infty}\Psi(\rho) = 0$

As required by simplification (82) the wave function has to meet circular boundary conditions:

(111) $\Psi(z=0) = \Psi(z=\overline{L})$ and

(112) $$\frac{\partial\Psi(z=0)}{\partial z}=\frac{\partial\Psi(z=\overline{L})}{\partial z}$$

For computing observables the Klein-Gordon electron wave functions have to be **normalized** such that:

(113) $$1=\|\Psi\|=\iiint_{\mathbf{R}^3}|\Psi|^2\,d\vec{r}$$

3.5 Observables of the Klein-Gordon Electron Wave Function

The potential energy of an electron is solely stemming from the Coulomb field:

(114) $$\overline{E}_{pot}(\vec{r})=-e\Phi(\vec{r})$$

The local kinetic energy of the electron is what's left when the potential energy is subtracted from $\overline{E}$:

(115) $$\overline{E}_{kin}(\vec{r})=\overline{E}+e\Phi(\vec{r})$$

The **volume charge density distribution of electron number** i in a static electromagnetic potential computes as following:

(116) $$\overline{\sigma}_{e,i}=-e|\Psi_i|^2$$

Summing this up for all N electrons of the CP and using modulus square factorization (148) results in:

(117) $$\overline{\sigma}_e=-e\sum_{i=1}^{N}|\Psi_i|^2=-\frac{e}{2\pi\overline{L}}\sum_{i=1}^{N}|\Psi_{\rho,i}|^2\,,$$ where $\Psi_{\rho,i}$ is the radial wave function of electron number i

The **current density distribution of electron number** i in a static electromagnetic potential computes as following:

(118) $$\vec{\overline{J}}_i=\frac{-e}{m_e}\left[-\frac{i\hbar}{2}\left(\Psi_i^*\nabla\Psi_i-\Psi_i\nabla\Psi_i^*\right)+e\vec{A}|\Psi_i|^2\right]$$

Summing (118) up for all N electrons of the CP provides:

(119) $$\vec{\overline{J}}=\frac{-e}{m_e}\sum_{i=1}^{N}\left[-\frac{i\hbar}{2}\left(\Psi_i^*\nabla\Psi_i-\Psi_i\nabla\Psi_i^*\right)+e\vec{A}|\Psi_i|^2\right]$$

Using product ansatz (146), modulus square factorization (148) and Ψ_z-solution (152), the **z-component** (in cylindrical coordinates) **of the current density** (119) in a CP computes as:

(120) $$\overline{J}_z=\frac{-e}{m_e}\sum_{i=1}^{N}\left[-\frac{i\hbar}{2}\left(\Psi_i^*\frac{\partial\Psi_i}{\partial z}-\Psi_i\frac{\partial\Psi_i^*}{\partial z}\right)+e\overline{A}_z|\Psi_i|^2\right]$$
$$=\frac{-e}{2\pi m_e\overline{L}}\sum_{i=1}^{N}\overline{p}_{z,i}|\Psi_{\rho,i}|^2\,,\text{ where}$$

(121) $$\overline{p}_{z,i}=\overline{P}_{z,i}+e\overline{A}_z=\hbar k_i+e\overline{A}_z$$ is the **z-component of the electron's kinetic momentum** $\hat{p}$

When (117), (119) and (120) will be used for determining the electric and magnetic potentials in the Klein-Gordon equation (108), the electron number i is incorrectly exposed also to its own potential. However, this error is quite small, if the CP contains very many electrons.

The total **current** in z-direction carried by all electrons of the CP can be computed by integrating (120) over all radius values and azimuth values:

$$(122)\quad I_z = \int_{\varphi=0}^{2\pi}\int_{\rho=0}^{\infty} \bar{J}_z(\rho)\rho d\rho d\varphi = \frac{-e}{m_e \bar{L}} \int_0^{\infty} \sum_{i=1}^{N} \bar{p}_{z,i} \left|\Psi_{\rho,i}(\rho)\right|^2 \rho d\rho$$

$$= \frac{-e}{m_e \bar{L}} \sum_{i=1}^{N} \int_0^{\infty} \left[\hbar k_i + e\bar{A}_z(\rho)\right] \left|\Psi_{\rho,i}(\rho)\right|^2 \rho d\rho$$

The expectation value of the **electron group velocity's z-component** (averaged over all N electrons of the CP) can be computed from the z-component of the total current:

$$(123)\quad \langle v_z \rangle = \frac{I_z \bar{L}}{-Ne}$$

The **expectation value of the electron orbit radius** for eigenstates of equation (108) is:

$$(124)\quad \langle \rho \rangle = \int_0^{\infty} |\Psi|^2 \rho^2 d\rho$$

Throughout this document the term "formation energy" is used instead of "negative binding energy". Both terms are supposed to mean the same thing: The energy it takes to form a CP from isolated electrons and nuclei. A positive formation energy therefore denotes that the formation of the CP is endothermic, i.e. it requires energy from an external source.

One could naively assume that the **total formation energy** $\bar{E}_B$ of a CP is the sum of the energy eigenvalues of all electrons plus the nuclear self-repulsion energy:

(125) $\bar{E}_B \neq \bar{E}_n + \sum_{i=1}^{N} \bar{E}_i$, where $\bar{E}_i$ is the energy eigenvalue of electron number i and $\bar{E}_n$ is the nuclear self-repulsion energy defined in (161)

However, this approach would count the electron-electron interaction energies $\langle \bar{E}_{C,e} \rangle_i$ twice, because the electrons are interacting among themselves.

Instead, one needs to subtract half of $\langle \bar{E}_{C,e} \rangle_i$ from the eigenvalues $\bar{E}_i$ before summation:

$$(126)\quad \bar{E}_B = \bar{E}_n + \sum_{i=1}^{N} \left(\bar{E}_i - \frac{1}{2} \langle \bar{E}_{C,e} \rangle_i \right),$$

where $\langle \bar{E}_{C,e} \rangle_i = \langle -e\Phi_e \rangle_i$ is the expectation value of the electron-electron Coulomb energy for electron number i and Φ_e is the potential of all electrons

A CP resembles a microstrip, if it is attached to the surface of a dielectric plate, which has a conducting return plane attached at the other side. Therefore, microstrip formulas can be used for approximating the characteristic impedance, the capacitance and the inductance of a CP. For this purpose the following assumptions are made:

(127) $\langle \rho \rangle_{mean} << h << \bar{L}$, where $\langle \rho \rangle_{mean}$ is the expectation value of the electron radius averaged over all electrons, h is the thickness of the dielectric plate and $\bar{L}$ is the length of the CP

The **characteristic impedance of a CP** (in microstrip geometry) can be approximated by:

(128) $Z_0 \approx \frac{1}{2\pi} \sqrt{\frac{\mu_0}{\varepsilon_0 \varepsilon_{eff}}} \ln\left(\frac{2h}{\langle \rho \rangle_{mean}} \right)$, where h is the thickness of the dielectric plate

The effective dielectric constant can be approximated as:

(129) $\varepsilon_{eff} \approx \frac{\varepsilon_r + 1}{2}$, where ε_r is the relative permittivity

The **capacitance of a CP** (in microstrip geometry) can be approximated by:

(130) $C \approx \frac{2\pi\varepsilon_0\varepsilon_{eff}\overline{L}}{\ln\left(2h/\langle\rho\rangle_{mean}\right)}$, where ,

The **inductance of a CP** (in microstrip geometry) can be approximated by:

(131) $\Lambda \approx Z_0{}^2 C \approx \frac{\mu_0\overline{L}}{2\pi}\ln\left(\frac{2h}{\langle\rho\rangle_{mean}}\right)$

3.6 Electromagnetic Potential and Field of a CP

The electric potential of a CP splits as follows:

(132) $\Phi = \Phi_n + \Phi_e + \Phi_{G,e} + \Phi_h$, where Φ_n is the electric potential of the nuclear jellium in the core according to simplification (84) and (85), Φ_e is the electric potential of the electrons, $\Phi_{G,e}$ is the granularity correction of electron-nucleus interaction (171) and Φ_h is the electric potential of the halo (177).

As a tool for computing the electromagnetic potential the following geometry is analyzed:

A sample charge at distance ρ from the z-axis (origin) and azimuth φ shall act as the point of measurement for vector potential A_z and the electric potential Φ.

The following figure illustrates this further:

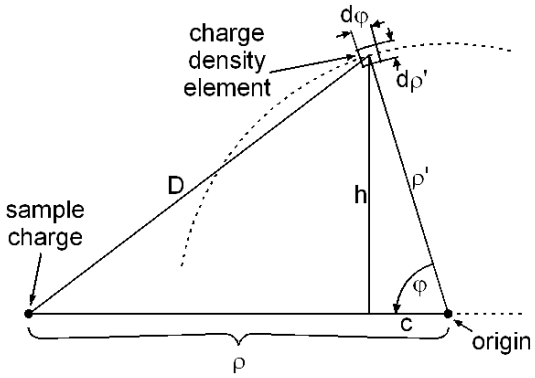

Figure 49 Scheme for computing the electromagnetic potential. This shows a cut perpendicular to the z-axis.

From the geometry of Figure 49 it can be concluded:

(133) $c = \rho'\cos\varphi$

(134) $h = \rho'\sin\varphi$

(135) $D = \sqrt{(\rho - c)^2 + h^2} = \sqrt{(\rho - \rho'\cos\varphi)^2 + \rho'^2\sin^2\varphi} = \sqrt{\rho'^2 - 2\rho'\rho\cos\varphi + \rho^2}$

The following figure shall illustrate the geometry in z-direction:

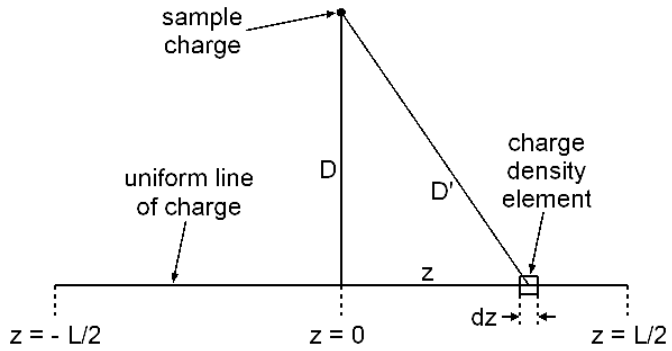

Figure 50 Scheme for computing the electromagnetic potential. This shows a cut in parallel to the z-axis.

From Figure 50 it can be concluded:

(136) $D' = \sqrt{z^2 + D^2}$

Figure 50 shows an infinitesimal thin line of charge extending from $z = -\overline{L}/2$ to $z = \overline{L}/2$. This line is in parallel to the z-axis. The volume charge density $\overline{\sigma}(\rho')$ is constant along the line.

An infinitesimal charge density element with a volume of $\rho' d\rho' d\varphi dz$ contains a charge of:

(137) $dQ = \overline{\sigma}(\rho')\rho' d\rho' d\varphi dz$, where

(138) $\overline{\sigma}(\rho') = \overline{\sigma}_n(\rho') + \overline{\sigma}_e(\rho') + \overline{\sigma}_h(\rho')$, i.e. the sum of the nuclear charge density in the core, the electron charge density and the charge density of the halo (176)

The electric potential at distance D from the infinitesimal line of charge and at axial position $z = 0$ computes as following:

(139) $$d\Phi(D) = \frac{1}{4\pi\varepsilon_0}\int_{-\overline{L}/2}^{\overline{L}/2}\frac{dQ}{D'} = \frac{1}{4\pi\varepsilon_0}\overline{\sigma}(\rho')\rho' d\rho' d\varphi 2\int_0^{\overline{L}/2}\frac{1}{\sqrt{z^2 + D^2}}dz$$

$$= \frac{1}{4\pi\varepsilon_0}\overline{\sigma}(\rho')\rho' d\rho' d\varphi 2\ln\frac{\overline{L}/2 + \sqrt{(\overline{L}/2)^2 + D^2}}{D}$$

Inserting (135) into (139) and integrating over ρ' and φ yields the contribution of the entire CP to the **electric potential** (in Lorentz gauge, static case):

(140) $\Phi(\rho) = \frac{1}{4\pi\varepsilon_0}\int_0^{\infty}\overline{\sigma}(\rho')G(\rho,\rho')\rho' d\rho'$, where

(141) $G(\rho,\rho') = 2\int_0^{2\pi}\ln\frac{\overline{L}/2 + \sqrt{(\overline{L}/2)^2 + \rho'^2 - 2\rho'\rho\cos\varphi + \rho^2}}{\sqrt{\rho'^2 - 2\rho'\rho\cos\varphi + \rho^2}}d\varphi$ is the geometry integral

The geometry integral can be solved by considering Gauss's law and by using the fact that the charge distribution is rotationally symmetric around the z-axis. For the case $\rho \le \rho'$ there is $G(\rho,\rho') = G(\rho',0)$. For the case $\rho > \rho'$ there is $G(\rho,\rho') = G(\rho,0)$:

(142) $$G(\rho,\rho') = \begin{cases} 4\pi\left[\ln\left(\overline{L}/2 + \sqrt{\overline{L}^2/4 + \rho'^2}\right) - \ln\rho'\right] & \text{for } \rho \le \rho' \\ 4\pi\left[\ln\left(\overline{L}/2 + \sqrt{\overline{L}^2/4 + \rho^2}\right) - \ln\rho\right] & \text{for } \rho > \rho' \end{cases}$$

Replacing $\overline{\sigma}(\rho')/\varepsilon_0$ with $\mu_0 \overline{J}_z(\rho')$ in (140) provides the z-component of the CP's **magnetic vector potential** (in Lorentz gauge, static case):

(143) $$\overline{A}_z(\rho) = \frac{\mu_0}{4\pi}\int_0^\infty \overline{J}_z(\rho')G(\rho,\rho')\rho' d\rho' = -\frac{e\mu_0}{8\pi^2 m_e \overline{L}}\int_0^\infty \sum_{i=1}^{N}\left[\overline{P}_{z,i} + e\overline{A}_z(\rho')\right]\left|\Psi_{\rho',i}\right|^2 G(\rho,\rho')\rho' d\rho',$$

where μ_0 is the vacuum permeability, $\overline{J}_z(\rho')$ is the z-component of the current density and $\overline{P}_{z,i} = \hbar k_i$ is the z-component of the electron's canonical momentum

Note that $\overline{A}_z$ is depending on itself in equation (143). Therefore, the values of $\overline{A}_z$ and $\overline{J}_z$ need to be determined iteratively until self-consistency.

Based on the circular boundary condition (82) the electric potential (140) and the vector potential (143) are made to be constant in z-direction. This approximation is required for maintaining the full cylindrical symmetry of the model.

The radial and azimuthal (see simplification (92)) components of the vector potential and the current density are zero everywhere. Due to simplification (94) the nuclear jellium is not contributing to the current density.

Note that $\lim_{\rho\to\infty} \Phi(\rho) = 0$ and $\lim_{\rho\to\infty} \overline{A}_z(\rho) = 0$. Equations (140) and (143) therefore can be used for determining the formation energy of electrons to a CP without engaging a non-zero reference potential.

The **radial electric field** of a CP computes as:

(144) $$\varepsilon_\rho = -\frac{\partial}{\partial\rho}\Phi(\rho)$$

The **azimuthal magnetic field** of a CP computes as:

(145) $$B_\varphi = -\frac{\partial}{\partial\rho}\overline{A}_z(\rho)$$

3.7 Product Ansatz

The following **product ansatz** is made to factorize the electron wave function:

(146) $\Psi(\rho,\varphi,z) = \Psi_\rho(\rho)\Psi_\varphi(\varphi)\Psi_z(z)$ or in short: $\Psi = \Psi_\rho\Psi_\varphi\Psi_z$

The wave function of a single electron is supposed to be normalized and it represents a stationary state. In azimuthal direction and in axial direction the electromagnetic potential is constant. Therefore the modulus square of Ψ_φ and Ψ_z is also constant:

(147) $$\left|\Psi_\varphi\right|^2 = \Psi_\varphi^*\Psi_\varphi = \frac{1}{2\pi} \text{ and } \left|\Psi_z\right|^2 = \Psi_z^*\Psi_z = \frac{1}{\overline{L}}$$

Hence the **modulus square** of the entire wave function factorizes as:

(148) $$\left|\Psi\right|^2 = \Psi_\rho^*(\rho)\Psi_\rho(\rho)\Psi_\varphi^*(\varphi)\Psi_\varphi(\varphi)\Psi_z^*(z)\Psi_z(z) = \frac{1}{2\pi\overline{L}}\left|\Psi_\rho(\rho)\right|^2$$

The **normalization criteria** (113) could then be carried out as:

(149) $$1 = \left\|\Psi\right\| = \int_0^\infty \left|\Psi_\rho(\rho)\right|^2 \rho d\rho$$

3.8 Separation of the Klein-Gordon Equation

With product ansatz (146) the partial derivatives of the wave function are:

$$(150)\quad \frac{\partial\Psi}{\partial\rho}=\Psi_\varphi\Psi_z\frac{d\Psi_\rho}{d\rho}\ \text{and}\ \frac{\partial\Psi}{\partial\varphi}=\Psi_\rho\Psi_z\frac{d\Psi_\varphi}{d\varphi}\ \text{and}\ \frac{\partial\Psi}{\partial z}=\Psi_\rho\Psi_\varphi\frac{d\Psi_z}{dz}$$

Inserting this into the equation (108) and dividing both sides by Ψ yields:

$$(151)\quad -\frac{\hbar^2}{2m_e}\left[\frac{1}{\rho\Psi_\rho}\frac{d}{d\rho}\left(\rho\frac{d\Psi_\rho}{d\rho}\right)+\frac{1}{\rho^2\Psi_\varphi}\frac{d^2\Psi_\varphi}{d\varphi^2}+\frac{1}{\Psi_z}\frac{d^2\Psi_z}{dz^2}+2\frac{e\overline{A}_z}{\hbar\Psi_z}i\frac{d\Psi_z}{dz}-\frac{e^2\overline{A}_z{}^2}{\hbar^2}\right]$$
$$-\frac{m_ec^2}{2}\left(\frac{\overline{E}+e\Phi}{m_ec^2}+1\right)^2+\frac{m_ec^2}{2}=0$$

Remark for the mathematical purity: The division by Ψ is done here out of convenience. It could have been postponed to a later step without affecting the end result, such that wave functions (which can have zeros) never show up in the denominator.

The following **wave function is solving the z-dependent part** of (151):

$$(152)\quad \Psi_z=\sqrt{\frac{1}{\overline{L}}}e^{ikz},\ \text{where}\ k\in\mathbf{R}$$

Due to simplification (82) the energy eigenvalues are quantized to a discrete spectrum, because wave number k has to meet the following boundary condition:

$$(153)\quad k=l\frac{2\pi}{\overline{L}},\ \text{where}\ l\in\mathbf{Z}$$

Integer l acts as an **axial quantum number** here (This quantum number l should not be confused with the l in Laplace's spherical harmonic function $Y_l^m(\theta,\varphi)$ used for modeling the electrons of atoms).

The following **wave function is solving the φ-dependent part** of (151):

$$(154)\quad \Psi_\varphi=\sqrt{\frac{1}{2\pi}}e^{im\varphi},\ \text{where}\ m\in\mathbf{Z}$$

Integer m is the **azimuthal quantum number**.

Inserting (121), (152) and (154) into (151) provides the **radial Klein-Gordon equation** of a CP:

$$(155)\quad \left\{\frac{\hbar^2}{2m_e}\left[-\frac{1}{\rho}\frac{d}{d\rho}\left(\rho\frac{d}{d\rho}\right)+\frac{m^2}{\rho^2}\right]+\frac{\overline{p}_z{}^2}{2m_e}-\frac{m_ec^2}{2}\left(\frac{\overline{E}+e\Phi}{m_ec^2}+1\right)^2+\frac{m_ec^2}{2}\right\}\Psi_\rho=0$$

At the **non-relativistic limit** the term $x=\left(\overline{E}+e\Phi\right)/\left(m_ec^2\right)$ approaches zero. By using only the first two terms of the Taylor series of $(x+1)^2$ about $x=0$ one can approximate:

$$(156)\quad (x+1)^2\approx 1+2x$$

With this approximation equation (155) becomes the **radial Schrödinger equation** of a CP:

$$(157)\quad \left\{\frac{\hbar^2}{2m_e}\left[-\frac{1}{\rho}\frac{d}{d\rho}\left(\rho\frac{d}{d\rho}\right)+\frac{m^2}{\rho^2}\right]+\frac{\overline{p}_z{}^2}{2m_e}-\overline{E}-e\Phi\right\}\Psi_\rho=0$$

The radial Schrödinger equation (157) is based on the **non-relativistic Hamiltonian** for an electron in an electromagnetic field with minimal coupling:

$$(158)\quad \hat{H} = \frac{\left(-i\hbar\nabla + e\vec{A}\right)^2}{2m_e} - e\Phi = \frac{\left(\vec{P} + e\vec{A}\right)^2}{2m_e} - e\Phi$$

The eigenstates of differential equation (155) or (157) provide the radial wave functions Ψ_ρ. The eigenvalues $\overline{E}$ of bound states are discrete, i.e. they are countable by a principal quantum number n, the azimuthal quantum number m and the axial quantum number l. The **principal quantum number** $n = 1, 2, 3, \ldots$ is defined here analogous to the hydrogen atom: n equals one plus the number of node lines of $\Psi_\rho\Psi_\varphi$, therefore $n \geq |m| + 1$ (In a stricter sense, Ψ_φ has no node lines. However, a standing wave of two superposed azimuthal wave functions, differing only in the sign of quantum number m, has m node lines.)

Principal quantum number n has no explicit representation in (155) or (157) or in any of the following formulas. It is useful however, as an ordering scheme for computational results.

One has to keep in mind that the eigenvalues $\overline{E}$, the eigenstates Ψ_ρ, Ψ_φ and Ψ_z, as well as the quantum numbers n, m and l are generally distinct for each electron of the CP. In order to ease readability, the electron number as an index has been omitted from these symbols, unless the index is needed in a summation.

3.9 The Jellium Model of the Nuclear Charge Distribution

According to simplification (84) the charge of the nuclei is treated as if it were a uniform "positive jelly" background, rather than point charges with distances in between.

The nuclear charge density distribution $\overline{\sigma}_n(\rho)$ of the core jellium has cylindrical symmetry, i.e. it doesn't depend on φ and z. It is a function of the radial distance ρ.

According to equations (132), (138) and (140) the **electric potential of the core nuclear jellium** is:

$$(159)\quad \Phi_n(\rho) = \frac{1}{4\pi\varepsilon_0}\int_0^\infty \overline{\sigma}_n(\rho')G(\rho,\rho')\rho' d\rho'$$

An infinitesimal charge element $\overline{\sigma}_n(\rho')\rho' d\rho' d\varphi dz$ brought into potential Φ_n has the potential energy:

$$(160)\quad d\overline{E}_n = \overline{\sigma}_n(\rho)\Phi_n(\rho)\rho d\rho d\varphi dz$$

Integrating (160) over the entire space and dividing the result by two yields the **nuclear self-repulsion energy**:

$$(161)\quad \overline{E}_n = -\overline{E}_{G,n} + \overline{E}_{n,h} + \overline{E}_{h,h} + \frac{1}{2}\int_0^{\overline{L}}\int_0^{2\pi}\int_0^\infty \overline{\sigma}_n(\rho)\Phi_n(\rho)\rho d\rho d\varphi dz$$

$$= -\overline{E}_{G,n} + \overline{E}_{n,h} + \overline{E}_{h,h} + \pi\overline{L}\int_0^\infty \overline{\sigma}_n(\rho)\Phi_n(\rho)\rho d\rho\,,$$

where $\overline{E}_{G,n}$ is the granularity correction (170), $\overline{E}_n > 0$ and $\overline{E}_{G,n} > 0$, $\overline{E}_{n,h}$ is the halo-core repulsion energy according to equation (179) and $\overline{E}_{h,h}$ is the halo self-repulsion energy according to equation (180)

The division by two in (161) takes care of the fact that the jellium is interacting with itself and the repulsion energy must not be accounted twice during integration.

Treating the nuclear charges purely as a jellium is under-representing the electron-nucleus Coulomb interaction and is over-representing the nucleus-nucleus Coulomb interaction.

Therefore and according to simplification (85), a granularity correction $\Phi_{G,e}(\overline{\sigma}_n)$ of the total Coulomb potential (132) is needed for the electron-nucleus interaction (Also a granularity correction $\overline{E}_{G,n}$ of the nuclear self-repulsion energy is needed). In the following, these two corrections will be derived.

Regarding simplification (90) the nuclei are assumed to have a mean charge of Z_m. The mean charge is determined by the average of the nuclear charges Z_i of the atomic sort weighted by the fraction $0 < F_i < 1$ of the respective atomic sort:

(162) $Z_m = \sum_0^n F_i Z_i$, where $\sum_0^n F_i = 1$ and n is the number of different atomic sorts of the mixture

The **volume occupied by exactly one nucleus with a charge of** eZ_m would be:

(163) $V_{1n} = \frac{eZ_m}{\overline{\sigma}_n} = \frac{4\pi}{3} {R_{1n}}^3$

Hence the **radius** R_{1n} **of a sphere with volume** V_{1n} would be:

(164) $R_{1n} = \sqrt[3]{\frac{3}{4\pi}\frac{eZ_m}{\overline{\sigma}_n}}$, therefore $\overline{\sigma}_n = \frac{3}{4\pi}\frac{eZ_m}{{R_{1n}}^3}$

In the picture of nuclear point charges the **potential of a single nucleus** is as following:

(165) $\Phi_{1n}(r_n) = \frac{1}{4\pi\varepsilon_0}\frac{eZ_m}{r_n}$, where r_n is the distance to the nucleus

However, in the jellium model the potential of a single nucleus equates to the **potential of a homogeneously charged sphere** with radius R_{1n}:

(166) $\Phi'_{1n}(r_n) = \frac{eZ_m}{8\pi\varepsilon_0}\left(\frac{3}{R_{1n}} - \frac{{r_n}^2}{{R_{1n}}^3}\right)$, where $r_n \le R_{1n}$ and $\overline{\sigma}_n$ is assumed to be constant within V_{1n}

Using equation (166) the self-repulsion energy per nucleus of the jellium within sphere for case $r_n \le R_{1n}$ would be as following:

(167) $\overline{E}_{1n}(\overline{\sigma}_n) = \frac{1}{2}\iiint_{V_{1n}} \Phi'_{1n}(r_n)\,dQ = \frac{1}{2}\int_{\varphi=0}^{2\pi}\int_{\theta=0}^{\pi}\int_{r=0}^{R_{1n}} \overline{\sigma}_n \Phi'_{1n}(r_n) {r_n}^2 dr_n \sin\theta\, d\theta\, d\varphi = 2\pi\overline{\sigma}_n \int_0^{R_{1n}} \Phi'_{1n}(r_n) {r_n}^2 dr_n$

$$= \frac{3}{16\pi\varepsilon_0}\frac{e^2 {Z_m}^2}{{R_{1n}}^3}\int_0^{R_{1n}}\left(\frac{3{r_n}^2}{R_{1n}} - \frac{{r_n}^4}{{R_{1n}}^3}\right)dr_n = \frac{3}{20\pi\varepsilon_0}\frac{e^2 {Z_m}^2}{R_{1n}} = \frac{1}{5\varepsilon_0}\sqrt[3]{\left(\frac{3}{4\pi}\right)^2 e^5 {Z_m}^5 \overline{\sigma}_n}$$

In reality, a single nucleus doesn't repel itself. Therefore, for each nucleus the energy $\overline{E}_{1n}(\overline{\sigma}_n)$ needs to be subtracted from the jellium's self-repulsion energy.

An infinitesimal cylindrical zone of a CP with radius $\rho - \frac{1}{2}d\rho \le \rho' \le \rho + \frac{1}{2}d\rho$ has the volume:

(168) $dV = 2\pi\overline{L}\,\rho\, d\rho$

The number of nuclei residing in volume dV is:

(169) $dN = \frac{dV}{V_{1n}} = 2\pi\overline{L}\,\frac{\overline{\sigma}_n(\rho)}{eZ_m}\rho\, d\rho$

Multiplying (169) with $\overline{E}_{1n}$ and integrating over ρ yields the **granularity correction of the jellium's core self-repulsion energy**:

$$(170)\quad \overline{E}_{G,n} = \int_{\rho=0}^{\infty} \overline{E}_{1n} dN = \frac{\overline{L}}{5\varepsilon_0} \sqrt[3]{\frac{9\pi}{2} e^2 {Z_m}^2} \int_{\rho=0}^{\infty} {\overline{\sigma}_n}^{4/3}(\rho)\rho d\rho$$

Within the volume V_{1n} there is also electron-electron interaction. No granularity correction applies to it, as this interaction is fully taken care of in (140).

Subtracting (166) from (165) and averaging over the volume V_{1n} provides the desired **granularity correction of the total potential (132) seen by the electrons** ($\overline{\sigma}_e$ is assumed to be constant within V_{1n}):

$$(171)\quad \Phi_{G,e} = \frac{4\pi}{V_{1n}} \int_0^{R_{1n}} (\Phi_{1n} - \Phi'_{1n}) {r_n}^2 dr_n = \frac{eZ_m}{\varepsilon_0 V_{1n}} \int_0^{R_{1n}} \left(r_n - \frac{3{r_n}^2}{2R_{1n}} + \frac{{r_n}^4}{2{R_{1n}}^3} \right) dr_n$$

$$= \frac{eZ_m}{10\varepsilon_0 V_{1n}} {R_{1n}}^2 = \frac{{\overline{\sigma}_n}^{1/3}}{10\varepsilon_0} \left(\frac{3eZ_m}{4\pi} \right)^{2/3}$$

According to simplification (86) the **nucleic charge distribution in the core** is modeled by means of a two-dimensional normal distribution in radial direction:

$$(172)\quad \overline{\sigma}_n(\rho) = \frac{Q}{\overline{L}} \frac{1}{2\pi\overline{s}^2} \exp\left(-\frac{\rho^2}{2\overline{s}^2} \right),$$

where $\overline{s}$ is the standard deviation in meter, Q is the nuclear charge of the CP core

The distribution function (172) is normalized, such that the integral over all space (in Cartesian coordinates) yields the nuclear charge Q:

$$(173)\quad \iiint \overline{\sigma}_n(\rho) = \int_{x=-\infty}^{\infty} \int_{y=-\infty}^{\infty} \int_{z=0}^{\overline{L}} \frac{Q}{\overline{L}} \frac{1}{2\pi\overline{s}^2} \exp\left(-\frac{\rho^2}{2\overline{s}^2} \right) dz dy dx = Q \text{, where } \rho^2 = x^2 + y^2$$

The standard deviation is to be determined iteratively (by variation), such that the total energy of the CP is minimized. During every computational iteration the electron eigenstates have to be recomputed, as they strongly depend on the nuclear charge distribution.

After studying the computational results of the radial electron density distribution, it became apparent that equation (172) needs to be adjusted like this:

$$(174)\quad \overline{\sigma}_n(\rho) = Height \cdot \exp\left(-\frac{\rho^2}{2\overline{s}^2} - \frac{\rho^5}{Slope^5} - \frac{\rho^{16}}{Cutoff^{16}} \right)$$

Parameter $Height$ has to be computed, such that the distribution function (174) is normalized to the core nuclear charge Q. Parameters $Slope$ and $Cutoff$ should be adjusted, such that the total energy of the CP is minimized.

3.10 The CP Halo (i.e. the Charge Compensation Layer)

The computational results achieved with the cylindrical model are showing that the core of a CP can carry excess negative charge (for example, 2% more electrons than nuclear charges).

Typically, the surplus negative charge of the CP has to be compensated by a surrounding layer of cations. This layer contains room charge, which terminates the electrical field around the CP core.

The charge compensation layer of cations will be called the "halo" of the CP, whereas the nuclei and the electrons comprising the CP (without the halo) will be called the "core" of the CP.

The halo can also be modeled as a jellium, like the core.

If the halo is fully compensating the charge of the core, the **linear charge density of the halo** is:

(175) $\overline{\lambda}_h \equiv \frac{Q_h}{\overline{L}} = -\overline{\lambda}_e - \overline{\lambda}_n$, where Q_h is the total charge of the halo, $\overline{\lambda}_n = Q/\overline{L}$ is the linear charge density of the nuclei in the core and $\overline{\lambda}_e$ is the linear charge density of the electrons in the core

For the purpose of computing the electric potential in the core, the easiest way is to assume a homogeneously charged cylindrical shell with a radius ρ_h, which is larger than the radial extent of the electron orbits and the extent of the nuclear charge distribution of the core (simplification (87)). The shell shall be concentric to the z-axis and have an infinitesimal wall thickness of $\delta\rho$. The **charge density of the halo** cations then is:

(176) $$\overline{\sigma}_h = \frac{\overline{\lambda}_h}{2\pi\rho_h\delta\rho}$$

The potential summands sourced by the nuclei and the electrons had been specified in equation (132). The **contribution of the halo to the Coulomb potential** computes as:

(177) $$\Phi_h = \frac{1}{4\pi\varepsilon_0}\int_0^\infty \overline{\sigma}_h(\rho')G(\rho,\rho')\rho' d\rho' = \frac{\overline{\lambda}_h}{8\pi^2\varepsilon_0}\int_{\rho_h}^{\rho_h+\delta\rho}\frac{1}{\rho'\delta\rho}G(\rho,\rho')\rho' d\rho' = \frac{\overline{\lambda}_h}{8\pi^2\varepsilon_0}G(\rho_h,\rho_h)$$

The **contribution of the halo to the Coulomb energy of a single electron** is:

(178) $$\overline{E}_{C,h} \equiv -e\Phi_h = -\frac{e\overline{\lambda}_h}{8\pi^2\varepsilon_0}G(\rho_h,\rho_h)$$

The additional charge of the halo increases the self-repulsion energy between the nuclear charges, as mentioned in equation (161). In particular:

The **core-halo repulsion energy** can be computed via:

(179) $$\overline{E}_{n,h} = Q\Phi_h$$

The **halo self-repulsion energy** is:

(180) $$\overline{E}_{h,h} = \frac{1}{2}Q_h\Phi_h$$

The result in the above equation was divided by two, because the halo charges are interacting with themselves.

The halo is the part of the CP, which interchanges matter with the environment. It would therefore be interesting to model the properties (density distribution, electric field, pressure, etc.). Unfortunately, this is not trivial: The internal pressure of the halo is partially caused by electrostatic repulsion of the cations. It is also caused by the degeneracy pressure of the cation's core electron shells. The degeneracy pressure depends on how many electrons remain to be bound to the cations.

Depending on the electrical field strength, part of the cation's electron shells is ripped away. One can therefore expect that the cations close to the CP core are carrying multiple positive charges, whereas the cations at the outer boundary of the halo are carrying only one positive charge. It was beyond the capacity of the author to model this reliably.

When a CP attaches itself to the surface of a dielectric (or metallic) substrate, some of the cationic charges are replaced by polarization charges induced in the substrate by the electric field of the CP. Per unit of charge it takes less energy to create polarization charge than it takes to create cationic charge. Therefore, a CP can lower its total energy by attaching to a surface and thereby neutralizing some of the halo cations.

3.11 A Plausibility Check on Pressures

Dividing equation (117) by the electron charge provides the **electron density** $d_e = -\overline{\sigma}_e / e = \sum_{i=1}^{N} |\Psi_i|^2$. By idealizing the electrons as a **free electron gas**, the electron density can be used for computing the **electron degeneracy pressure** (at the non-relativistic limit):

(181) $$P_d = \frac{\left(3\pi^2\right)^{2/3} \hbar^2}{5m_e} d_e^{\,5/3}$$

The degeneracy (outward) pressure is approximately balancing the (inward) pressure generated by the electrostatic and magnetic forces acting on the electrons:

(182) $P_d \approx P_e + P_m$, where P_e is the electrostatic pressure, P_m is the magnetic pressure

The above equation is useful as a **plausibility check** for any solutions produced by the Klein-Gordon equation.

The electric field $\varepsilon_\rho(\rho')$ from equation (144) creates a force $F_{\rho,e}(\rho')$ on the infinitesimal charge element $\left[\overline{\sigma}_n(\rho') + \overline{\sigma}_e(\rho')\right]\rho' d\rho' d\varphi dz$ of the plasma:

(183) $$F_{\rho,e}(\rho') = \varepsilon_\rho(\rho')\left[\overline{\sigma}_n(\rho') + \overline{\sigma}_e(\rho')\right]\rho' d\rho' d\varphi dz$$

Integrating (183) provides the **pressure** on the plasma **created by the electric field**:

(184) $$P_e(\rho) = P_G + \int_\rho^\infty \frac{F_{\rho,e}(\rho')}{\rho' d\varphi dz} = P_G + \int_\rho^\infty \varepsilon_\rho(\rho')\left[\overline{\sigma}_n(\rho') + \overline{\sigma}_e(\rho')\right] d\rho'$$, where P_G is the granularity correction of the electrostatic pressure specified in (191)

The magnetic field $B_\varphi(\rho')$ from equation (145) creates an inward force $F_{\rho,m}(\rho')$ on the infinitesimal current element $J_z(\rho')\rho' d\rho' d\varphi$ of the electron gas:

(185) $$F_{\rho,m}(\rho') = \overline{L} B_\varphi(\rho') J_z(\rho') \rho' d\rho' d\varphi$$

Integrating (185) provides the **inward pressure** on the moving electron gas **created by the magnetic field**:

(186) $$P_m(\rho) = -\int_\rho^\infty \frac{F_{\rho,m}(\rho')}{\overline{L}\rho' d\varphi} = -\int_\rho^\infty B_\varphi(\rho') J_z(\rho') d\rho'$$

The granularity correction P_G stems from electrostatic attraction of the electron gas to the nuclear point charges in the direct vicinity $r \le R_{1n}$ of the nuclei. It can be computed as following:

(187) $$P_G(\rho) = \frac{\partial}{\partial V_{1n}}\left(\overline{E}_{en} + \overline{E}_{ee}\right)$$, where $\overline{E}_{en}$ is the electron-nucleus Coulomb energy and $\overline{E}_{ee}$ is the electron-electron Coulomb energy, respectively within a volume V_{1n} of the plasma

Using equation (165) and assuming the electron charge density is constant within V_{1n}, the electron-nucleus Coulomb energy computes as:

(188) $$\overline{E}_{en} = 4\pi\overline{\sigma}_e \int_0^{R_{1n}} \Phi_{1n} r_n^{\,2} dr_n = \frac{eZ_m\overline{\sigma}_e}{\varepsilon_0}\int_0^{R_{1n}} r_n dr_n = \frac{eZ_m\overline{\sigma}_e}{2\varepsilon_0} R_{1n}^{\,2} = \left(\frac{3}{4\pi}\right)^{2/3} \frac{e^2 Z_m^{\,2}}{2\varepsilon_0} \frac{\overline{\sigma}_e}{\overline{\sigma}_n} V_{1n}^{\,-1/3}$$

Taking the idea from (166), the potential of the electrons within volume V_{1n} is:

(189) $$\Phi_{ee}(r_n) = \frac{\overline{\sigma}_e V_{1n}}{8\pi\varepsilon_0}\left(\frac{3}{R_{1n}} - \frac{{r_n}^2}{{R_{1n}}^3}\right)$$

Using this potential, the electron-electron Coulomb energy within volume V_{1n} is:

(190) $$\overline{E}_{ee} = 2\pi\overline{\sigma}_e\int_0^{R_{1n}}\Phi_{ee}{r_n}^2 dr_n = \frac{{\overline{\sigma}_e}^2 V_{1n}}{4\varepsilon_0}\int_0^{R_{1n}}\left(\frac{3{r_n}^2}{R_{1n}} - \frac{{r_n}^4}{{R_{1n}}^3}\right)dr_n = \frac{{\overline{\sigma}_e}^2 V_{1n}}{5\varepsilon_0}{R_{1n}}^2 = \left(\frac{3}{4\pi}\right)^{2/3}\frac{e^2{Z_m}^2}{5\varepsilon_0}\frac{{\overline{\sigma}_e}^2}{{\overline{\sigma}_n}^2}{V_{1n}}^{-1/3}$$

Assuming that $\overline{\sigma}_e/\overline{\sigma}_n$ is constant at volume changes and putting together (163), (187), (188) and (190) yields:

(191) $$P_G(\rho) = \left(\frac{3}{4\pi}\right)^{2/3}\frac{e^2{Z_m}^2}{\varepsilon_0}\left(\frac{1}{2}\frac{\overline{\sigma}_e}{\overline{\sigma}_n} + \frac{1}{5}\frac{{\overline{\sigma}_e}^2}{{\overline{\sigma}_n}^2}\right)\frac{\partial}{\partial V_{1n}}{V_{1n}}^{-1/3} = -\left(\frac{3eZ_m}{4\pi}\right)^{2/3}\frac{{\overline{\sigma}_n}^{4/3}}{3\varepsilon_0}\left(\frac{1}{2}\frac{\overline{\sigma}_e}{\overline{\sigma}_n} + \frac{1}{5}\frac{{\overline{\sigma}_e}^2}{{\overline{\sigma}_n}^2}\right)$$

One has to keep in mind, though that equation (182) is merely a coarse approximation:

- Polarization of the electron gas by the field of the nuclei has been neglected.
- At high densities, equation (181) overestimates the degeneracy pressure P_d, because a fraction of the electrons have a relativistic velocity. At the relativistic limit P_d is proportional to ${d_e}^{4/3}$, rather than ${d_e}^{5/3}$ suggested by equation (181).

3.12 Transformation to Natural Units

In the following text the **Hartree energy** will be used as a **unit of measure for energy**. It is defined as:

(192) $$\overline{E}_h \equiv \frac{\hbar^2}{m_e{a_0}^2} = \frac{e^2}{4\pi\varepsilon_0 a_0} = m_e\left(\frac{e^2}{4\pi\varepsilon_0\hbar}\right)^2 = m_e c^2\alpha^2 \approx 27.211eV$$, where

(193) $$a_0 \equiv \frac{4\pi\varepsilon_0\hbar^2}{m_e e^2} = \frac{\hbar}{m_e c\alpha} \approx 52.918\,pm$$ is the **Bohr radius** and

(194) $$\alpha \equiv \frac{1}{4\pi\varepsilon_0}\frac{e^2}{\hbar c} = \frac{\hbar}{m_e c a_0} \approx 7.2974\cdot 10^{-3}$$ is the **fine structure constant**.

The **electron rest energy** in units of $\overline{E}_h$ therefore becomes:

(195) $$\frac{m_e c^2}{\overline{E}_h} = \frac{1}{\alpha^2}$$

The following equation defines a **reference radius**:

(196) $$\rho_0 \equiv \frac{a_0}{\sqrt{\lambda_n}}$$, where

(197) $$\lambda_n \equiv \frac{Q}{e}\frac{1}{L}$$ is the **linear nuclear charge density of the core** in natural units,

(198) $$L \equiv \frac{\overline{L}}{a_0}$$ is the **CP length** in units of the Bohr radius.

The definition of the reference radius was crafted, such that the relative radial extent of the electron orbits at the non-relativistic limit becomes independent of the linear nuclear charge density.

The **relative radius** is defined as:

(199) $r \equiv \frac{\rho}{\rho_0}$

The **volume charge density** in natural units is defined here as:

(200) $\sigma = \sigma_n + \sigma_e + \sigma_h \equiv \frac{{a_0}^3}{e}\overline{\sigma} = \frac{{a_0}^3}{e}\left(\overline{\sigma}_n + \overline{\sigma}_e + \overline{\sigma}_h\right)$

The **current density** in natural units is defined here as:

(201) $J_z \equiv \frac{{a_0}^3}{ec}\overline{J}_z$

Additionally, the following quantities are defined here:

(202) $E \equiv \overline{E}/\overline{E}_h$, i.e. the **sum of the potential energy and the kinetic energy** of the electron, which is functioning as the **energy eigenvalue** of the Klein-Gordon equation

(203) $E_C = E_{C,n} + E_{C,e} + E_{G,e} + E_{C,h} \equiv -e\Phi/\overline{E}_h$
$= -e\Phi_n/\overline{E}_h - e\Phi_e/\overline{E}_h - e\Phi_G/\overline{E}_h - e\Phi_h/\overline{E}_h$,
i.e. the **potential energy related to the Coulomb potential** of the electrons, the core nuclei and the halo as seen by an electron (negative sample charge)

(204) $E_{n,h} \equiv \overline{E}_{n,h}/\overline{E}_h = -\lambda_n L E_{C,h}$, i.e. the **core-halo repulsion energy in natural units**

(205) $E_{h,h} \equiv \overline{E}_{h,h}/\overline{E}_h = -\frac{1}{2}\lambda_h L E_{C,h}$, i.e. the **halo self-repulsion energy in natural units**

(206) $P_z \equiv a_0\overline{P}_z/\hbar = 2\pi l/L$ is **the axial canonical momentum** of the electron in natural units

(207) $A_z \equiv -ea_0\overline{A}_z/\hbar$ is the **axial magnetic vector potential** in natural units. The related terms $-P_z A_z$ and ${A_z}^2/2$ are the **magnetic electron-electron interaction energy** and the so-called **diamagnetic energy**, respectively

(208) $p_z \equiv a_0\overline{p}_z/\hbar = P_z - A_z = 2\pi l/L + ea_0\overline{A}_z/\hbar$ is the **axial kinetic momentum** of the electron in natural units. The related term ${p_z}^2/2$ is **the axial kinetic energy** in natural units

(209) $E_n \equiv \overline{E}_n/\overline{E}_h$, i.e. the **nuclear self repulsion energy**

(210) $E_{G,n} \equiv \overline{E}_{G,n}/\overline{E}_h$, i.e. the **granularity correction** of the nuclear jellium's self-repulsion

The **radial wave function** in natural units is defined as:

(211) $R \equiv \rho_0\Psi_\rho$

Dividing both sides of (155) by $\overline{E}_h$, using the product rule of calculus and substituting via (195), (198), (202), (203), (204) and (208) results in:

(212) $\left\{-\frac{{a_0}^2}{2}\frac{d^2}{d\rho^2} - \frac{{a_0}^2}{2\rho}\frac{d}{d\rho} + \frac{{a_0}^2}{2}\frac{m^2}{\rho^2} + \frac{{p_z}^2}{2} - \frac{\alpha^2}{2}\left(E - E_C + \frac{1}{\alpha^2}\right)^2 + \frac{1}{2\alpha^2}\right\}\Psi_\rho = 0$

Substituting (199) and (211) in (212), using the notation R' and R'' for the first and second derivative to r of radial wave function R and multiplying both sides of the equation by ρ_0 yields the **radial Klein-Gordon equation** in natural units:

$$(213)\quad -\frac{\lambda_n}{2}R'' - \frac{\lambda_n}{2r}R' + \left[\frac{\lambda_n m^2}{2r^2} + \frac{{p_z}^2}{2} - \frac{\alpha^2}{2}\left(E - E_C + \frac{1}{\alpha^2}\right)^2 + \frac{1}{2\alpha^2}\right]R = 0$$

The **Schrödinger equation** (157) in natural units is:

$$(214)\quad -\frac{\lambda_n}{2}R'' - \frac{\lambda_n}{2r}R' + \left[\frac{\lambda_n m^2}{2r^2} + \frac{{p_z}^2}{2} + E_C - E\right]R = 0$$

The **geometry integral** (142) can be expressed in natural units as:

$$(215)\quad G(r,r') = \begin{cases} 4\pi\left[\ln\left(\sqrt{\lambda_n}L/2 + \sqrt{\lambda_n L^2/4 + r'^2}\right) - \ln r'\right] & \text{for } r \le r' \\ 4\pi\left[\ln\left(\sqrt{\lambda_n}L/2 + \sqrt{\lambda_n L^2/4 + r^2}\right) - \ln r\right] & \text{for } r > r' \end{cases}$$

Multiplying (117) with ${a_0}^3/e$ and using (148) and (211) yields the **volume charge density in natural units**:

$$(216)\quad \sigma_e(r) = -\frac{\lambda_n}{2\pi L}\sum_{i=1}^{N}\left|R_i(r)\right|^2$$

Multiplying (120) with ${a_0}^3/(ec)$ and using (153), (194), (198), (204) and (211) yields the **current density in natural units**:

$$(217)\quad J_z(r) = \frac{-\alpha\lambda_n}{2\pi L}\sum_{i=1}^{N}\left[P_{z,i} - A_z(r)\right]\left|R_i(r)\right|^2$$

By using (194), (199), (204), (207), and (211) in equation (122) the **total current** (averaged over all electrons, in amperes) can be computed from the quantities in natural units as following:

$$(218)\quad I_z = -\frac{e\alpha c}{a_0 L}\sum_{i=1}^{N}\int_0^\infty\left[P_{z,i} - A_z(r)\right]\left|R_i(r)\right|^2 r\,dr$$

Multiplying both sides of (140) by $-e/\overline{E}_h$ and substituting via (199), (200), (203) and (216) provides the **Coulomb energy** in natural units:

$$(219)\quad E_C(r) = E_{G,e} - \frac{1}{\lambda_n}\int_0^\infty\sigma(r')G(r,r')r'dr' = E_{G,e} + E_{C,h} - \frac{1}{\lambda_n}\int_0^\infty\left[\sigma_e(r') + \sigma_n(r')\right]G(r,r')r'dr'$$

The **contribution of the halo to the Coulomb energy of a single electron in natural units** is:

$$(220)\quad E_{C,h} = -\frac{\lambda_h}{2\pi}G(r_h,r_h),\ \text{where}\ \lambda_h = \frac{a_0\overline{\lambda}_h}{e}\ \text{and}\ r_h = \frac{\rho_h}{\rho_0}$$

Dividing both sides of equation (171) by $-e/\overline{E}_h$ and substituting via (192), (193) and (200) yields the **granularity correction of the electron-nucleus interaction energy** is**:**

$$(221)\quad E_{G,e} = -\frac{2\pi}{5}{\sigma_n}^{1/3}\left(\frac{3Z_m}{4\pi}\right)^{2/3}$$

Multiplying both sides of (143) by $-ea_0/\hbar$, substituting via (194), (196), (199), (201), (207) and (217) and using $\varepsilon_0\mu_0 = c^{-2}$ provides the **magnetic vector potential** in natural units:

(222) $A_z(r) = -\frac{\alpha}{\lambda_n}\int_0^\infty J_z(r')G(r,r')r'dr' = \frac{\alpha^2}{2\pi L}\int_0^\infty \left\{\sum_{i=1}^{N}\left[P_{z,i} - A_z(r')\right]|R_i(r')|^2\right\}G(r,r')r'dr'$

By dividing (124) by ρ_0 and using (196), (199) and (211) the **expectation value of the electron orbit radius** in natural units becomes:

(223) $\langle r\rangle = \int_0^\infty |R|^2 r^2 dr$

Dividing (161) by $\overline{E}_h$ and using (170), (192), (193), (196), (200), (203) and (210) and taking care of the fact that the sample charges are positive, yields the **nuclear self-repulsion energy** in natural units:

(224) $E_n = -E_{G,n} + E_{n,h} + E_{h,h} - \frac{\pi L}{\lambda_n}\int_0^\infty \sigma_n(r)E_{C,n}(r)rdr$, where $E_n > 0$ and

$E_{G,n} = \frac{4\pi}{5}\sqrt[3]{\frac{9\pi}{2}Z_m{}^2}\,\frac{L}{\lambda_n}\int_{\rho=0}^\infty \sigma_n{}^{4/3}(r)rdr$ is the **granularity error** in natural units, $E_{G,n} > 0$

Using (196) and (211) the **normalization criteria** (149) in natural units becomes:

(225) $1 = \|R\| = \int_0^\infty |R(r)|^2 rdr$

The **standard deviation of the core nuclear charge distribution** in natural units is:

(226) $s \equiv \frac{\overline{s}}{\rho_0}$

Multiplying both sides of (172) with $a_0{}^3/e$ and substituting via (196), (198), (199) and (226) yields the **nuclear charge distribution of the core** in natural units:

(227) $\sigma_n(r) = \frac{Q\lambda_n}{2\pi e L s^2}\exp\left(-\frac{r^2}{2s^2}\right)$

With the modifications made in (174) the nuclear charge distribution reads:

(228) $\sigma_n(r) = C_H \exp\left(-\frac{r^2}{2s^2} - \frac{r^5}{C_S{}^5} - \frac{r^{16}}{C_C{}^{16}}\right)$, where $C_H = \frac{a_0{}^3}{e}Height$, $C_S = \frac{Slope}{\rho_0}$ and $C_C = \frac{Cutoff}{\rho_0}$

The **charge density of the halo** (derived from equation (176)) in natural units reads:

(229) $\sigma_h = \frac{\lambda_n\lambda_h}{2\pi r_h \delta r}$

3.13 Approximate Solution of the Radial Wave Function

The following **ansatz** will be used for approximating the **radial wave function**:

(230) $R(r) = f(r)\cdot\exp(-\zeta r)$, where

$f(r)$ is assumed to be a polynomial and $\zeta \in \mathbf{R}^+$ is a tunable scaling factor.

The radial Klein-Gordon equation (213) has a second solution, which is linear independent of the solution gained by ansatz (230). The second solution would be represented by the following ansatz:

(231) $R(r) = f(r) \cdot \exp(\zeta r)$, where $\zeta \in \mathbf{R}^+$

However, this second solution and all linear combinations with it were incompatible with boundary condition (110). Therefore, this second solution ansatz will not be used.

The first derivative of the radial wave functions (230) reads:

(232) $R' = (f' - \zeta f) \cdot \exp(-\zeta r)$

The second derivative of the radial wave functions is:

(233) $R'' = (f'' - 2\zeta f' + \zeta^2 f) \cdot \exp(-\zeta r)$

The value of ζ can be determined by analyzing the asymptotic behavior of the wave function R at $r \to \infty$:

The electromagnetic potential (and therefore the terms E_C and A_z) become zero, when the radius approaches infinity. Also, the terms proportional to $1/r$ and $1/r^2$ disappear at $r \to \infty$. The Klein-Gordon equation (213) then simplifies to:

(234) $-\lambda_n R'' + (P_z^2 - \alpha^2 E^2 - 2E)R = 0$

Inserting (231) and (233) into (234) leads to:

(235) $\lambda_n(-f'' + 2\zeta f' - \zeta^2 f) + (P_z^2 - \alpha^2 E^2 - 2E)f = 0$

Assuming function f can be approximated by a polynomial of finite degree, the function dominates over its derivatives at $r \to \infty$ and therefore the **exponential scaling factor** is:

(236) $\zeta = \sqrt{\frac{1}{\lambda_n}(P_z^2 - \alpha^2 E^2 - 2E)}$

Only the positive value of the square root is valid here, because of ansatz (230).

As a consequence of equation (236), there is an upper limit of the eigenvalues E:

(237) $E < \frac{1}{\alpha^2}\left(\sqrt{\alpha^2 P_z^2 + 1} - 1\right)$

Solving (236) for the energy provides:

(238) $E = \frac{1}{\alpha}\sqrt{P_z^2 - \lambda_n \zeta^2 + \frac{1}{\alpha^2}} - \frac{1}{\alpha^2}$

Only the positive value of the square root is valid here, because of boundary condition (109).

Equation (238) in conjunction with boundary condition (109) has interesting consequences:

(239) $0 < \zeta < \sqrt{\frac{1}{\lambda_n}\left(P_z^2 + \frac{1}{\alpha^2}\right)}$, i.e. the scaling factor ζ is limited by means of the rest energy

At the **non-relativistic limit** the **exponential scaling factor** computes as:

(240) $\zeta = \sqrt{\frac{1}{\lambda_n}(P_z^2 - 2E)}$, thus $E = \frac{1}{2}(P_z^2 - \lambda_n \zeta^2)$, where $0 < \zeta < \sqrt{\frac{1}{\lambda_n}\left(P_z^2 + \frac{2}{\alpha^2}\right)}$ and $E < \frac{P_z^2}{2}$

Inserting (230), (232), (233) and (238) into radial Klein-Gordon equation (213) is leading to:

$$(241)\quad -\frac{\lambda_n}{2}f'' + \frac{\lambda_n}{2}\left(2\zeta - \frac{1}{r}\right)f' + \left[\frac{\lambda_n\zeta}{2r} + \frac{\lambda_n m^2}{2r^2} + \frac{{p_z}^2}{2} - \frac{\alpha^2}{2}\left(\frac{1}{\alpha}\sqrt{{P_z}^2 - \lambda_n\zeta^2 + \frac{1}{\alpha^2}} - E_C\right)^2 + \frac{1}{2\alpha^2} - \frac{\lambda_n\zeta^2}{2}\right]f = 0$$

For the non-relativistic limit the Schrödinger equation (214) is leading to:

$$(242)\quad -\frac{\lambda_n}{2}f'' + \frac{\lambda_n}{2}\left(2\zeta - \frac{1}{r}\right)f' + \left(\frac{\lambda_n\zeta}{2r} + \frac{\lambda_n m^2}{2r^2} - P_z A_z + \frac{{A_z}^2}{2} + E_C\right)f = 0$$

Solutions to differential equation (241) or (242) consist of eigenvalues of ζ and eigenstates of polynomial f. These solutions can then be used to compute the eigenvalues of E and eigenstates of R of the radial Klein-Gordon equation (213) or Schrödinger equation (214).

Function $f(r)$ can be **approximated by a polynomial** of r as following:

$$(243)\quad f(r) \approx \sum_{j=0}^{J} c_j r^{\beta+j} \text{ for } \beta \in \mathbf{N}_0 \text{ and } c_j \in \mathbf{R}$$

The summation is running over a number $J+1$ of terms. The maximum index J is depending on the desired accuracy of the approximation. In practice, J needs to be 150 through 2500 with 80-bit floating point numbers for "reasonable" accuracy. The required J increases drastically with increasing axial current in the CP.

The (generally arbitrary) phase of the (generally complex) wave function R is chosen, such that the coefficients c_j become real numbers.

Generally, constants c_j and ζ are depending on quantum numbers n, m and l. For simplicity reasons, this dependency is not reflected in the respective indices of these constants.

The first derivative of (243) reads:

$$(244)\quad f'(r) \approx \sum_{j=0}^{J} (\beta + j) c_j r^{\beta+j-1}$$

The second derivative of (243) is:

$$(245)\quad f''(r) \approx \sum_{j=0}^{J} (\beta + j)(\beta + j - 1) c_j r^{\beta+j-2}$$

In equation (241) a number of terms can be approximated by a polynomial of degree P:

$$(246)\quad \frac{{p_z}^2}{2} - \frac{\alpha^2}{2}\left(\frac{1}{\alpha}\sqrt{{P_z}^2 - \lambda_n\zeta^2 + \frac{1}{\alpha^2}} - E_C\right)^2 + \frac{1}{2\alpha^2} - \frac{\lambda_n\zeta^2}{2} \approx \sum_{p=0}^{P} b_p r^p ,$$

where $P \le J - 1$ and $b_p \in \mathbf{R}$

At the non-relativistic limit (246) simplifies to:

$$(247)\quad -P_z A_z + \frac{{A_z}^2}{2} + E_C \approx \sum_{p=0}^{P} b_p r^p \text{ , where } P \le J - 1 \text{ and } b_p \in \mathbf{R}$$

Approximations (246) and (247) have a limited convergence radius, no matter how large P is made and how the coefficients are chosen. However, for a given closed interval of radius values the approximations can be made

arbitrarily precise by choosing P and the coefficients appropriately. Good approximation accuracy has been achieved with $P = 8$.

A suitable approximation can be found by first determining the range $r_0 \le r \le r_P$ of relevant radius values reflecting the radial extent of the electron's wave function. For example, one can choose r_0 and r_P in such a way that the electron resides with 99.9% probability between these radii and, at the same time, the range is made as small as possible.

Based on this range, additional nodes r_1 through r_{P-1} need to be determined between r_0 and r_P. The nodes should be chosen, such that the approximation error is minimized (e.g. via Chebyshev nodes). These nodes can then be used e.g. by Newton polynomials for interpolation.

Inserting (243), (244), (245) and (246) into (241) and multiplying both sides with $-2r^2/\lambda_n$ yields:

$$(248)\quad \sum_{j=0}^{J}(\beta+j)(\beta+j-1)c_j r^{\beta+j} + (1-2\zeta r)\sum_{j=0}^{J}(\beta+j)c_j r^{\beta+j} - \left[\zeta r + m^2 + \frac{2}{\lambda_n}\sum_{p=0}^{P} b_p r^{p+2}\right]\sum_{j=0}^{J} c_j r^{\beta+j} = 0$$

By neglecting the terms with potencies of r higher than $\beta + J$ the result can be written as:

$$(249)\quad \sum_{j=0}^{J}\left\{\left[(\beta+j)^2 - m^2\right]c_j + \zeta(1-2\beta-2j)c_{j-1} - \frac{2}{\lambda_n}\sum_{p=0}^{P} b_p c_{j-p-2}\right\} r^{\beta+j} + \varepsilon_{cut} = 0,$$

where $c_i = 0$ for $i < 0$

and ε_{cut} is the cut-off error produced by neglecting potencies of r higher than $\beta + J$

The cut-off error computes as:

$$(250)\quad \varepsilon_{cut} = \zeta(-1-2\beta-2J)c_J r^{\beta+J+1} - \frac{2}{\lambda_n}\sum_{p=0}^{P}\sum_{j=J+1}^{J+p+2} b_p c_{j-p-2} r^{\beta+j}$$

The left hand side of equation (249) equals zero for all values of r. This can only be true, if the coefficients of $r^{\beta+j}$ fulfill the following equation:

$$(251)\quad \left[(\beta+j)^2 - m^2\right]c_j + \zeta(1-2\beta-2j)c_{j-1} - \frac{2}{\lambda_n}\sum_{p=0}^{P} b_p c_{j-p-2} = 0$$

Analyzing the case $j = 0$ gives:

$$(252)\quad \beta^2 - m^2 = 0, \text{ therefore } \beta = |m|$$

Inserting (252) into (251) yields the **iterative formula for computing the coefficients** from the value of c_0:

$$(253)\quad c_j = \frac{1}{(2|m|j + j^2)}\left\{\zeta(2|m| + 2j - 1)c_{j-1} + \frac{2}{\lambda_n}\sum_{p=0}^{P} b_p c_{j-p-2}\right\}, \text{ where } c_i = 0 \text{ for } i < 0$$

Note that the coefficients c_j are all proportional to each other. Formula (253) stays the same at the non-relativistic limit.

Equation (250) puts additional requirements on the coefficients c_{J-P} through c_J, which contradict the requirements of equation (253). Therefore, the polynomial approximation of the radial wave function cannot be made precise. Unfortunately, ε_{cut} diverges, if J is made too large. The latter effect is caused by rounding errors in conjunction with finite floating-point number precision.

The approximation error becomes minimal, when the last coefficient c_J is zero, which is the case only for the eigenvalues of ξ. Therefore, this defines a method for determining the eigenvalues.

Alternatively one could determine the eigenvalues by using the original Klein-Gordon equation (213) in conjunction with (238) as a measure of error:

$$(254)\quad \delta(r,\zeta) = -\frac{\lambda_n}{2}R'' - \frac{\lambda_n}{2r}R' + \left[\frac{\lambda_n m^2}{2r^2} + \frac{{p_z}^2}{2} - \frac{\alpha^2}{2}\left(\frac{1}{\alpha}\sqrt{{P_z}^2 - \lambda_n\zeta^2 + \frac{1}{\alpha^2}} - E_C\right)^2 + \frac{1}{2\alpha^2}\right]R$$
$$\approx -\frac{\lambda_n}{2}R'' - \frac{\lambda_n}{2r}R' + \left\{\frac{\lambda_n m^2}{2r^2} + \sum_{p=0}^{P} b_p r^p + \frac{\lambda_n\zeta^2}{2}\right\}R$$

At the non-relativistic limit one would use the Schrödinger equation (214) in conjunction with (240) as a measure of error:

$$(255)\quad \delta(r,\zeta) = -\frac{\lambda_n}{2}R'' - \frac{\lambda_n}{2r}R' + \left[\frac{\lambda_n m^2}{2r^2} - P_z A_z + \frac{{A_z}^2}{2} + E_C + \frac{\lambda_n\zeta^2}{2}\right]R$$
$$\approx -\frac{\lambda_n}{2}R'' - \frac{\lambda_n}{2r}R' + \left\{\frac{\lambda_n m^2}{2r^2} + \sum_{p=0}^{P} b_p r^p + \frac{\lambda_n\zeta^2}{2}\right\}R$$

The function $\delta(r,\zeta)$ is approaching zero for all values of r only at the energy eigenvalues E or ζ.

The value of coefficient c_0 can be determined from ζ by normalization of the wave function R.

Combining (230), (243) and (252) leads to:

$$(256)\quad R \approx \sum_{j=0}^{J} c_j r^{|m|+j} \exp(-\zeta r)$$

The normalization condition (225) requires:

$$(257)\quad 1 = \|R\| = \int_0^\infty |R(r)|^2 r dr = \int_0^\infty \left(\sum_{j=0}^{J} c_j r^{|m|+j}\right)^2 \exp(-2\zeta r) r dr$$

That means, one has to scale all c_j proportionally, such that (257) yields the value 1.

In many cases the cut-off error (250) is so small that the radial wave function can be computed without having any noticeable distortion from it. Unfortunately, the cut-off error is not always small compared to the amplitude of the "real" wave function. The following plot shall illustrate this:

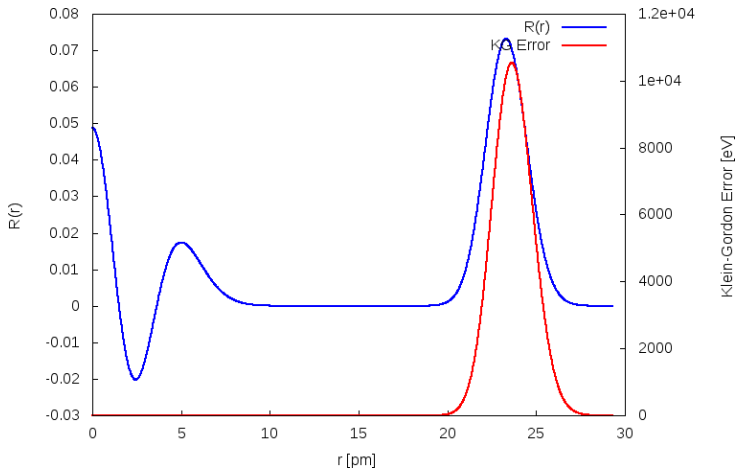

Figure 51 Example of a radial wave function (blue) with a large distortion from the cut-off error centered on $r \approx 23\,pm$. The distortion is leading to a large Klein-Gordon error (red).

Empirically, the Klein-Gordon error in Figure 51 as computed via (254) is closely correlated to the cut-off error computed via $\varepsilon_{cut} \cdot \exp(-\zeta r)$ for the same wave function:

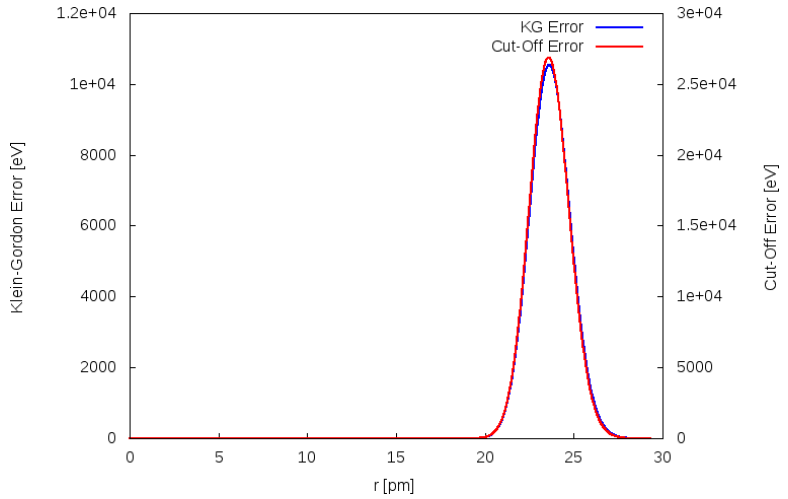

Figure 52 Correlation between the Klein-Gordon error (blue) and the cut-off error (red)

This correlation is a bit surprising, as the Klein-Gordon error is computed from different potencies of the radius than the cut-off error.

Distortions of the wave function and the related Klein-Gordon error are generally becoming smaller, if the upper limits of the summation index in (243) and (244) are adjusted, such that the highest potencies of the radius matches with (245):

$$(258) \quad f = \sum_{j=0}^{J-2} c_j r^{|m|+j} \quad \text{re-definition of (243)}$$

$$(259) \quad f' = \sum_{j=0}^{J-1} (|m|+j) c_j r^{|m|+j-1} \quad \text{re-definition of (244)}$$

$$(260) \quad f'' = \sum_{j=0}^{J} (|m|+j)(|m|+j-1) c_j r^{|m|+j-2} \quad \text{copy of (245)}$$

The adjusted upper limits of j are changing the cut-off error (250) to:

$$(261) \quad \varepsilon_{cut} = \left[(|m|+J-1)^2 c_{J-1} + \zeta(3-2|m|-2J) c_{J-2} \right] r^{|m|+J-1} + (|m|+J-1)\left[(|m|+J) c_J - 2\zeta c_{J-1} \right] r^{|m|+J} - \frac{2}{\lambda_n} \sum_{p=0}^{P} \sum_{j=J-1}^{J+p} b_p c_{j-p-2} r^{|m|+j} \quad \text{(Re-definition)}$$

3.14 Grouping, Orbital Occupation, Self-Consistent Field Iterations

The electron configuration of a CP consists of many orbitals, which are characterized by the quantum numbers n, m and l. According to the Pauli Exclusion Principle each orbital can only be occupied by a maximum of two electrons (one with spin up and one with spin down).

There are too many electrons in a CP for computing all occupied orbitals individually. Instead, ranges of orbitals with contiguous values for l are grouped together. Within a group all orbitals have the same quantum numbers n and m. These orbitals of such groups differ in quantum number l. The arithmetic mean of the quantum numbers l represents the group during computation.

The simplest approach is to let each group contain the same number of orbitals. On one hand, the groups should be small enough to achieve a fine spacing in the electron energies (for accuracy). On the other hand, the groups need to be coarse enough, such that computation time becomes affordable.

Equations (216) and (217) are computed by letting the summation run over the occupied number of groups. Each summand is multiplied by the number of electrons it represents.

For ground state computations the occupation should start with the lowest energy. It should progress to groups with successively higher energy until the targeted number of electrons "found their orbital".

Equations (216), (217) and (253), as well as the occupation process are depending on each other in a circular manner. Thus they can be computed only **iteratively** until reaching **self-consistency between eigenstates, potential and occupation**.

Within each of these SCF-iterations (self-consistent field iterations) there is a need for sub-iterations:

According to (217) and (222) the axial current density J_z and the vector potential A_z are mutually depending on each other. Sub-iterations are required for making these quantities consistent with each other, while leaving the eigenstates unchanged.

4 Extensions of the Cylindrical Model

The cylindrical model, as defined by simplifications (80) through (98), was build to be simple, rather than precise. Accordingly, some terms are missing in the Hamiltonian.

The following extensions of the cylindrical model are attempting to explore some of these missing terms, which had been "approximated away" in the first instance. The extensions themselves are also approximations.

4.1 Helical Structure, Spin-Orbit Interaction, Inductance

According to simplification (91) the electron spins (and their related magnetic moment) are neglected. According to simplification (92) also the magnetic field of the azimuthal electron orbits is neglected. Both simplifications make sense in the perfectly straight geometry of CPs prescribed by the cylindrical model of CPs.

In reality however, CPs often have a helical shape, as is depicted by Figure 2. This is like a solenoid with two layers of windings. In these cases the axial movement of the electrons is tied to their azimuthal movement. The magnetic field then has an axial component, which will couple with the electron spins. The details of the coupling are complicated and not yet fully understood.

Here, a rough estimate shall be derived about the maximum energy release per electron, which can be expected when the electron spins are aligning with the axial component of the magnetic field.

The strength of the magnetic field within a long solenoid in vacuum is given by:

(262) $B = \mu_0 \frac{N}{l} I$, where $\frac{N}{l}$ is the number of winding turns per unit of length, I is the current flowing through the windings and μ_0 is the vacuum permeability

Assuming that the current reaches 10 kA and there are 100 winding per millimeter, the resulting strength of the magnetic field is in the order of 1 kT. The electrons are only partially immersed in this field, so that the expectation value of the magnetic field $\langle B \rangle$ is maybe only one tenth of this value (i.e. 100 T).

The potential energy of an electron is lowered by the following amount, when the electron spin aligns itself to the effective magnetic field:

(263) $\Delta E = \mu_B \langle B \rangle \approx 0.006 eV$

The inductance per unit of length of a solenoid in vacuum is:

(264) $\frac{L}{l} = \mu_0 \left(\frac{N}{l} \right)^2 A$, where A is the cross section area of the solenoid

Assuming that a CP has a solenoid radius of 10 micrometer and 100 turns per millimeter, the inductance per unit of length would be about 4 nH per millimeter of solenoid length, i.e. about 0.6 nH per millimeter of plasma length.

In comparison, the inductance of a straight CP in the golden configuration (see chapter 5.1) is about 4nH per millimeter of plasma length. This means, the inductance of a CP will be dominated by equation (131) rather than by equation (264).

Equation (264) will become inaccurate, if the spacing between the windings is becoming much larger than the diameter of the solenoid "wire", as is often the case with CPs.

The cyclotron frequency of the electrons is given by:

(265) $f_c = \frac{e\langle B \rangle}{2\pi m_e}$

At $\langle B \rangle = 100T$ the cyclotron frequency of the electrons is about 2.8 THz.

The radius of the cyclotron orbits is:

(266) $r_c = \frac{m_e v}{e\langle B \rangle} \approx 6.8\mu m$, where *v* is the electron velocity

The computed cyclotron radius is roughly commensurate with the above assumption that the solenoid radius is 10 µm.

4.2 Polarization of the Electron Gas around the Nuclei

Simplification (84) models the nuclear charges as a uniform jellium, rather than charged points in space. The resulting electron orbitals are therefore not forming density cusps around the nuclei as one would expect to occur in reality.

It is intuitively clear that the resulting formation energy with the jellium approach is higher (i.e. more endothermic) than in reality, where the electrons in the cusps on average come closer to the positive charge of the nuclei.

As an extension of the cylindrical model one can quantify the static electron polarization around the nuclei (i.e. cusps) by means of Thomas-Fermi screening. The contribution of the cusps to the total formation energy of a CP can be estimated with this.

Assuming the electron temperature in a CP is $T_e < 10^5 K$ and the Fermi energy of the electrons (i.e. the difference between the highest and the lowest occupied electron eigenvalue) is $\overline{E}_F > 10^5 eV$, then $k_B T_e < 8.6eV << \overline{E}_F$. Therefore, Thomas-Fermi can be applied to a CP safely at the $T_e \to 0$ limit.

For a Fermi gas at $T = 0$ the state density at the Fermi edge is:

(267) $\frac{\partial n}{\partial \mu} = \frac{3}{2}\frac{n}{\overline{E}_F}$, where *n* is the electron number density and μ is the internal chemical potential

Usually, the above equation is used for computing the screening wave number of Thomas-Fermi screening. However, the electron gas of a CP is not free, because it is bound to a potential well in radial direction.

As can be seen in Figure 62, the electron state density distribution in a CP differs from a free electron gas. The figure shows the state density distribution of a typical CP configuration. The maximum state density per electron is 11.6 MeV^{-1}. The mean expectation value of the electron number density in this case is $\langle n \rangle_{mean} = 0.150\, pm^{-3}$. The mean volume occupied by exactly one electron is $V_{1e} = \langle n \rangle_{mean}^{-1} = 6.67\, pm^3$.

With these values the maximum state density per V_{1e} (i.e. the state density per volume at the Fermi edge) computes as:

(268) $\max\left(\frac{\partial n}{\partial \mu}\right) = \frac{11.6\langle n \rangle_{mean}}{MeV} = \frac{1.74}{MeV \cdot pm^3}$

The Fermi energy in this case is 157 keV. With this, equation (268) can be related to the Fermi energy like:

$$\max\left(\frac{\partial n}{\partial \mu}\right) = \frac{11.6\langle n\rangle_{mean}}{MeV} = 1.82\frac{\langle n\rangle_{mean}}{\overline{E}_F} \quad (269)$$

For computing the Thomas-Fermi screening length in the region of highest electron density, equation (269) will be used below, rather than equation (267).

However, there are uncertainties, which could hamper the application of Thomas-Fermi screening to CPs:

- A strong magnetic field is present, with unclear (at least to the author) consequences to the polarization of the electrons
- It may be incorrect to assume full 3-D screening, because CPs mostly extend in axial direction and have a small radius (in the order of 40 pm, depending on configuration)

Additionally, the Fermi wave number k_F is not a well-defined quantity in CPs, because:

- The axial wave numbers at the occupation edge (Fermi level) are covering the hole range of k-values (in Figure 60), i.e. from 55.6 pm^{-1} through 57.8 pm^{-1}. The mean of these values is 56.3 pm^{-1}, which is translating into an axial De Broglie wave length of 0.112 pm.
- The axial wave numbers are greatly inflated/shifted by the magnetic field. Without this shift, the wave axial numbers at the Fermi level would probably be an order of magnitude smaller
- The maximum occupied wave number is greatly anisotropic in CPs. In radial direction the shortest De Broglie wave length is 2.85 pm, which translates to a wave number of 2.20 pm^{-1}

The Thomas-Fermi model is valid only for wave numbers much smaller than the Fermi wave number k_F. In other words: Modeling the polarization cusps at distances to the nucleus shorter than 2 pm is probably of little value, because the Thomas-Fermi model is just not accurate in this range.

Despite all these uncertainties and in lack of a good alternative, the Thomas-Fermi theory will be applied in the following.

With linearized Thomas-Fermi screening the induced electron charge density is approximated by:

$$\overline{\sigma}_e^{induced}(\vec{r}_n) \approx -e^2 \max\left(\frac{\partial n}{\partial \mu}\right)\Phi^{screened}(\vec{r}_n) \approx -1.82e^2\frac{\langle n\rangle_{mean}}{\overline{E}_F}\Phi^{screened}(\vec{r}_n), \quad (270)$$

where $\Phi^{screened}$ shall be the screened potential of a nucleus and $\vec{r}_n$ is the position relative to the nucleus

In the above equation $\Phi^{screened}$ is defined to approach zero at large $\vec{r}_n$. $\langle n\rangle_{mean}$ is the value of the electron number density at large $\vec{r}_n$.

Relation (270) can be converted into a wave-number-dependent dielectric function (i.e. the relative permittivity):

$\varepsilon_r(k) = 1 + \frac{k_s^{\,2}}{k^2}$, where k is the wave number of the polarization (in momentum space) (271)

and $k_s = \sqrt{\frac{e^2}{\varepsilon_0}\max\left(\frac{\partial n}{\partial \mu}\right)} = \sqrt{\frac{1.82e^2}{\varepsilon_0}\frac{\langle n\rangle_{mean}}{\overline{E}_F}}$ (in SI units) is the Thomas-Fermi screening wave number

The dielectric function can be used to compute the effects of polarization in momentum space:

$$\varepsilon_r(k) = \frac{\overline{\sigma}^{extern}(k)}{\overline{\sigma}^{extern} + \overline{\sigma}_e^{induced}(k)} = 1 - \frac{\overline{\sigma}_e^{induced}(k)}{\overline{\sigma}^{extern} + \overline{\sigma}_e^{induced}(k)} = \frac{\Phi^{extern}(k)}{\Phi^{extern}(k) + \Phi_e^{induced}(k)}, \text{ where} \quad (272)$$

$\overline{\sigma}_e^{induced}(k)$ and $\Phi^{induced}(k)$ are the electron charge density and the potential caused by polarization.

$\overline{\sigma}^{extern}(k)$ and $\Phi^{extern}(k)$ are the charge density and the potential, which caused the polarization.

The Poisson's equation relates the electric potential with the volume charge density:

(273) $\nabla^2 \Phi(\vec{r}) = -\frac{\overline{\sigma}(\vec{r})}{\varepsilon_0}$, where $\vec{r}$ is the position

A nucleus with a point charge of $Q_n = eZ$ will produce a Thomas-Fermi-screened potential of:

(274) $\Phi^{screened}(k) = \frac{e}{\varepsilon_0} \frac{Z}{k^2 + k_s^{\,2}}$

The above equation Fourier-transforms to:

(275) $\Phi^{screened}(\vec{r}_n) = \frac{e}{4\pi\varepsilon_0} \frac{Z}{r_n} \exp(-k_s r_n)$, where $\vec{r}_n$ is the position relative to the nucleus

The quantity $1/k_s$ is the Thomas-Fermi screening length. With the values of $\overline{E}_F = 157keV$ and $\langle n \rangle_{mean} = 0.150 \cdot pm^{-3}$ the screening length computes as:

(276) $\frac{1}{k_s} = \sqrt{\frac{\varepsilon_0}{1.82e^2} \frac{\overline{E}_F}{\langle n \rangle_{mean}}} = 5.64\,pm$

The screening length is a bit shorter than the minimum distance between the nuclei (7.66 pm for the same configuration). This might help to understand, why in a CP the nuclei can have such a high density.

Using (275) with (276), the screened potential is plotting as following:

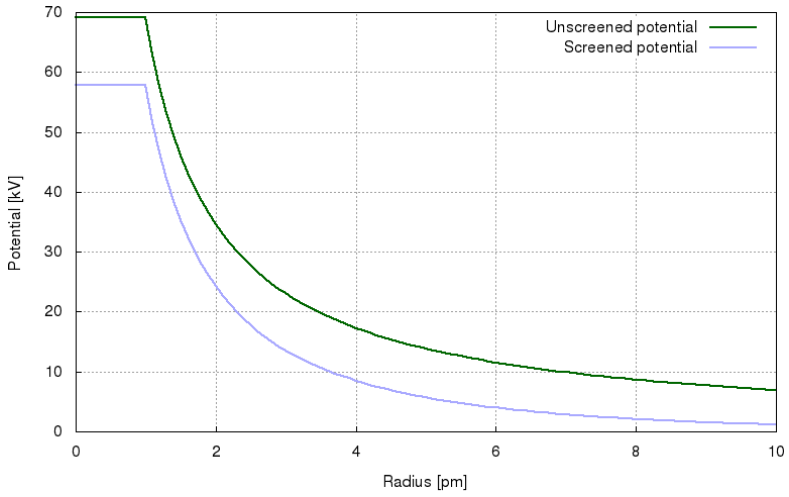

Figure 53 Screened and unscreened potential of a nucleus with nuclear charge Z=48.
The diverging values have been cropped at Radius < 1 pm

The difference between the unscreened potential and the screened potential is not varying much with the radius. This difference can hence be characterized by a constant, i.e. the screening potential:

(277) $\Phi_s = \frac{eZk_s}{4\pi\varepsilon_0} = 12.3kV$, with $Z = 48$ and $k_s^{-1} = 5.64\,pm$

In line with the above example, for the fusion of hydrogen (Z=1) with cadmium (Z=48) the screening potential energy would be $U_s = 12.3keV$. For d-d fusion there would be $U_s = 256eV$ and the minimum distance between neighboring deuterons would be 2.04 pm.

The induced electron density according to equation (270) is plotting as following:

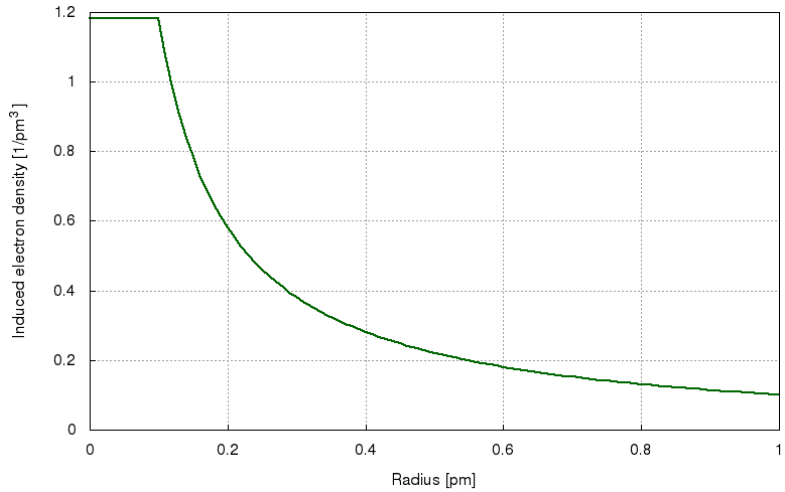

Figure 54 Induced electron density around the nucleus of Figure 53.
The diverging values have been cropped at Radius < 0.1 pm

How much induced charge will be accumulated in a sphere around a nucleus (cusp) with a radius of one third of the distance to the nearest neighbor nucleus (2.47 pm)? This question can be answered by integrating equation (270) and using (275):

$$(278)\quad Q_e^{\,cusp} \approx -1.82e^2 \cdot 4\pi \frac{\langle n \rangle_{mean}}{\overline{E}_F} \int_0^{2.47\,pm} \Phi^{screened}(\vec{r}_n) r_n^{\,2} dr_n$$

$$= -1.82 \frac{e^3 Z}{\varepsilon_0} \frac{\langle n \rangle_{mean}}{\overline{E}_F} \int_0^{2.47\,pm} r_n \exp(-k_s r_n) dr_n$$

$$= 1.82 \frac{e^3 Z}{\varepsilon_0} \frac{\langle n \rangle_{mean}}{\overline{E}_F k_s} \left[r_n \exp(-k_s r_n) + \frac{1}{k_s} \exp(-k_s r_n) \right]_0^{2.47\,pm} = -3.46e$$

The electron density $\overline{\sigma}_e^{\,induced} / e$ surpasses $\langle n \rangle_{mean} = 0.150 / pm^{-3}$ (i.e. the electron density at large $\vec{r}_n$) only at $r_n < 0.71 pm$. For the purpose of estimating the formation energy contribution of the cusp, the integral can therefore be limited to maybe $r_n < 0.71 pm$.

The formation energy between a nucleus (Z=48) and the charge induced by this nucleus in the cusp is:

$$(279)\quad U_{cusp} = 4\pi \int_0^{0.71\,pm} \overline{\sigma}_e^{\,induced}(\vec{r}_n) \Phi^{unscreened}(\vec{r}_n) r_n^{\,2} dr_n$$

$$= -4\pi \cdot 1.82e^2 \frac{\langle n \rangle_{mean}}{\overline{E}_F} \int_0^{0.71\,pm} \Phi^{screened}(\vec{r}_n) \Phi^{unscreened}(\vec{r}_n) r_n^{\,2} dr_n$$

$$= -\frac{1.82e^4 Z^2}{4\pi\varepsilon_0^{\,2}} \frac{\langle n \rangle_{mean}}{\overline{E}_F} \int_0^{0.71\,pm} \exp(-k_s r_n) dr_n = -69.6keV$$

Dividing the result of equation (279) by the number of core electrons per nucleus (=48.96) yields an **estimated contribution of the cusp to the formation energy per electron of -1.42 keV**.

Given that the contribution of the cusps is so small and there are so many uncertainties in applying Thomas-Fermi screening to CPs, the author decided to not include the cusp contribution in the Hamiltonian during the simulation runs.

4.3 Exchange-Correlation Energy Functionals

Local-density approximations (LDA) are approximations to the exchange-correlation energy functional in density functional theory (DFT) that depend solely upon the value of the electron density at each point in space (and not, for example, derivatives of the density).

Using LDA for a CP (in units of the Hartree energy, cylindrical coordinates) provides:

$$(280)\quad E_{xc}[\sigma_e] = \frac{2\pi L}{\lambda_n}\int_0^\infty |\sigma_e(r)|\varepsilon_{xc}[\sigma_e]rdr\,,$$

where σ_e is the electron charge density in natural units according to (200), L is the axial length of the CP in units of the Bohr radius, r is the relative radius coordinate according to (199) and ε_{xc} is the exchange-correlation energy per particle of a homogeneous electron gas of charge density σ_e.

The exchange-correlation energy is decomposed into exchange and correlation terms linearly,

$$(281)\quad \varepsilon_{xc} = \varepsilon_x + \varepsilon_c$$

However, the DFT formalism breaks down, to various degrees, in the presence of a magnetic field. In such a situation, the one-to-one mapping between the ground-state electron density and wave function is lost. Generalizations to include the effects of magnetic fields have led to the current density functional theory and magnetic field density functional theory. For reasons of simplicity, these theories are not engaged here.

The approximation quality of DFT/LDA achievable by neglecting the magnetic field is therefore seen as merely "experimental". Nonetheless, such rogue approach is detailed below.

The analytically known exchange energy functional in LDA is (in units of the Hartree energy, cylindrical coordinates):

$$(282)\quad \varepsilon_x[\sigma_e] = -\frac{3}{4}\sqrt[3]{\frac{3}{\pi}|\sigma_e(r)|}$$

The Chachiyo correlation energy functional (in units of the Hartree energy), which is based on many-body perturbation theory, is applicable to the full range of densities:

$$(283)\quad \varepsilon_c[\sigma_e] = \frac{\ln(2)-1}{2\pi^2}\ln\left(1+\frac{b}{r_s}+\frac{b}{r_s^2}\right),$$

where $r_s = \sqrt[3]{\frac{3}{4\pi}\frac{1}{|\sigma_e|}}$ is the Wigner-Seitz parameter and $b = 20.4562557$

The Wigner-Seitz parameter r_s is defined as the radius of a sphere which encompasses exactly one electron, divided by the Bohr radius.

With the CP configuration of chapter 5.1 the exchange energy per electron is -554 eV and the correlation energy per electron is -4.5 eV. These values are so small (compared to the other terms of the Hamiltonian) that they were not included in the simulation runs. Also, the values could be incorrect due to the strong magnetic field.

5 Computational Results from the Cylindrical Model

5.1 The Physical Properties of the "Golden Configuration"

The author has programmed a "simulator" tool [18], which implements the mathematics of the cylindrical model described in chapter 3. Many different configurations of CPs have been simulated successfully with this tool.

In this chapter here, only one of these configurations will be described, which the author believes is among the most stable ones. This configuration is called the "golden configuration" throughout this document. A discussion about the stability of CPs can be found in chapter 5.4. The influence of varying the input parameters is described in chapter 5.2.

The golden configuration of a CP is characterized by the following **input parameters**:

- The computation was relativistic, i.e. the Klein-Gordon equation was engaged
- A template with 14750 orbital groups was used. The template specifies the quantum numbers *n*, *m* and *l* for groups of electrons. The orbitals (i.e. eigenvalues and eigenstates) of these groups were calculated as candidates for occupation. 7375 of these groups were actually occupied in the order of the computed eigenvalues.
- The length of the CP was set to 9.6 mm
- The nuclei in the jellium had a mean charge of 48 elementary charges
- The linear charge density of the nuclei λ_n was set to 500 elementary charges per picometer length of the CP
- The number of electrons was set to be 102% of the total number of elementary charges contained in all the core nuclei combined
- A halo of cations was configured to reside at a distance of $150\rho_0 = 48.8\,pm$, such that the total charge of the CP is zero (neutral).
- The core nuclear charge distribution was computed according to equation (174) with a standard deviation of $\bar{s} = 90\rho_0 = 29.3\,pm$, a slope parameter of $Slope = 105\rho_0 = 34.2\,pm$ and a cutoff parameter of $Cutoff = 115\rho_0 = 37.4\,pm$
- The maximum number of coefficients c_j of the wave function polynomial was set to 2150
- The axial velocity of the electrons was limited to $10\% \le v_z \le 80\%$ of the speed of light
- The "engineering strength" was 3.0×10^{-6} *)
- The "engineering start" was $100\rho_0 = 32.5\,pm$ *)

*) These parameters will be described in chapter 5.3

The simulator tool in this case had to compute 44 iterations before reaching a self-consistent field status, where the field of the electron charge distribution was self-consistent with the eigenstates of the occupied groups. The tool lists the resulting eigenvalues (in eV) of the groups ordered by their quantum number in a huge table.

The beginning of the eigenvalue table is shown here as a screen shot:

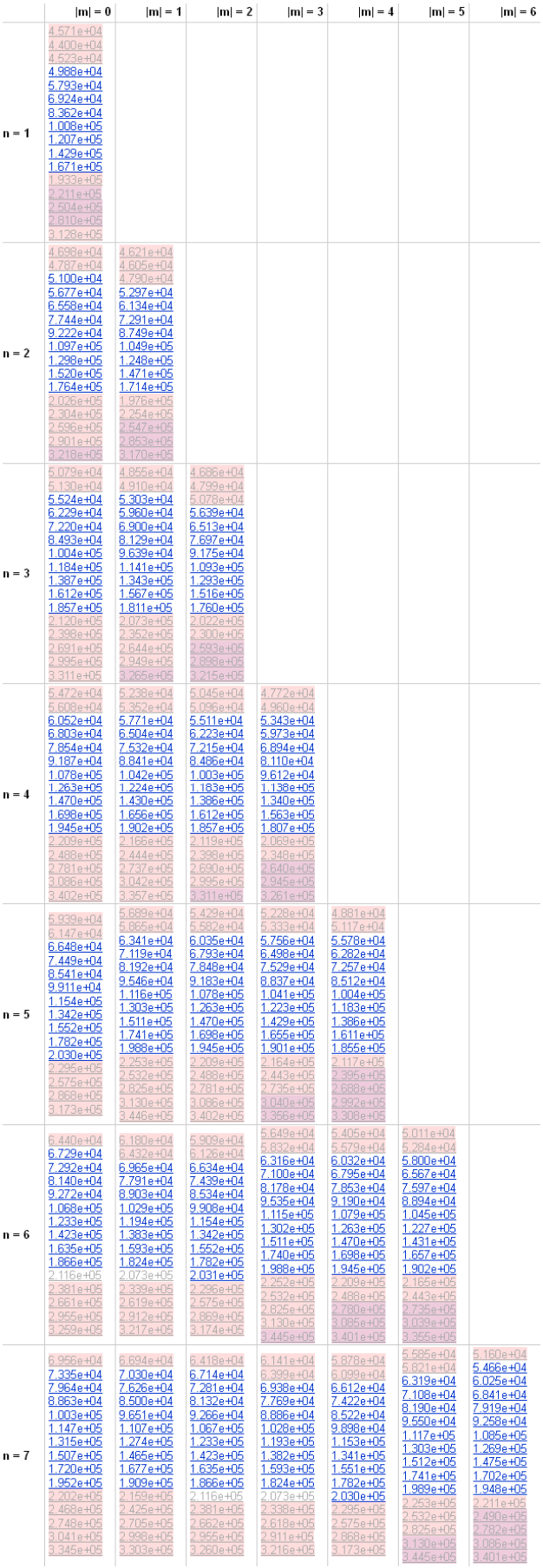

	|m| = 0	|m| = 1	|m| = 2	|m| = 3	|m| = 4	|m| = 5	|m| = 6
n = 1	4.571e+04 4.400e+04 4.523e+04 4.988e+04 5.793e+04 6.924e+04 8.362e+04 1.008e+05 1.207e+05 1.429e+05 1.671e+05 1.933e+05 2.211e+05 2.504e+05 2.810e+05 3.128e+05						
n = 2	4.698e+04 4.787e+04 5.100e+04 5.677e+04 6.558e+04 7.744e+04 9.222e+04 1.097e+05 1.298e+05 1.520e+05 1.764e+05 2.026e+05 2.304e+05 2.596e+05 2.901e+05 3.218e+05	4.621e+04 4.605e+04 4.790e+04 5.297e+04 6.134e+04 7.291e+04 8.749e+04 1.049e+05 1.248e+05 1.471e+05 1.714e+05 1.976e+05 2.254e+05 2.547e+05 2.853e+05 3.170e+05					
n = 3	5.079e+04 5.130e+04 5.524e+04 6.229e+04 7.220e+04 8.493e+04 1.004e+05 1.184e+05 1.387e+05 1.612e+05 1.857e+05 2.120e+05 2.398e+05 2.691e+05 2.995e+05 3.311e+05	4.855e+04 4.910e+04 5.303e+04 5.960e+04 6.900e+04 8.129e+04 9.639e+04 1.141e+05 1.343e+05 1.567e+05 1.811e+05 2.073e+05 2.352e+05 2.644e+05 2.949e+05 3.265e+05	4.686e+04 4.799e+04 5.078e+04 5.639e+04 6.513e+04 7.697e+04 9.175e+04 1.093e+05 1.293e+05 1.516e+05 1.760e+05 2.022e+05 2.300e+05 2.593e+05 2.898e+05 3.215e+05				
n = 4	5.472e+04 5.608e+04 6.052e+04 6.803e+04 7.854e+04 9.187e+04 1.078e+05 1.263e+05 1.470e+05 1.698e+05 1.945e+05 2.209e+05 2.488e+05 2.781e+05 3.086e+05 3.402e+05	5.238e+04 5.352e+04 5.771e+04 6.504e+04 7.532e+04 8.841e+04 1.042e+05 1.224e+05 1.430e+05 1.656e+05 1.902e+05 2.166e+05 2.444e+05 2.737e+05 3.042e+05 3.357e+05	5.045e+04 5.096e+04 5.511e+04 6.223e+04 7.215e+04 8.486e+04 1.003e+05 1.183e+05 1.386e+05 1.612e+05 1.857e+05 2.119e+05 2.398e+05 2.690e+05 2.995e+05 3.311e+05	4.772e+04 4.960e+04 5.343e+04 5.973e+04 6.894e+04 8.110e+04 9.612e+04 1.138e+05 1.340e+05 1.563e+05 1.807e+05 2.069e+05 2.348e+05 2.640e+05 2.945e+05 3.261e+05			
n = 5	5.939e+04 6.147e+04 6.648e+04 7.449e+04 8.541e+04 9.911e+04 1.154e+05 1.342e+05 1.552e+05 1.782e+05 2.030e+05 2.295e+05 2.575e+05 2.868e+05 3.173e+05	5.689e+04 5.865e+04 6.341e+04 7.119e+04 8.192e+04 9.546e+04 1.116e+05 1.303e+05 1.511e+05 1.741e+05 1.988e+05 2.253e+05 2.532e+05 2.825e+05 3.130e+05 3.446e+05	5.429e+04 5.582e+04 6.035e+04 6.793e+04 7.848e+04 9.183e+04 1.078e+05 1.263e+05 1.470e+05 1.698e+05 1.945e+05 2.209e+05 2.488e+05 2.781e+05 3.086e+05 3.402e+05	5.228e+04 5.333e+04 5.756e+04 6.498e+04 7.529e+04 8.837e+04 1.041e+05 1.223e+05 1.429e+05 1.655e+05 1.901e+05 2.164e+05 2.443e+05 2.735e+05 3.040e+05 3.356e+05	4.881e+04 5.117e+04 5.578e+04 6.282e+04 7.257e+04 8.512e+04 1.004e+05 1.183e+05 1.386e+05 1.611e+05 1.855e+05 2.117e+05 2.395e+05 2.688e+05 2.992e+05 3.308e+05		
n = 6	6.440e+04 6.729e+04 7.292e+04 8.140e+04 9.272e+04 1.068e+05 1.233e+05 1.423e+05 1.635e+05 1.866e+05 2.116e+05 2.381e+05 2.661e+05 2.955e+05 3.259e+05	6.180e+04 6.432e+04 6.965e+04 7.791e+04 8.903e+04 1.029e+05 1.194e+05 1.383e+05 1.593e+05 1.824e+05 2.073e+05 2.339e+05 2.619e+05 2.912e+05 3.217e+05	5.909e+04 6.126e+04 6.634e+04 7.439e+04 8.534e+04 9.908e+04 1.154e+05 1.342e+05 1.552e+05 1.782e+05 2.031e+05 2.296e+05 2.575e+05 2.869e+05 3.174e+05	5.649e+04 5.832e+04 6.316e+04 7.100e+04 8.178e+04 9.535e+04 1.115e+05 1.302e+05 1.511e+05 1.740e+05 1.988e+05 2.252e+05 2.532e+05 2.825e+05 3.130e+05 3.445e+05	5.405e+04 5.579e+04 6.032e+04 6.795e+04 7.853e+04 9.190e+04 1.079e+05 1.263e+05 1.470e+05 1.698e+05 1.945e+05 2.209e+05 2.488e+05 2.780e+05 3.085e+05 3.401e+05	5.011e+04 5.284e+04 5.800e+04 6.567e+04 7.597e+04 8.894e+04 1.045e+05 1.227e+05 1.431e+05 1.657e+05 1.902e+05 2.165e+05 2.443e+05 2.735e+05 3.039e+05 3.355e+05	
n = 7	6.956e+04 7.335e+04 7.964e+04 8.863e+04 1.003e+05 1.147e+05 1.315e+05 1.507e+05 1.720e+05 1.952e+05 2.202e+05 2.468e+05 2.748e+05 3.041e+05 3.345e+05	6.694e+04 7.030e+04 7.626e+04 8.500e+04 9.651e+04 1.107e+05 1.274e+05 1.465e+05 1.677e+05 1.909e+05 2.159e+05 2.425e+05 2.705e+05 2.998e+05 3.303e+05	6.418e+04 6.714e+04 7.281e+04 8.132e+04 9.266e+04 1.067e+05 1.233e+05 1.423e+05 1.635e+05 1.866e+05 2.116e+05 2.381e+05 2.662e+05 2.955e+05 3.260e+05	6.141e+04 6.399e+04 6.938e+04 7.769e+04 8.886e+04 1.028e+05 1.193e+05 1.382e+05 1.593e+05 1.824e+05 2.073e+05 2.338e+05 2.618e+05 2.911e+05 3.216e+05	5.878e+04 6.099e+04 6.612e+04 7.422e+04 8.522e+04 9.898e+04 1.153e+05 1.341e+05 1.551e+05 1.782e+05 2.030e+05 2.295e+05 2.575e+05 2.868e+05 3.173e+05	5.585e+04 5.821e+04 6.319e+04 7.108e+04 8.190e+04 9.550e+04 1.117e+05 1.303e+05 1.512e+05 1.741e+05 1.989e+05 2.253e+05 2.532e+05 2.825e+05 3.130e+05 3.445e+05	5.160e+04 5.466e+04 6.025e+04 6.841e+04 7.919e+04 9.258e+04 1.085e+05 1.269e+05 1.475e+05 1.702e+05 1.948e+05 2.211e+05 2.490e+05 2.782e+05 3.086e+05 3.401e+05

Figure 55 Table of the energy eigenvalues (in eV), first part

The end of the eigenvalue table is shown here:

	|m| = 56	|m| = 57	|m| = 58	|m| = 59	|m| = 60	|m| = 61	|m| = 62
n = 57	1.939e+05 2.076e+05 2.234e+05 2.410e+05 2.603e+05						
n = 58	2.056e+05 2.186e+05 2.336e+05 2.504e+05 2.690e+05	1.973e+05 2.111e+05 2.269e+05 2.445e+05 2.638e+05					
n = 59	2.169e+05 2.292e+05 2.436e+05 2.599e+05	2.091e+05 2.222e+05 2.372e+05 2.541e+05 2.727e+05	2.007e+05 2.146e+05 2.304e+05 2.480e+05 2.673e+05				
n = 60			2.127e+05 2.258e+05 2.408e+05 2.578e+05	2.042e+05 2.180e+05 2.339e+05 2.516e+05 2.709e+05			
n = 61					2.077e+05 2.215e+05 2.374e+05 2.551e+05		

Figure 56 Table of the energy eigenvalues (in eV), last part

The eigenvalues within a single field of the table are distinguished by quantum number *l*, i.e. the electrons of the respective groups have different axial velocities.

Each eigenvalue has a hyperlink, which upon clicking opens a detailed description of the respective eigenstate, including a plot of the wave function.

The occupied groups are printed in blue, whereas the unoccupied groups are grayed-out. The orbitals with a pink background are "forbidden" to occupy, because the axial velocity of the electron exceeds the predefined limits.

Plots with samples of the computed wave functions are shown in the following figures:

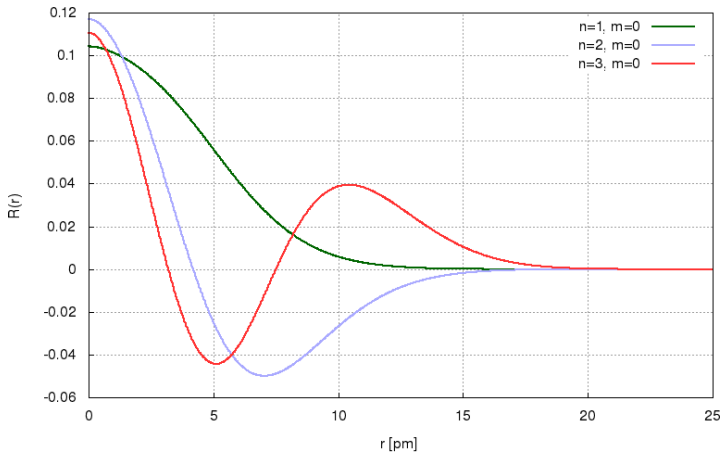

Figure 57 Plots of three radial wave functions R(r) against the radius r
with principle quantum numbers n = 1, 2 and 3 and azimuth quantum number m = 0

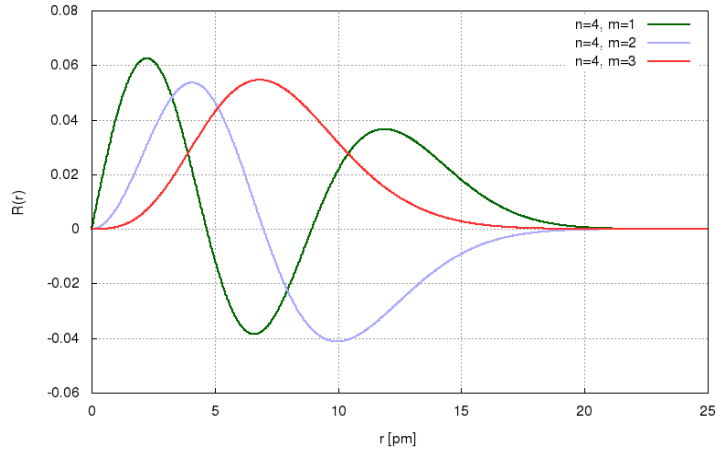

Figure 58 Plots of three radial wave functions R(r) against the radius r
with principle quantum numbers n = 4 and azimuth quantum number m = 1, 2 and 3

As can be seen from Figure 57 and Figure 58, the number of zeros of the wave functions equals n - m, whereby the last zero is at infinite radiuses.

The radial extent of the wave functions generally increases with principal quantum number n.

The eigenvalues of wave functions with identical n and l but different m are non-degenerate (i.e. they are different): The radial extent of a wave function (with a fixed n) decreases and the eigenvalue decreases with increasing m. This is illustrated by the following figure:

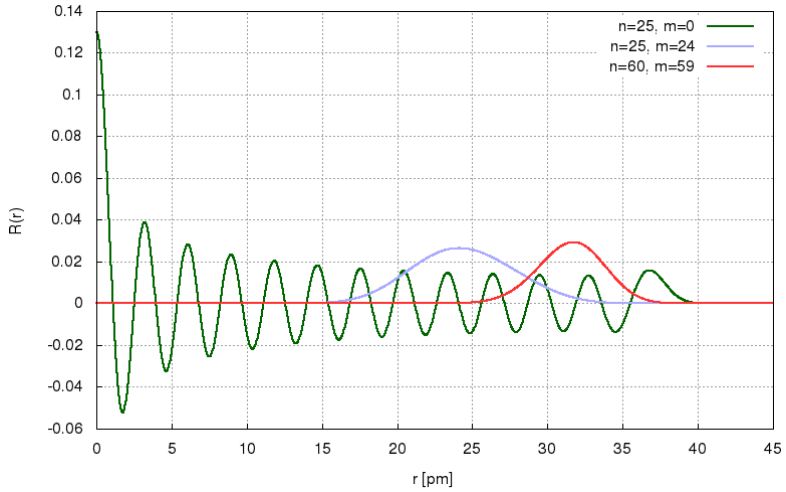

Figure 59 Plots of three radial wave functions R(r) against the radius with large principle quantum numbers

The orbital with quantum numbers $n=25$ and $m=0$ has the largest extent of all occupied orbitals. In comparison, the orbital with $n=25$ (i.e. same value as before) and $m=24$ has a much smaller radial extent. Even the orbital with the largest occupied value of n (i.e. $n=60$) has a smaller extent than the former one, because $m=59$ is at its maximum possible value.

According to the Pauli exclusion principal, the electron wave functions of a CP have to be orthogonal to each other. The simulator tool, while normalizing the wave functions appropriately, spends no CPU time on orthogonalizing the wave functions. Instead, each solution of the Klein-Gordon equation is taken as is. This means, the solutions are not linear-combined to form an orthonormal basis set.

This said, the question arises, just how far away the wave functions are away from being linear independent. To answer this question, two sets of wave functions (with four members each) have been used to form the pair-wise scalar product $\int_0^\infty R_1 R_2 r dr$ between each member within the respective set. The results are showing in the following tables:

	R(n=1)	R(n=2)	R(n=3)	R(n=4)
R(n=1)	1,0000	-0,0001	0,0001	0,0000
R(n=2)	-	1,0000	-0,0004	0,0000
R(n=3)	-	-	1,0000	-0,0006
R(n=4)	-	-	-	1,0000

Table 1 Scalar products of four wave functions with m=0, l=8.70×10^{10}

	R(n=4)	R(n=5)	R(n=6)	R(n=7)
R(n=4)	1,0000	-0,0004	0,0000	0,0000
R(n=5)	-	1,0000	-0,0007	0,0000
R(n=6)	-	-	1,0000	-0,0009
R(n=7)	-	-	-	1,0000

Table 2 Scalar products of four wave functions with m=3, l=8.70×10^{10}

The author thinks that the orthogonality of the wave functions is "good enough" (without further processing) for the purposes of the subsequent evaluations (such as the charge density and the current density distributions).

The symmetry of the axial velocity distribution is broken, i.e. it is not centered symmetrically on zero. The axial velocity correlates with the wave number of the axial De Broglie waves. The wave number distribution is also asymmetric. Both distributions can be seen in the following figure:

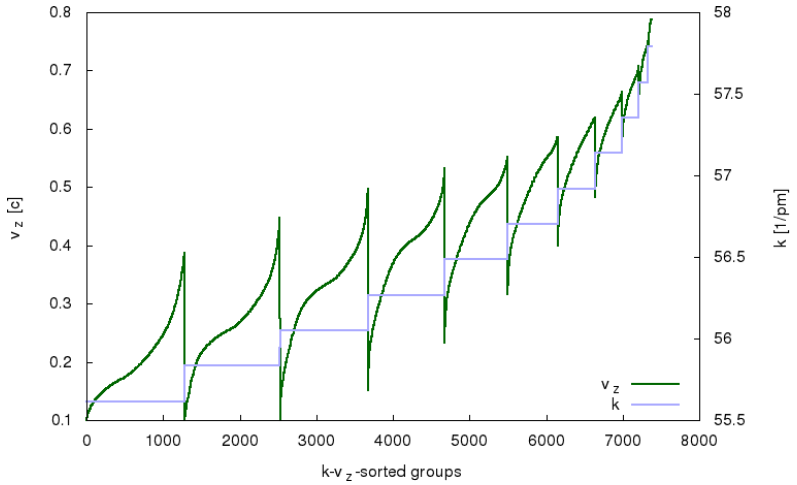

Figure 60 Distributions of the electron's axial velocities (v_z) and axial wave numbers (k).
The occupied groups have been sorted at first by wave number.
Within the ranges of constant wave numbers the groups have then been sorted by velocity.

All electrons are moving in positive z-direction, as specified by the input parameters. Additionally, the minimum velocity of the groups is further limited by the orbital template, such that the electrons are safely confined by the magnetic field and therefore will not tunnel out of the CP.

The staircase shape of the wave number graph is an artifact from electron grouping: A whole range of wave numbers is represented by its mean value of the group. With larger number of groups in the simulation template, the steps are getting smaller.

The velocity ranges for neighboring wave number values are overlapping, which results in the saw teeth shape of the velocity distribution graph.

Surprisingly, the axial wave numbers reside in a small interval, although the velocities cover a wide range. This can be explained by the Aharonov-Bohm effect, which according to equation (104) offsets the kinetic momentum $\hat{p}$ by $e\vec{A}$ from the canonical momentum (i.e. from the De Broglie wave numbers).

The energy eigenvalues of the occupied orbitals is distributed according to the following figure:

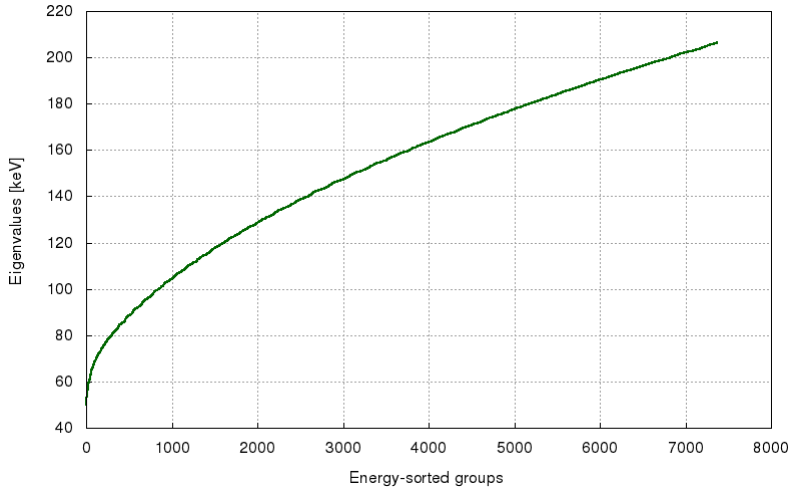

Figure 61 Electron eigenvalue distribution. The occupied groups have been sorted by energy eigenvalue.

The information contained in the eigenvalue distribution can alternatively be displayed as an electron state density distribution, as following. The latter is important as a fundamental thermodynamic quantity and for analyzing Thomas-Fermi screening.

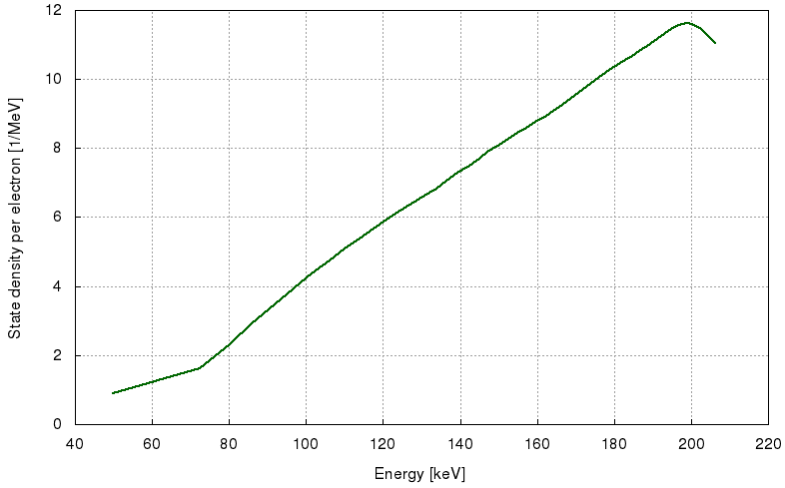

Figure 62 Electron state density distribution. It has been computed by exchanging the x and y axes of Figure 61 and then forming the first derivative via numerical derivation. The state density measures, how many quantum states per electron exist in an infinitesimal energy interval.

By adding the modulus square of all (occupied) wave functions together according to equation (216), one gets the electron density distribution. Multiplication of each summand with the axial kinetic momentum according to equation (217) computes the current density distribution:

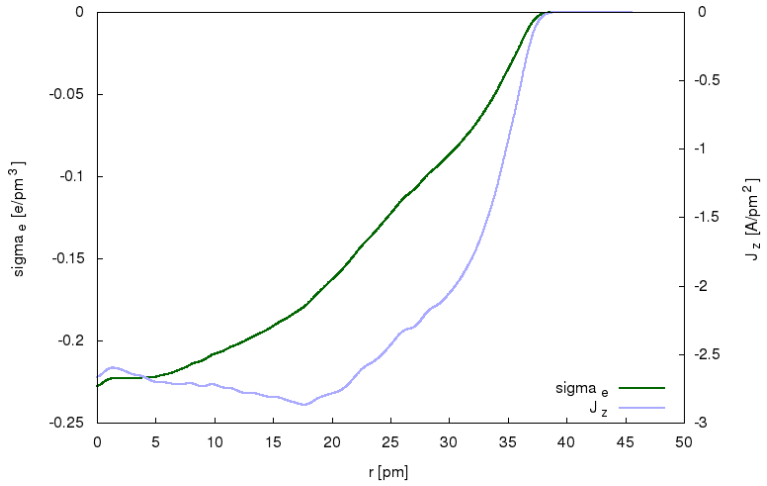

Figure 63 Radial distributions of the electron charge density ($sigma_e$) and the current density (J_z)

The values shown in the above figure are quite remarkable: No other aggregation state of matter allows for nearly as high electron and current densities! To put this in perspective: One would not want to exceed a current density of 5 A/mm^2 in a transformer winding in order to protect against overheating. This is about 18 orders of magnitude below the maximum current density in this CP!

The charge density distribution of the nuclear jellium in the core is modeled via equation (228). At radius values around 32 pm the electron charge density exceeds the nuclear charge density. The resulting total charge density distribution can be seen in the following figure:

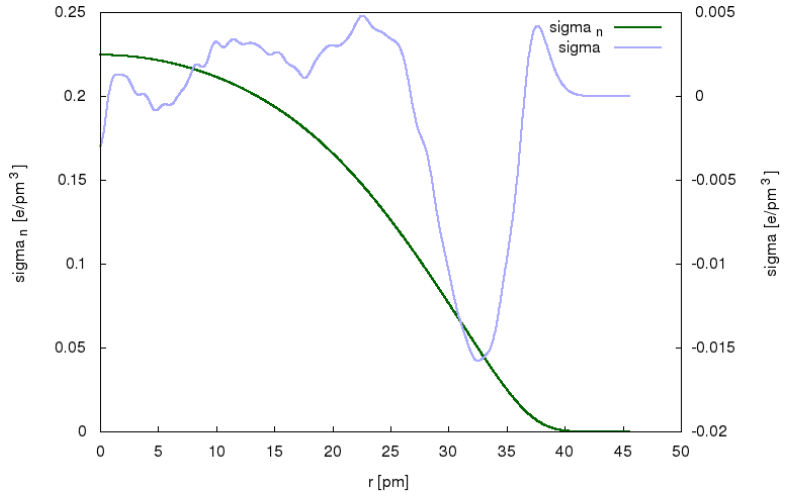

Figure 64 Radial Distributions of the core nuclear charge density (sigma$_n$) versus the total charge density (sigma)

By means of equations (219) and (222) the simulator computes from the charge density and current density distributions the electric and magnetic potentials:

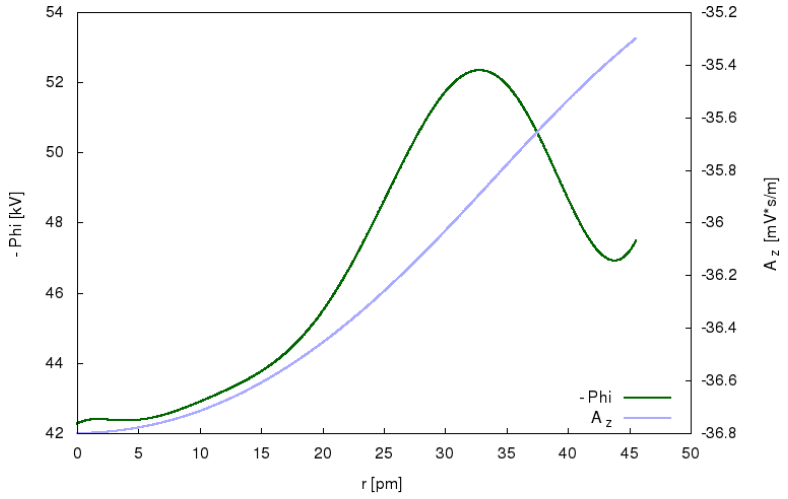

Figure 65 Electric potential (Phi) and magnetic potential (A_z)

Note that the potentials are deep, but they do not vary much in the radial interval of interest.

The gradient of these potentials give the electric and magnetic fields as a function of the radius:

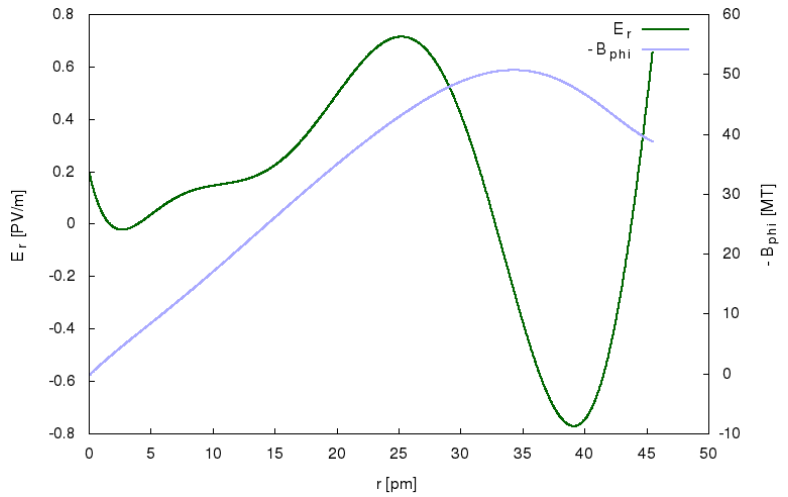

Figure 66 Radial electric field (E_r) and azimuthal magnetic field (B_{phi})

The electric field strength is between -772 and plus +714 volt per picometer. The magnetic field goes up to 50.7 megatesla! To put that in perspective: The strength of the magnetic field in pulsars can be up to 100 megatesla.

Other computation results for the golden configuration are as following:

- The reference radius ρ_0 computes as 0.325 pm.
- The total nuclear charge of the CP core is 7.69×10^{-7} Coulomb
- The total charge of the halo cations is an additional 1.54×10^{-8} Coulomb
- The CP contains 100 billion nuclei
- There are 4.90×10^{12} electrons in the CP
- Each electron group contains 664 million electrons
- The minimum nuclear distance is 7.42 pm between cadmium nuclei, 4.08 pm between oxygen nuclei and 2.04 pm between hydrogen nuclei.
- The maximum matter density in the CP core is 647 kg/cm^3 for cadmium, 92.0 kg/cm^3 for oxygen and 5.80 kg/cm^3 for hydrogen. For cadmium this is about 75,000 times denser than ordinary metal.
- The nuclear self-repulsion energy is 14.5 MeV per electron (i.e. the Coulomb energy from nucleus-nucleus interaction). This value includes 539 keV core-halo repulsion energy, 5.39 keV halo-halo self-repulsion energy and -9.41 keV granularity correction of the core self-repulsion energy.
- The formation energy computes as 92.3 keV per electron (endothermic). The total formation energy of the CP therefore is 0.0725 J. This is equivalent to the energy stored in a 33 nF capacitor, which is charged to 2100 V. *)
- The lowest occupied orbital eigenvalue is 49.9 keV *)
- The highest occupied eigenvalue (i.e. the internal chemical potential, aka "Fermi level") is 206 keV *)
- The Fermi energy (computed as the difference between highest and lowest eigenvalue) is 156 keV
- The mean expectation value of the electron radius is 20.2 pm
- The mean expectation value of the electron charge density is -0.150 e/pm^3
- The mean expectation value of the axial current density is -2.48 A/pm^2
- The mean axial velocity of the electrons is 37.6% of the speed of light
- The kinetic energy of the electrons ranges from 1.9 to 155 keV, stemming mostly from the axial movement
- The axial De Broglie wavelength of the electrons ranges from 0.108 pm to 0.113 pm
- The total axial current in the CP is -9.21 kA

*) Cautionary comment: The computed results of the formation energy and the eigenvalues seem to be not well-aligned with key experimental findings. According to Ken Shoulders [2] CPs can be created with less than 10^{-6} J of energy. For a further discussion of this, please refer to chapter 5.4.

For computing the impedance, capacitance and inductance of the golden CP configuration it is assumed that the CP is attached to the surface of a dielectric plate with a thickness of 1 mm and a relative permittivity of 4. It is further assumed that a conducting plate is attached at the other side of the dielectric plate. The conducting plate is the return path for the current flowing through the CP.

Using equations (128) and (129) the characteristic impedance of the CP computes as $Z_0 = 698\Omega$.

Using equations (129) and (130) the capacitance of the CP computes as $C = 0.0725\,pF$.

Using equation (131) the inductance of the CP is $\Lambda = 35.3nH$.

The magnetic flux of the CP computes as $\Phi_B = \Lambda I = 325\mu Wb$.

The energy of CP's magnetic flux is $\overline{E}_M = \frac{1}{2}\Lambda I^2 = 1.50J$. This is equivalent to an energy of 1.91 MeV per electron.

As a plausibility check on pressures according to equation (182) the following diagrams have been computed:

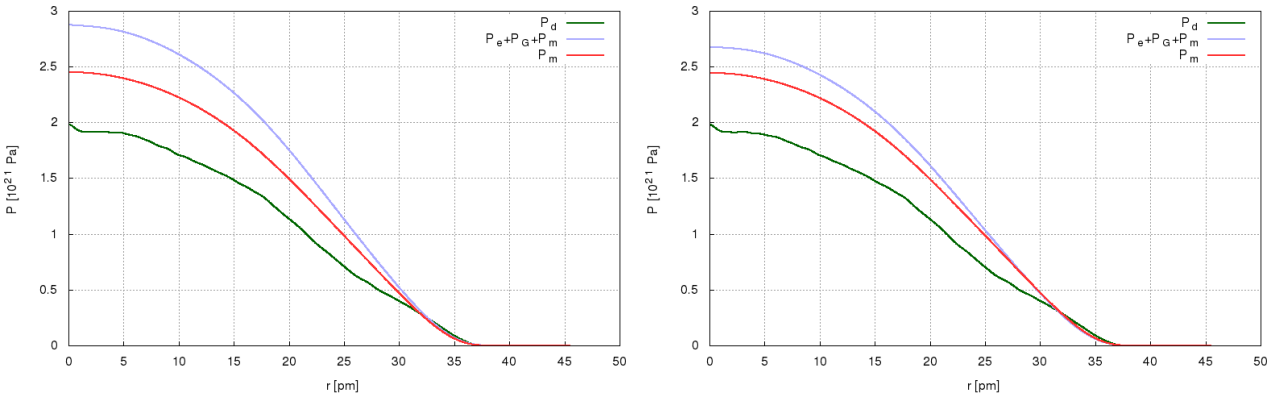

Figure 67 Total pressure $P_e+P_G+P_m$ inside a CP compared to the degeneracy pressure P_d of the electron gas and the pressure P_m exerted by the magnetic field.
The diagram at the left side is for Z_m=48 and the diagram at the right side is for Z_m=1

Astonishingly, the total pressure inside a CP is exceeding 2×10^{21} Pa at low radius values! This pressure is five orders of magnitude higher than the pressure in the middle of the solar core (2.65×10^{16} Pa), but lower than the pressure in a neutron star (3.2×10^{31} to 1.6×10^{34} Pa).

The plasma inside a CP is predominantly confined/compressed by the magnetic force on the electrons (z-pinch condition). The compression is roughly commensurate to the degeneracy pressure of the resulting electron density. It was the purpose of the plausibility check to demonstrate this.

In Figure 67 the different values of the total pressure at different Z_m are caused by different results for the granularity correction P_G.

In the following, the energy balance of a particular electron will be analyzed according to some terms of the Klein-Gordon equation. The orbital with principal quantum number n=14, angular quantum number m=7 and an axial wave number k = 56.5 pm^{-1} (corresponding to an axial velocity of 0.391 c) has been chosen as a sample:

- The energy eigenvalue $\overline{E}_h E$ of the electron state is 128 keV
- The expectation value of the electron-electron Coulomb energy $\left\langle \overline{E}_h E_{C,e} \right\rangle$ is 29.206 MeV
- The expectation value of the electron-nucleus Coulomb energy $\left\langle \overline{E}_h \left(E_{C,n} + E_{C,h} \right) \right\rangle$ is -29.156 MeV
- The expectation value of the electron-nucleus granularity correction $\left\langle \overline{E}_h E_{G,e} \right\rangle$ is -5.1 keV
- The expectation value of the kinetic energy $\left\langle \overline{E}_h \left(E - E_C - E_{G,e} \right) \right\rangle$ is 77.1 keV *)
- The term $\overline{E}_h P_z^{\,2}/2$ yields 121.559 MeV
- The expectation value of the magnetic interaction energy $\left\langle -\overline{E}_h A_z P_z \right\rangle$ computes as -238.764 MeV
- The expectation value of the diamagnetic energy $\left\langle -\overline{E}_h A_z^{\,2}/2 \right\rangle$ is 117.248 MeV
- The expectation value of the axial kinetic energy term $\left\langle \overline{E}_h p_z^{\,2}/2 \right\rangle$ is 43 keV
- The expectation value of the rotational energy term $\left\langle \overline{E}_h \lambda_n m^2/2r^2 \right\rangle$ is 15.7 keV
- The expectation value of the radial kinetic energy term $\left\langle \overline{E}_h \left(-\frac{\lambda_n}{2} R'' - \frac{\lambda_n}{2r} R' \right) \frac{1}{R} \right\rangle$ is 29.9 keV
- Just for comparison: The nuclear self-repulsion energy per electron is 14.484 MeV (But this is not a term of the Klein-Gordon equation)

5.2 Varying the Input Parameters

The most prominent changes of the simulation results occur, when the linear charge density of the core λ_n is varied. The total number of nuclei and electrons in the CP has been kept constant for this comparison:

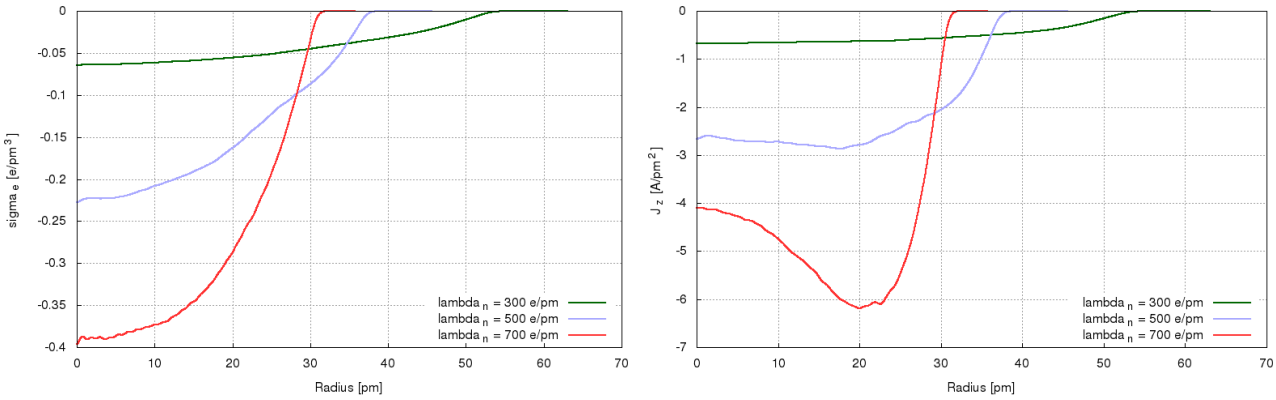

Figure 68 Electron charge density distribution (left) and current density distribution (right) at different values for the linear charge density lambda_n of the nuclei

With larger densities λ_n the CP is becoming thinner, while the electron density increases. The current density does not change in exactly the same way, because of two counteracting effects: The radial extent of the current distribution is also becoming thinner at larger densities λ_n, but the radius value at the maximum current density is becoming larger, i.e. at high-density configurations the current flows mostly at the outer layer of the electrons.

Other key properties of a CP also change significantly, when the linear charge density of the core nuclei λ_n is varied:

Linear charge density of the core [e/pm]	100	200	300	400	500	600	700	800
CP length [mm]	48	24	16	12	9.6	8	6.86	6
Mean expectation value of the electron radius [pm]	66.2	39.6	29.2	23.7	20.2	17.8	17.0	16.3
Mean expectation value of the electron charge density [e/pm^3]	-0.0029	-0.0159	-0.0433	-0.0875	-0.150	-0.231	-0.297	-0.374
Mean expectation value of the current density [A/pm^2]	-0.0222	-0.160	-0.529	-1.24	-2.48	-4.06	-5.26	-6.81
Formation energy per electron [keV]	9.79	24.4	43.4	65.2	92.3	118	136	158
Min. electric potential of the core [kV]	-7.36	-18.3	-27.9	-39.5	-52.3	-60.7	-66.6	-79.6
Total axial current [kA]	-0.779	-2.08	-3.90	-6.15	-9.21	-12.0	-14.2	-16.7
Mean axial velocity [c]	0.159	0.213	0.265	0.314	0.376	0.409	0.414	0.426
Max. magnetic flux density [MT]	1.43	6.24	15.3	29.3	50.7	74.8	94.6	119
Characteristic Impedance [Ω]	653	673	684	692	698	703	705	706
Inductance [nH]	165	85.1	57.7	43.8	35.3	29.7	25.5	22.4
Capacitance [fF]	388	188	123	91.5	72.5	60.0	51.4	44.8
Magnetic flux [μWb]	129	177	225	269	326	356	362	373
Energy of the magnetic flux per electron [MeV]	0.0639	0.235	0.560	1.06	1.91	2.72	3.28	3.98
Minimum nuclear distance (Z_m=48, 8 and 1) [pm]	27.8 15.3 7.65	15.7 8.64 4.32	11.2 6.16 3.08	8.80 4.84 2.42	7.42 4.08 2.04	6.52 3.59 1.79	6.16 3.39 1.69	5.83 3.21 1.60
Lowest occupied orbital eigenvalue [keV]	8.35	15.5	22.9	28.5	49.9	58.3	72.4	87.3
Highest occupied orbital eigenvalue [keV]	26.4	61.5	102	147	206	258	298	350
Max. state density per electron [1/MeV]	114	42.9	25.7	18.2	11.6	8.83	7.56	6.03

Table 3 Changes of key properties, when the linear charge density of the core nuclei λ_n is varied (the "golden configuration" is marked yellow)

Varying λ_n strongly changes the eigenvalue distribution:

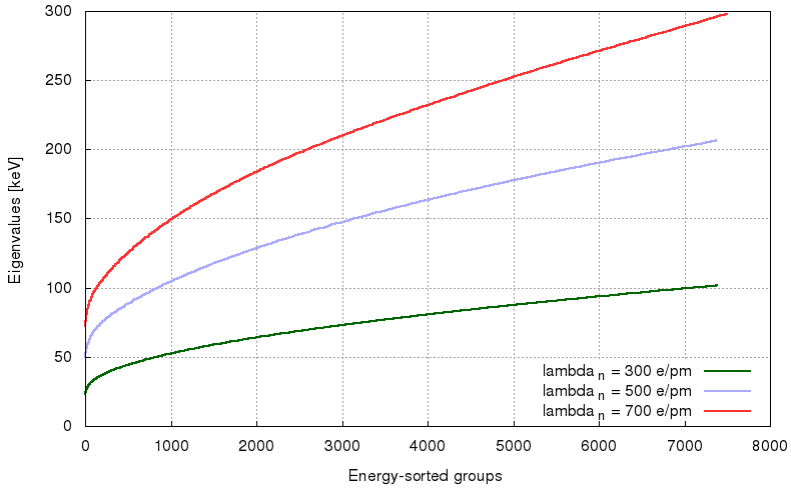

Figure 69 Changes of the eigenvalue distribution, when λ_n is varied

The minimum axial velocity also has strong influence on the properties of the CP, mainly because it changes the axial current of the CP:

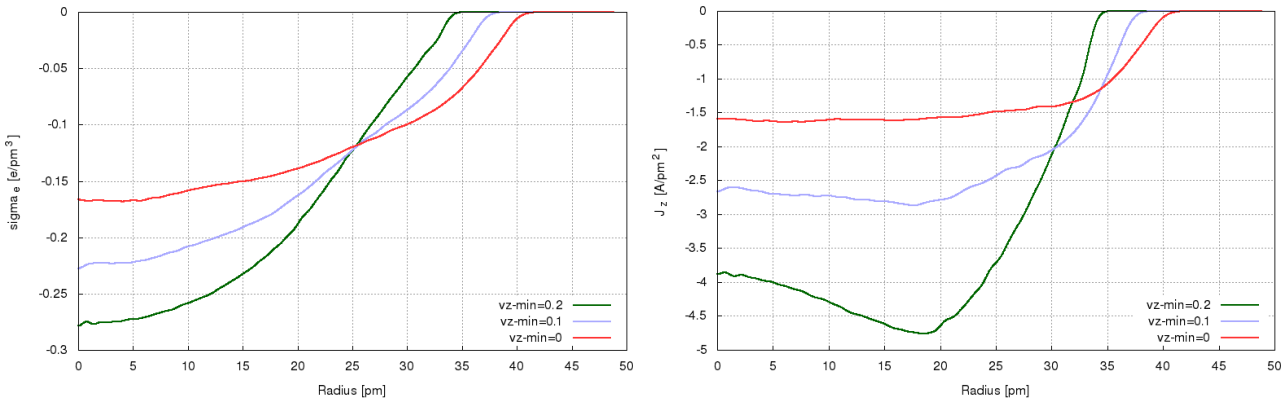

Figure 70 Electron charge density distribution (left) and current density distribution (right) at different values of the minimum axial velocity (in units of the light speed) of the electrons

Varying the minimum axial velocity is changing the eigenvalues, because of the differences in the axial kinetic energy:

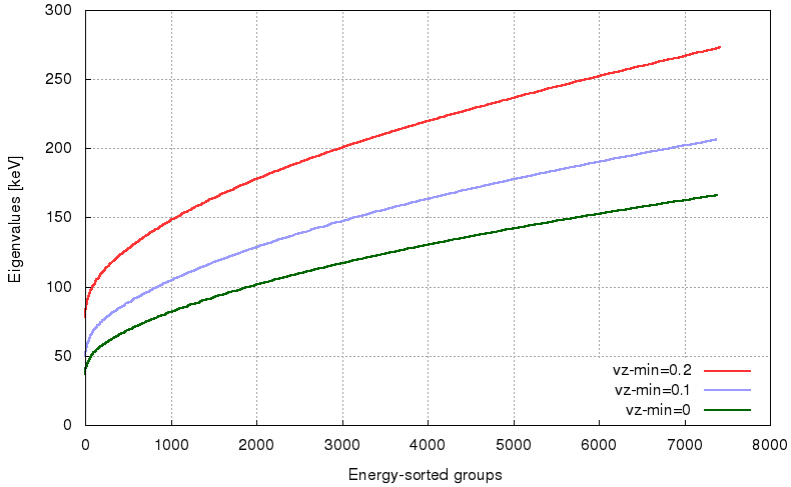

Figure 71 Changes of the eigenvalue distribution, when the minimum axial velocity is varied

Other key properties are changing with the minimum axial velocity as following:

	$v_{z,\min} = 0$	$v_{z,\min} = 0.1 \cdot c$	$v_{z,\min} = 0.2 \cdot c$
Formation energy	66.1 keV	92.3 keV	132 keV
Total axial current	-6.38 kA	-9.21 kA	-12.2 kA
Mean axial velocity	0.260 c	0.376 c	0.498 c
Mean expectation value of the electron radius	22.7 pm	20.2 pm	18.0 pm
Mean expectation value of the electron charge density	-0.120 [e/pm^3]	-0.150 [e/pm^3]	-0.190 [e/pm^3]
Mean expectation value of the current density	-1.43 [A/pm^2]	-2.48 [A/pm^2]	-4.05 [A/pm^2]
Min. electric potential of the core	-48.5 kV	-52.3 kV	-63.3 kV
Max. magnetic flux density	-32.6 MT	-50.7 MT	-74.4 MT
Minimum nuclear distance (Z_m=48)	8.15 pm	7.42 pm	6.92 pm
Lowest occupied orbital eigenvalue	36.9 keV	49.9 keV	78.1 keV
Highest occupied orbital eigenvalue	166 keV	206 keV	273 keV

Table 4 Changes of key properties, when the minimum of the axial velocity of the electrons is varied

The following diagrams are comparing the results of non-relativistic simulations (via the Schrödinger equation) with relativistic simulations (via the Klein-Gordon equation):

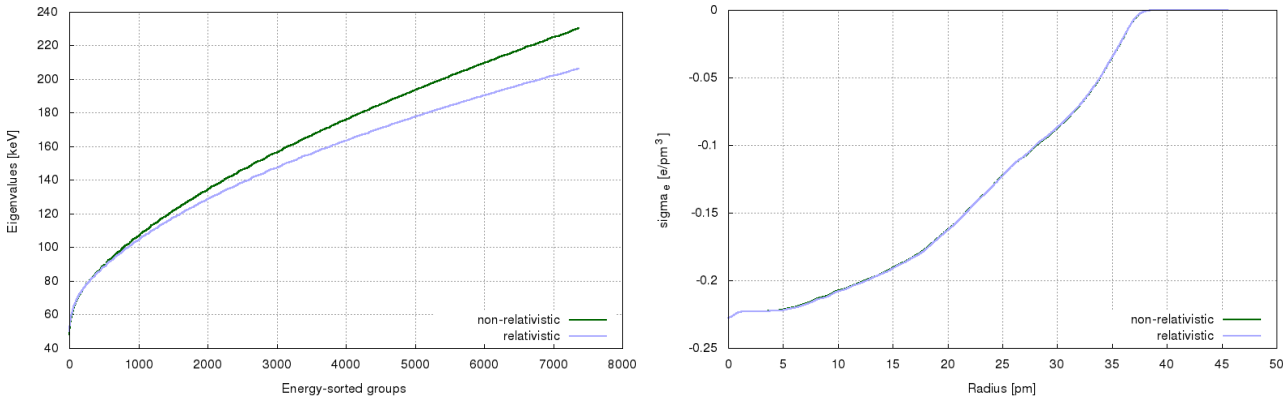

Figure 72 Eigenvalue distribution and electron charge density distribution, non-relativistic versus relativistic

As can be seen above, there is virtually no difference in the electron charge distributions for both types of simulation runs. The same is true for the individual wave functions.

However, the eigenvalue distribution changes markedly between non-relativistic versus relativistic simulations. These changes lead to a higher (i.e. more endothermic) formation energy and a lower state density at non-relativist runs.

Except for the purpose of this comparison here, all properties of CPs were obtained by relativistic simulations.

A comparison of other properties, as they change between non-relativistic and relativistic simulations, can be seen in the following table:

	Non-relativistic	Relativistic
Formation energy	105 keV	92.3 keV
Total axial current	-9.21 kA	-9.21 kA
Mean axial velocity	0.376 c	0.376 c
Minimum nuclear distance (Z_m=48)	7.42 pm	7.42 pm
Lowest occupied orbital eigenvalue	48.4 keV	49.9 keV
Highest occupied orbital eigenvalue	230 keV	206 keV

Table 5 Key properties, non-relativistic versus relativistic

The length of a CP $\overline{L}$ has only minor influence on the resulting properties. The length has been changed over four orders of magnitude for demonstrating the effect:

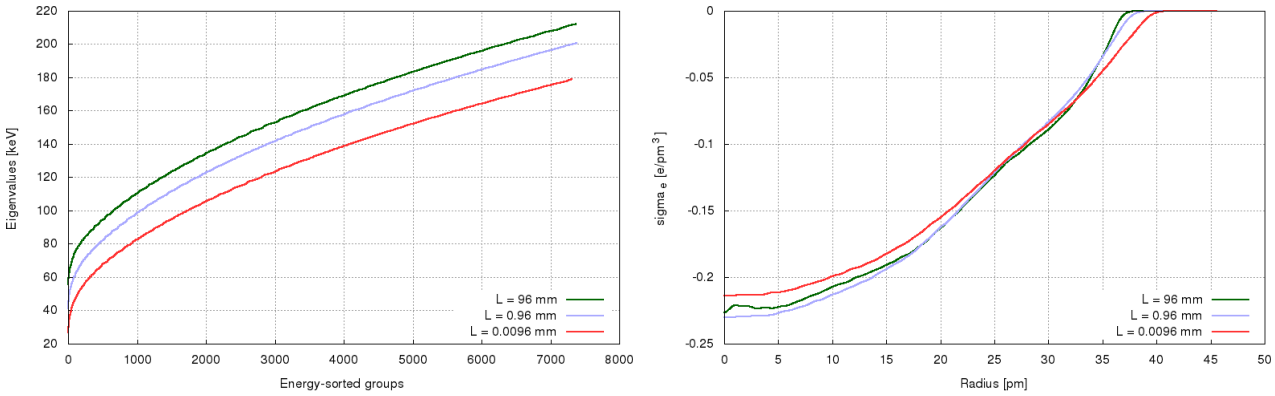

Figure 73 Eigenvalue distribution and electron charge density distribution at different values of the CP length

For geometric reasons the CP length has direct impact on the depth of the electric and magnetic potentials. The variance in the potentials is then leading to changes in the eigenvalues. Interestingly, these changes in eigenvalues don't impact the formation energy. Other key properties of a CP are changing only slightly by varying $\overline{L}$:

	$\overline{L}$ = 0.0096 mm	$\overline{L}$ = 0.096 mm	$\overline{L}$ = 0.96 mm	$\overline{L}$ = 9.6 mm	$\overline{L}$ = 96 mm
Formation energy	87.5 keV	90.8 keV	93.2 keV	92.3 keV	91.8 keV
Total axial current	-8.87 kA	-9.14 kA	-9.30 kA	-9.21 kA	-9.12 kA
Mean axial velocity	0.362 c	0.373 c	0.380 c	0.376 c	0.372 c
Min. electric potential of the core	-34.8 kV	-41.1 kV	-47.1 kV	-52.3 kV	-58.4 kV
Max. magnetic potential	-23.2 mV·s/m	-28.1 mV·s/m	-32.9 mV·s/m	-36.8 mV·s/m	-40.7 mV·s/m
Minimum nuclear distance (Z_m=48)	7.52 pm	7.43 pm	7.34 pm	7.42 pm	7.42 pm
Lowest occupied orbital eigenvalue	27.0 keV	35.0 keV	41.4 keV	49.9 keV	55.7 keV
Highest occupied orbital eigenvalue	179 keV	191 keV	201 keV	206 keV	212 keV

Table 6 Changes of key properties, when $\overline{L}$ is varied

The number of electrons in the CP core in excess of the number of positive charges of the core nuclei cannot be computed directly, because it would require a better modeling of the halo properties. The number of electrons has rather to be set as an input parameter to the simulation runs.

The following compares the influence of changing the number of electrons in a CP. The halo charge has been adjusted such that the total charge of the CP is neutral (All other simulation runs in this document were using a number of electrons, which is 102% of the number of core nuclear charges):

Number of electrons	100.5 %	102%	108%	108%
Number of halo charges	0.5%	2%	8%	0
Formation energy	91.1 keV	92.3 keV	95.4 keV	177 keV
Total axial current	-9.07 kA	-9.21 kA	-9.52 kA	-9.52 kA
Mean axial velocity	0.376 c	0.376 c	0.367 c	0.367 c
Min. electric potential of the core	-44.9 kV	-52.3 kV	-88.9 kV	-2.29 MV
Min. electric field	-0.170 PV/m	-0.772 PV/m	-3.10 PV/m	-3.09 PV/m
Max. magnetic potential	-36.3 mV·s/m	-36.8 mV·s/m	-38.0 mV·s/m	-38.0 mV·s/m
Minimum nuclear distance (Z_m=48)	7.42 pm	7.42 pm	7.49 pm	7.49 pm
Lowest occupied orbital eigenvalue	38.5 keV	49.9 keV	93.5 keV	2.29 MeV
Highest occupied orbital eigenvalue	196 keV	206 keV	244 keV	2.44 MeV

Table 7 Changes of key properties, when the number of electrons (as a percentage of core nuclear charges) is varied

5.3 The CP Simulator Tool and its Limitation

As said, the simulator tool was programmed to obtain the computational results. It can be accessed via a Web interface by any registered user, see [18].

The tool is written in C. It uses a MySQL database for archiving computational results. The performance of the tool is quite high: A simulation run with a template of 15000 groups and 2000 wave function coefficients takes about one day (while running typically 40 SCF iterations) to compute on a one-core virtual machine with two gigabytes of main memory. Computation time raises quadratic with the number of coefficients.

The tool has a read-only level and a privileged level of user access. Interested researchers can request a password at the login screen, which will grant read-only access. With read-only access one can retrieve the simulation runs, which are archived in the database. The results are displayed as tables and graphical plots.

The privileged level, which allows users to start simulation runs, requires a special agreement with the author, due to the involved compute resources.

There is a known **limitation of the simulator tool**:

The wave functions are starting to diverge at large radius values, if the number of wave function coefficients c_j is made too high, as shown in Figure 51.

There is a correspondence between the radial extent of the wave function and the number of coefficients required for modeling the respective wave function appropriately.

The feasible number of coefficients limits the radial extent of the wave function to about 38 pm for typical configurations with $\lambda_n = 500\, e/pm$. Most wave functions of a CP naturally have a smaller extent, but a fraction of wave functions would exceed this limit. Thus they cannot be modeled accurately.

The simulator tool therefore has to reduce the radial extent of the largest wave functions artificially. This technique has been dubbed "potential engineering" by the author. It adds a small repulsive potential energy at the high end of the radius values like this:

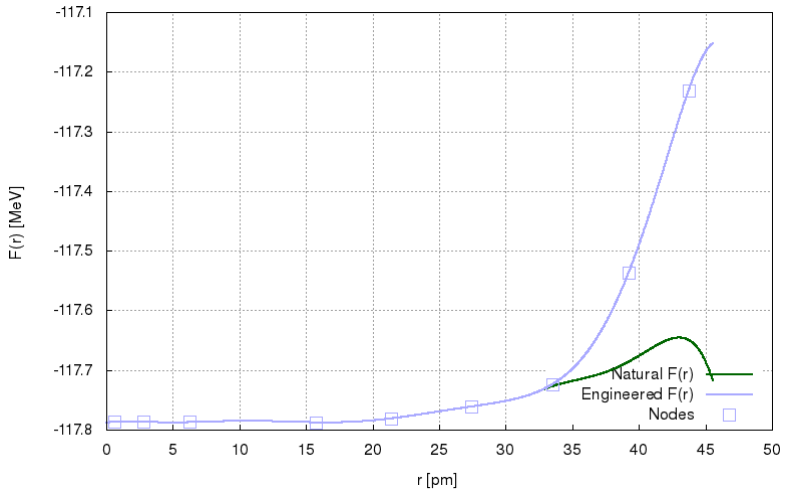

Figure 74 Pseudo potential energy, engineered versus natural.
The nodes for the polynomial interpolation are shown as points.

The pseudo potential energy F(r) in the above graph represents the terms of the Klein-Gordon equation, which are approximated via the b-polynomial of equations (246) and (247).

Most wave functions don't "see" the difference between natural and engineered potential energy, because they don't extend beyond 30 pm. The few wave functions, which are reaching into the engineered area, will compute as having a shorter extent, than without engineering.

The overall impact of potential engineering on the simulation results are minimal, as demonstrated in the following:

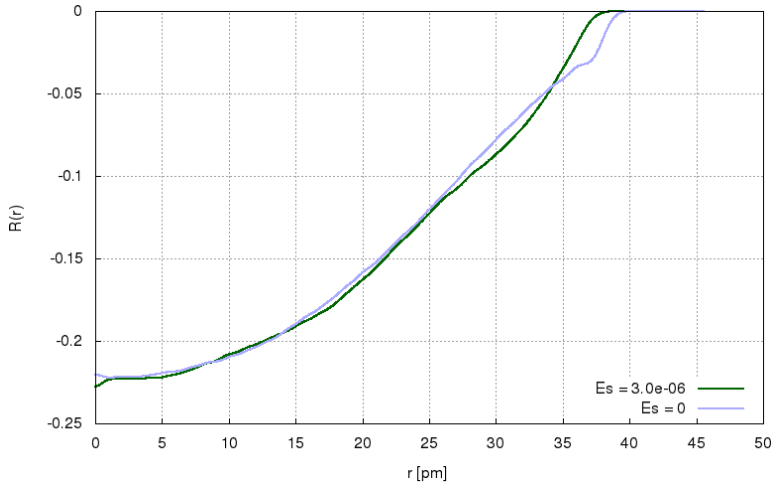

Figure 75 Electron charge density distribution (left) with potential engineering (Es=3.0e-06) and without potential engineering (Es=0)

In the above example the formation energy with potential engineering is 1.8 keV higher (i.e. more endothermic) than without potential engineering. Without potential engineering the radial extent of the wave functions is limited by the number of wave function coefficients c_j, rather than by the potential. Most other properties, such as the total axial current, stay nearly the same.

The simulator tool controls potential engineering by two parameters: The "engineering start" parameter defines the radius value beyond which the potential is modified. The "engineering strength" (Es) parameter controls, how much the potential is changed relative to its natural value. Generally, the potential modification rises with the radius to the power of two.

5.4 Confinement, Stability, Formation energy, Electron Scattering

According to Figure 65 the electric potential in the CP core is below -47.5 keV with an electron surplus of 2% against the nuclear charges. The potential is repulsive to the electrons and attractive to the nuclei. **The electric potential safely confines/traps the nuclei** inside the core.

The negative potential is a direct result of the electron surplus in the CP core. The larger this surplus is, the more negative the potential will become. It is believed that there is an equilibrium of diffusion for the nuclei: If the core potential is becoming too negative, nuclei from the surrounding matter will be pulled into the core. If the core potential is becoming less negative, nuclei from the core will diffuse out and will recombine with electrons from the surrounding matter. A quantitative analysis of this equilibrium is not available, however.

The magnetic potential confines the electrons in radial direction safely, because the axial velocity of the electrons is in positive z-direction. Therefore, the electrons will be compressed against the z-axis (z-pinch).

The confinement of the electrons in axial direction exists only, if the CP has formed a **closed loop**, i.e. the electrons can't escape at the ends.

In open-ended configurations of a CP the electrons will be emitted at one end of the CP, while the other end will be depleted from electrons. It is clear that open-ended CP configurations are not stable. However, they can exist in a transient manner, e. g. while being attached to a cathode and in the presence of a strong electric field. The cathode in this case has to replace the electrons at the positive end of the CP, at the same rate the electrons are emitted at the negative end.

Within the current framework of the cylindrical model the **length stability of a CP** remains to be enigmatic. On one hand, there is ample experimental evidence available (e.g. "heat after death" observations) that CPs are either energetically metastable or dynamically stable with lifetimes sometimes exceeding one hour. On the other hand, a CP with the formation energies according to Table 3 would just elongate itself and decay, because the formation energies fall monotonically with the CP length.

Could the length stability be caused by a yet unknown term of the Hamiltonian, which lowers the formation energy at higher densities? Such term would need to contribute to the formation energy in the order of -100 keV at a density of $\lambda_n = 500\, e/pm$. Note that this energy would be small compared to the largest term of the Hamiltonian, i.e. the magnetic interaction energy $\left\langle -\overline{E}_h A_z P_z \right\rangle$, which typically exceeds -200 MeV per electron.

There are effects from electromagnetic induction, which contribute to the (dynamic) stability of a CP: As can be seen from Table 3 the magnetic flux decreases with decreasing densities. However, **in the absence of resistive losses the magnetic flux in a plasma is conserved** upon geometric changes. Therefore, magnetic induction will accelerate the electrons in axial direction, such that the flux stays constant upon elongation. The resulting formation energy of a CP elongated from higher densities will be higher than the computed formation energies at low densities in Table 3.

Unfortunately, the effects from flux conservation are not strong enough to fully explain the observed metastability of CPs.

In summary, the length stability has not been proven with the current modeling. In consequence it is uncertain, at which densities CPs are most stable. Unfortunately, most other parameters are depending on the density chosen for the simulation.

Arguments exist, why the resistive losses in a CP at low or moderate temperatures are expected to be extremely small:

Small-angle scattering of the electrons would need to occupy higher-energy orbitals or would result in orbitals, which are already occupied. Thus one can say that small-angle **scattering is** quantum mechanically **suppressed**.

Large-angle scattering (such as the reflection of electrons by the core nuclei) is also suppressed, because the resulting orbitals would run in negative z-direction. The resulting eigenvalues would be higher than before the reflection, i.e. the reflection will not occur.

Only at very high temperatures (above hundreds or thousands Kelvin) there will be sizable electron-phonon scattering (both, small-angle and large-angle). Some of the resulting eigenstates will have negative axial velocities. These electrons will be repelled from the CP by the electric field (i.e. they will be lost). In other cases the resulting eigenstates will relax back (under electromagnetic radiation) to the lower-energy eigenstates, which were populated before the scattering occurred.

Interestingly, the electrons, which will be accelerated in positive z-direction, cannot relax back to lower velocities, because linear movement of charges doesn't radiate. In effect, very high temperatures in the core can increase the mean axial velocity of the electrons.

In order for the model proposed here to account for stable CPs, the resistive loss will need to be very low. The reasons given above are thought to be plausible as to how this might come about. However, further analysis or experimentation would be required for clarification.

If the resistive losses are indeed very small, the magnetic flux of a CP is expected to be virtually constant in a sub-millisecond timeframe. Over a longer time span the flux can potentially change slowly (in both directions, depending on the external conditions).

For a CP to decay, the axial movement of the electrons has to slow down. This, however, takes a long time because of the said lack of electron scattering and because the magnetic flux can change only very slowly.

6 Predictions and Experimental Evidence

A theory, at best, is only as good as its predictive value.

In the following a number of predictions will be derived from the theory on CPs. Many, but not all, of the prediction are already backed by experimental evidence. Those predictions, which are not yet backed by experiments, could become proof points for verifying/falsifying the theory on CPs.

Also, the predictions offer themselves as a detailed guidance for technical implementations of LENR energy reactors.

6.1 Elements Working as LENR "Fuel"

CPs are bring atomic nuclei to unusually short distances in the order of 2 to 15 pm. In this environment tunneling of nuclei through the Coulomb barrier becomes probable.

It is predicted that the tunneling is not limited to specific elements. Therefore, all sorts of elements can react in LENR, not merely hydrogen and transition metals.

This prediction is already backed by experimental evidence:

- The device built by Alexandra und Paulo N. Correa using pulsed anomalous glow discharge (PAGD) was releasing excess energy from just aluminum electrodes and maybe some air [20] [21].
- Gerald L. Wendt & Clarence E. Irion produced helium by decomposition of tungsten via high-current discharges. No hydrogen was present in the experiments. See chapter 1.13.
- George Ohsawa observed the transmutation of carbon and oxygen into silicon and iron by arching between carbon electrodes in air [25].
- A. B. Karabut ignited glow discharges in low-pressure D_2, H_2, Kr and Xe gases with cathodes made of Al, Sc, Ti, Ni, Nb, Zr, Mo, Pd, Ta, W and Pt. He observed characteristic X-ray emissions, excess heat and gamma emissions with all gases and metals (the strongest emission was with deuterium and palladium). The results suggest that hydrogen is not strictly required for LENR [30].

6.2 LENR Reaction Products

Chapters 1.8, 1.9 and 1.10 provide examples of the many possible reaction routes in LENR.

It is predicted that the byproducts of the LENR reaction can be virtually any element in the periodic table, not merely helium. This prediction is depending on the validity of the hypotheses in chapters 1.8, 1.9 and 1.10.

This prediction is already backed by experimental evidence: T. Matsumoto, Tadahiko Mizuno, George H. Miley, Yasuhiro Iwamura, and others [26] [27] [28] [29] discovered that LENR devices are producing a wide range of elemental transmutations. Some of the created elements were lighter and some were heavier than the originating elements.

6.3 Fast Electron Emission, Lack of Ion Emission

The core of a CP always has a negative potential. Electrons, which are escaping out of the core (because their axial velocities have dropped below the critical limit), will be accelerated away from the core by the repulsive core potential.

It is therefore predicted that CPs are emitting electrons with kinetic energies with kinetic energies up to tens of keV.

In contrast, nuclei diffusing out of the CP will be attracted by the core potential. It is therefore predicted that cations coming out of a CP will have practically no kinetic energy and will recombine with electrons in the vicinity of the CP.

There is experimental evidence in the writings of Ken Shoulders that there is indeed electron emission from EVs (i.e. CPs). The most conclusive findings were stemming from his pinhole camera experiments [19]. Also, he found out that dielectric surfaces, which came in touch with CPs, were negatively charged afterwards as a result of the electron emission.

In contrast, Ken Shoulders couldn't detect any ion emission from the CPs, even under high amplification measurements.

Nonetheless, nuclei with several MeV of energy can be emitted from CPs as a result of nuclear reactions (spallation products). In most cases these are protons and alpha particles. Compared to the emission of electrons, the spallation radiation is very infrequent, though.

6.4 CP "Death Knell" Signature

CPs contain a repository of kinetic energy, which will be suddenly released, when the intrinsic current of the CPs stops and the nuclei and electrons recombine to ordinary atoms and molecules. This means that CPs will eventually bust, either by disruptions from external causes or by their normal decay.

It is predicted that when a CP busts, a very specific signature of time-correlated radiation/signals can be measured. This signature includes:

- Sound: A sharp click occurs, when the CP transitions from its high matter density to the lower density of ordinary matter
- Radio frequency emission: A wide-band radio frequency "click" occurs, resulting from the sudden disappearance of the CP's magnetic moment
- Light and X-ray emission: When the electrons escape from their magnetic trap they will scatter and decelerate, leading to broad-band bremsstrahlung. The nuclei will then recombine with electrons, which is causing a line spectrum from X-ray through UV to light emission.

All types of emissions from this signature will occur synchronously in a very short time period.

There is not yet experimental evidence in the literature about this "death knell" signature of CPs. In practice, it should be possible to build a CP detector/counter, which time-correlates the signals of said signature.

6.5 Cathode Erosion, Anode Deposition

A CP emitted by a cathode requires electrons and nuclei to form. It is predicted that not merely the electrons, but to a certain degree also the nuclei have to come out of the cathode. Therefore the cathode will erode at the point of CP emission, leading to craters in the surface.

It is further predicted that the cathode nuclei can travel in the CP and can be deposited as a little droplet on the anode.

Additional corrosion at the cathode will occur, if closed-loop CPs are attaching themselves for some time to the surface of the cathode. This is further described in chapter 6.6.

There is experimental evidence for this phenomenon from several sources:

- Ken Shoulders has described the erosion of the cathode tip by EVs/CPs [2].
- It has been observed and documented by the Correas in [21]
- The presentation produced by Klimov A. et al. in 2017 [31] provides very clear photographic evidence for the cathode erosion, the anode deposits and the path of the CPs on their ways from the anode to the cathode through the plasma
- In 2007 W.-S. Zhang and J. Dash [32] published a document showing the craters on the surface of a palladium cathode after electrolysis in heavy water

6.6 Erosion of All Materials, No nuclear reactions in Crystal Lattice

It is predicted that all materials, which are coming in contact with CPs, will be eroded. The erosion is the result of ionization and re-condensation of the matter surrounding the CPs. Most of this ionization is based on the strong electric field between the core and the halo of CPs.

It is predicted that no nuclear reactions can occur in the crystal lattice, because nuclear reactions would require the presence of CPs and CPs would destroy the lattice by ionization.

There is experimental evidence from many sources that CPs can cause patterns and craters on surfaces by erosion [1] [2] [6] [21] [31] [32].

No experimental evidence in known to the author, which would prove that nuclear reactions can occur in the lattice. The absence of evidence is significant, because the prevailing assumption of the Fleischmann paradigm is that the fusion occurs in the lattice.

6.7 Intrinsic Current, Magnetic Moment, Pseudo-Ferromagnetism

It is predicted that CPs always have an intrinsic axial current. The magnetic field of this current is strong enough to bend the CPs to a helical shape.

It is predicted that the helical shape in combination with the intrinsic current is in most cases leading to a strong magnetic dipole moment of CPs. The exception of this rule occurs, if CPs have a secondary structure like a toroid coil. In this case the magnetic field lines of the CPs are internally closed and no external magnetic moment can be measured.

It is further predicted that the magnetic moments of CPs are aligning in an external magnetic field, such that the strength of the external magnetic field is increasing.

It is predicted that this "pseudo-ferromagnetism" will persist even at very high temperatures, way above the Curie temperature of all known ferromagnetic substances.

Some anecdotal evidence has been reported that CPs are increasing an externally applied magnetic field. For example, T. Matsumoto reported [39] that a platinum wire tips became magnetic after having absorbed CPs. More systematic measurements have to be made to fully back these predictions.

6.8 Broad-Band Electromagnetic Radiation Stemming from Electrons

It is predicted that most of the electromagnetic radiation of CPs is stemming from the electrons, rather than from excited nuclei.

It is further predicted that CPs are causing broad-band emissions because of the density and delocalization of the electrons.

There are measurements available [30] [31] in support of this claim. The measured spectra are additionally showing some emission lines from ordinary atoms of the surrounding matter.

The very sharp gamma lines, which are typical of excited nuclei, are normally not found in LENR emission spectra. The exception of this rule is based on the death knell signature described in chapter 6.4.

6.9 Directed X-Ray Radiation in Parallel to Magnetic Field

The secondary structure of CPs is often quasi-periodic (helical). CPs in these cases can act like a free-electron laser.

It is predicted that CPs can emit collimated laser-like pulses of x-ray and UV radiation.

It is further predicted that the laser pulses are directed in parallel to the magnetic field lines.

Laser-like x-ray pulses have been observed by Karabut [30].

Evidence is not yet available that the collimated x-ray pulses will be directed in parallel to an externally applied magnetic field.

6.10 Triggering Energy, Non-Spontaneous Formation

It is predicted that the formation of CPs is requiring triggering energy in form of a strong current pulse through a plasma. This means, CPs cannot form spontaneously, e.g. in hydrogen-loaded metals.

The many negative results in LENR history from attempts to replicate certain experiments can be attributed to a lack of such triggering energy.

6.11 Preference to Surfaces

It is predicted that CPs can electrostatically attach themselves to surfaces.

There is a wealth of evidence from Shoulders, Savvatimova and others for this phenomenon [1] [2] [6] [7] [16].

6.12 Nuclear Energy Feedback, Self-Sustained Growth, Negative Resistivity

It is predicted that CPs can have a negative resistivity during the acceleration phase, they can grow their length and they can sustain their lifetime, if the right external conditions are met, such as:

- Nuclear fuel is available and can diffuse into the CPs
- Fast electrons are available in the surrounding matter
- Cations are available in the surrounding matter

This prediction is depending on the validity of the nuclear energy hypothesis in chapter 1.13.

There is anecdotal evidence available from several sources, including Francesco Piantelli, Andrea Rossi, Sergey Tsvetkov and others that LENR reactors can temporarily enter a self-sustained mode, where the heat production requires no input energy.

There is experimental evidence available from the Correas and from Anatoly Vachaev that the negative resistivity of CPs can cause sustained high-voltage oscillations in the connected electrodes with no external energy supply.

More experimental evidence needs to be produced in order to conclusively correlate the self-sustained episodes with the above conditions and to prove the nuclear feed-back mechanism.

7 LENR Technology Assessment

When LENR will finally hit the market, it will be disruptive to many established businesses and power structures. One can expect fierce resistance from established forces against a quick adoption of this powerful technology. The political and economic dimensions of LENR are certainly worth a detailed analysis. However, this is beyond the scope of this document.

In the following an attempt is made to assess the potential dangers of the future market adoption of LENR. Only those aspects will be assessed, which can be derived from the physical properties of CPs.

7.1 Can LENR be Weaponized?

At the beginning of LENR research there was no way to judge upon the dangers of LENR as a potential "low-cost hydrogen bomb". In light of the theory on CPs this prospect seems to be an unlikely development:

- CPs cannot be stored safely for longer periods of time. They have instead to be produced at the time of their use.
- CPs cannot be produced in large quantities, without spending a lot of electrical energy in their creation. This would render the sudden amassing of CPs for achieving an atom-bomb-scale destruction rather impractical.

However, LENR can be used for generating a smaller-scale explosion by charging a large bank of capacitors with high voltage and switching this charge to a thin wire or spark gap mounted under water. An underwater arc will occur and the current will produce CPs, which is releasing nuclear energy. The nuclear energy will cause radiolysis of the surrounding water, forming compressed HHO gas, vapor and heat. There can be additional amounts of hydrogen and helium stemming from spallation products (i.e. fast protons and alpha particles). The rest of the water will be forcefully driven aside with high velocities [35].

The rapidity of the energy release from such underwater arc explosions is surprising, because the energy release is the result of tunneling (of nuclei through the Coulomb barrier). Tunneling is a probabilistic process and the reaction is rate-limited by the tunneling probability of the nuclei.

So yes, LENR can be weaponized, but the technology looks inferior compared to the established explosives.

7.2 Will LENR Reactors Produce Dangerous Waste and Radiation?

From the past experience with LENR, there are almost no radioactive remains from the reaction. Some spurious amounts of tritium and some neutrons have been detected under some "abnormal" conditions.

A mixture of all sorts of elements is created by LENR. Some of these elements are toxic and need to be recycled or deposited with care.

In light of the theory on CPs there are two different outcomes from two different cases:

The first case is a LENR reaction with long-living CPs. This case will typically be found in devices, where the self-sustained growth of CPs is effective. This mode is desirable, because it produces practically no radioactive residues, no

hard x-rays and no gamma radiation. The CPs stay intact long enough that the nuclear energy is "cooled away" by the electrons.

The second case can be observed in plasma focus devices. These devices are optimal for the sudden creation of very many CPs, which will be smashed against the anode and destroyed. This mode of LENR operations will cause significant amounts of hard x-ray and gamma radiation, as well as neutrons. It also produces long-living radioactive isotopes. In this mode of operations the CPs don't live long enough to provide proper "cooling" of the excited nuclei. The hard x-rays are stemming from bremsstrahlung emitted during the destruction of the CPs.

In summary, the design of a LENR device needs to be optimized for the longevity of CPs, if one wants to reduce unwanted radiation and radioactive waste.

LENR devices with a high energy output are producing intense amounts of soft x-rays and vacuum UV radiation. Shielding against this radiation is an absolute requirement for protecting people against health hazards.

LENR devices can produce strong electromagnetic pulses, i.e. radio-frequency emissions. Without proper shielding, the devices would disturb wireless communications and delicate electronics.

LENR devices of all kinds will create and potentially emit CPs (previously dubbed "strange radiation"). These emissions should not be called "radiation", because it is not corpuscular or electromagnetic. LENR devices have to be properly shielded against CP emissions, because CPs are harmful to biological tissue and pose a serious health risk. They are also destroying electronics and might have other unwanted effects to all sorts of material. Please refer to chapter 1.5 for advice on shielding against CPs.

As a precaution against neutron emissions one should avoid neutron-rich isotopes as LENR fuel, i.e. ^{7}Li, ^{9}Be, ^{11}B and elements heavier than zinc (including palladium). As can be seen from equations (40), (42), (44), (58) and (59) spallation and fission can liberate neutrons. Deuterium is not merely more neutron-rich than protium, but fusion with deuterium also increases the likelyhood of subsequent spallation/fission due to the larger reaction energy. In this regard protium is preferable over deuterium for LENR applications.

In summary, there are some ecological and health dangers from LENR. In comparison to the monstrous radioactive inventory of a fission reactor or the dangers from CO_2-based climate change, the dangers from LENR seem to be manageable. More experience will be needed to fully judge upon the possible risks of LENR.

7.3 Can LENR Lead to Run-Away Reactions with Explosions and Meltdown?

According to the nuclear feedback hypothesis in chapter 1.13 LENR can enter run-away conditions with uncontrolled and sudden release of large amounts of nuclear energy.

Several cases of (rare) accidents have been reported:

- At the beginning of 1985 Fleischmann and Pons electrolyzed a one-centimeter cube of palladium in heavy water with 1.5 A of current. According to eye witness Kevin Ashley (as quoted in [42]), who was a graduate student of Pons, the experiment exploded over night. He saw the shambles and a particular dust in the air. The lab bench, which was made of very hard material, had a hole of about one foot in diameter. Under the hole was a pit in the concrete floor, which was about four inches deep. Fleischmann and Pons reported in their Preliminary Note, ". . . a substantial portion of the [palladium] fused (melting point 1,554C), part of it vaporized, and the cell and contents and a part of the fume cupboard housing the experiment were destroyed."
- In [40] there is a thorough analysis by Tadahiko Mitsuno and Yu Toriyabe of a LENR explosion. The explosion was occurring during electrolysis of a 0.2 molar K_2CO_3 solution (700 cc) with a platinum mesh anode and a tungsten cathode wire 1.5 mm in diameter, 29 cm long, 3 cm exposed to the electrolyte, input voltage 15 V and input current 1.5 A. The estimated heat output was 800 times higher than input power, based on the data recorded up to the moment of the event. There were many elements deposited on the electrode surface. The major elements were Ca and S.
- There were reports from Andrea Rossi and eye witnesses that some of the high-temperature E-Cat ("Hot-Cat") reactors were destroyed by meltdown events. This was more likely to happen at the beginning of the excess heat production, especially if the reactor was started too fast (and the $LiAlH_4$ fuel was still fresh, the author supposes).

It would be a bad mistake to dismiss these reports as sensationalism. LENR experiments can be dangerous, if the experimenter does not understand the possibility of self-sustained CP growth and uncontrolled electrical oscillations in the electrodes. The common pattern in the said accidents was that plenty of nuclear fuel was present in the experiment in direct contact with the CPs and that the experimenters didn't see a necessity to provide resistive damping to the electrode circuitry.

The reported main reaction products of the Mitsuno-Toriyabe incident are a valuable hint of what had happened: The reported reaction product "sulfur" could have been produced by O-O fusion according to equation (6). The reaction

product “calcium” could have been produced by H-K fusion according to equation (50). In other words: The explosion was probably fuelled by the electrolyte rather than by reactions at the tungsten cathode.

Generally, **it is not advisable to perform LENR electrolysis**, because usually the amount of water in such experiments is large enough to produce dangerous damages in case of a reaction excursion.

Fleischmann and Pons concluded from the accident that they had to reduce the size of their palladium cathodes to very small volumes. This was understandable, because they believed the reaction was occurring in the volume of palladium. However, this precaution is not sufficient: The nuclear reaction can be sustained by both, the PdD and the D_2O (or water, in general).

Water is also problematic in that it can suddenly produce large volumes of hydrogen (by radiolysis) and steam, which was causing the forces to shatter the above experiments.

Also at reactors with fuel powder mixtures, the amount of fuel is typically not limited to the immediate needs to create the desired output power. The CP growth in these reactors cannot be safely controlled merely by regulating the working temperature to always limit the energy production in the desired way.

The reported melting of the E-Cats may have been “pseudo-melting”, caused by ionization by CPs in addition to thermal damage.

A much safer way of building LENR reactors is to use low-pressure gas as fuel. The electrodes and construction materials should be made of materials, which do not sustain nuclear reactions in the absence of the gas fuel. Iron and nickel or alloys thereof would suffice in this regards. In case of emergency the fuel gas could be flushed away from the electrodes by argon or krypton.

Generally, **in order to build safe LENR reactors one has to ensure that the reaction rate is fuel-limited and the electrode circuitry is damped by an appropriate resistor** under all possible conditions.

8 Summary and Conclusions

Previously known as “charge clusters”, “EVs”, or “strange radiation”, a novel aggregation state of matter has been characterized and named “condensed plasmoids”. A quantum-mechanical model of CPs was built, a computer program was designed, and computer calculations were used to obtain the properties of CPs.

The computed properties are well-aligned with many experimental findings in LENR, including the strange patterns left by CPs on the surfaces of electrodes and x-ray films.

CPs are compressing matter magnetically to such high densities that atomic nuclei can tunnel through the Coulomb barrier, thereby enabling fusion.

Gamma rays of fusion-excited nuclei are suppressed by the high current density inside of CPs via near-field interactions. The nuclear energy is “down-converted” to many electrons ending as heat.

Possible routes of the nuclear reactions have been explored. There are many ways to explain the generation of helium-4 from deuterium and other “fuel” elements, without assuming d-d fusion. If the proposed hypotheses will turn out to be true, they are solving the most puzzling questions of LENR research.

This document derives verifiable predictions from the theory on CPs. It assesses potential dangers of LENR and proposes shielding mechanism required for the safe operation of these devices.

The current modeling is seen as being incomplete, because no length stability of CPs was found and because the calculated intrinsic current of CPs appears to be larger than what can be concluded from the experiments. This is probably caused by inaccuracies in the relativistic Hamiltonian. There is a remote possibility that CPs are superconducting, which would be an alternate route for completing the theory.

LENR reactors can be dangerous, if they are not well-designed. The main sources of danger are x-ray and UV emissions, direct exposure to CPs, uncontrolled and sudden release of energy via self-sustained CP growth or uncontrolled electrical oscillations.

Hopefully, the theory on CPs will reinvigorate the scientific discourse between research groups, startup companies and other organizations, which lately were working on their patents and LENR reactor designs in an understandably closed-lipped fashion. Without an open scientific dialogue on CPs however, the completion of this theory cannot be achieved.

May the theory on CPs be instrumental in the technical development of *reliable, durable and safe* LENR reactors and a timely commercialization.

9 Acknowledgements

Edward H. Lewis had put forward the hypothesis that atoms can enter a previously unknown state of matter, in which they behave like ball lightning, and which is an intermediate state of the LENR reaction. This view turned out to be so right! The author owes his original inspiration about CPs to the comprehensive collection of microscopic, experimental and natural evidence published by Ed Lewis in [10] and [11].

It was of tremendous value to the author's research having had access to the vast library of original literature at len-canr.org. The author is thankful to the researchers for their dedication and effort and the International Society for Condensed Matter Nuclear Science for maintaining their media.

The theory on Condensed Plasmoids is seen as a continuation of the pioneering work of Winston Bostick's work on vortex filaments in plasma focus devices and Ken Shoulders' work on charge clusters. The author is deeply indebted to the ingenuity, insight and dedication of the late Ken Shoulders.

The kind and competent support of Peter Hagelstein was much appreciated, as it helped the author to avoid some mistakes regarding the intricacies of relativistic quantum mechanics.

The author is thankful to Paulo and Alexandra Correa for having invented, built, analyzed, patented and documented the most wonderful LENR reactor [20][21].

10 Appendix

Numerous cold fusion experiments have shown strong evidence for transmutations occurring alongside excess heat production. As shown below in Figure 76, Figure 77 and Figure 78, all sorts of different elements are created by cold fusion:

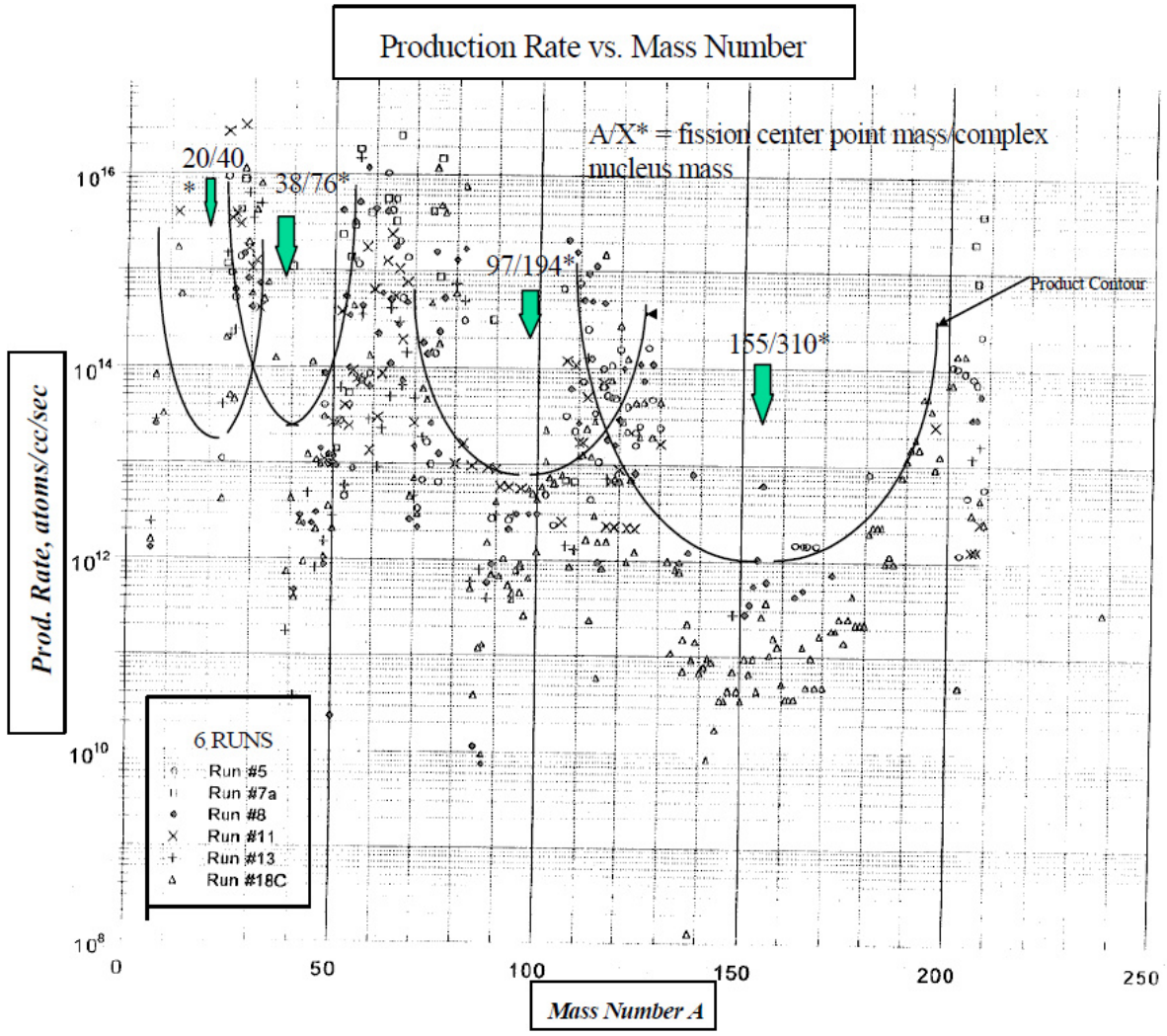

Figure 76 Pd-Ni thin film light water electrolysis experiments, George H. Miley [26][27]

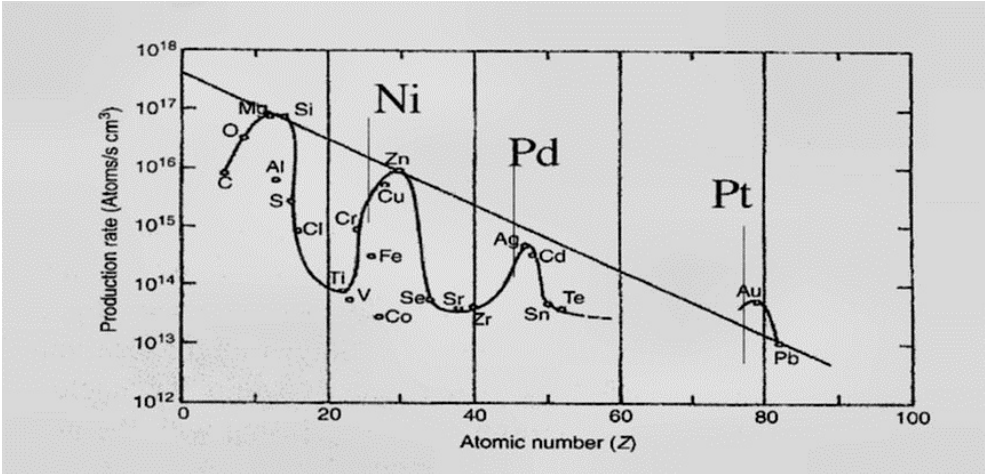

Figure 77 Miley's Ni-H_2O experiments [29]: Reaction product yield vs. atomic number

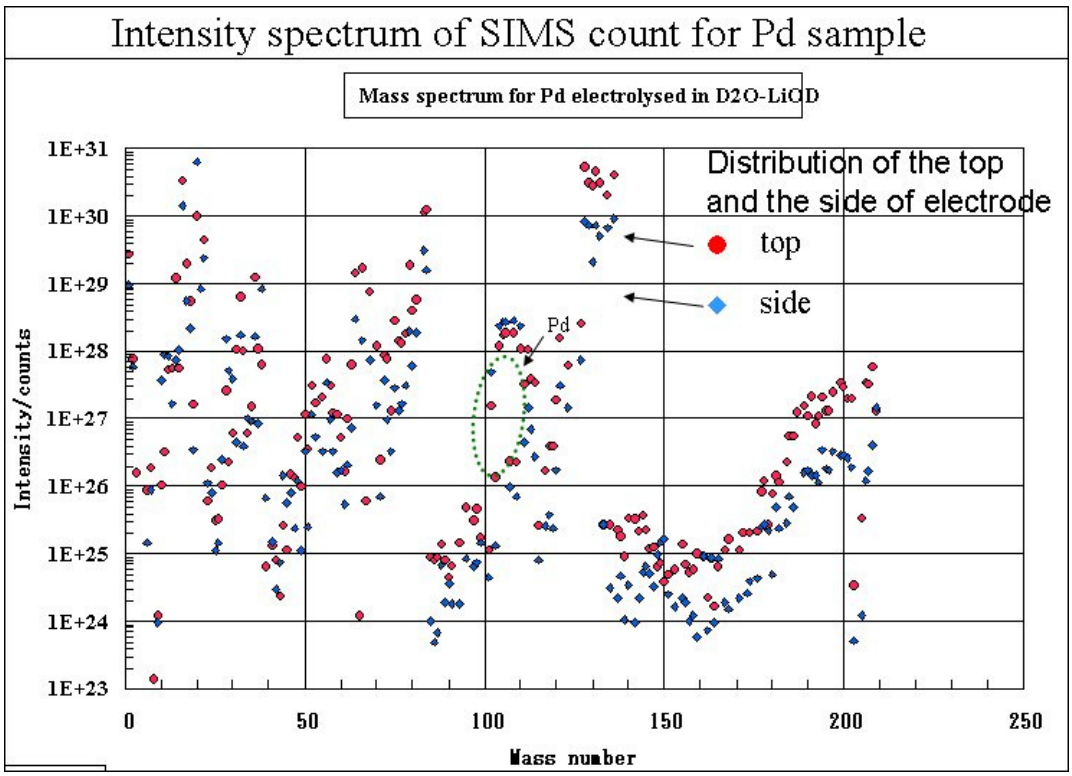

Figure 78 Mass Spectrum of Palladium electrolyzed in D_2O-LiOD, Tadahiko Mizuno, 2009 [28]

The distribution of element production rates is somewhat similar if one compares nickel-proton reactions with palladium-deuteron reactions. Both, lighter and heavier elements were created starting from nickel or palladium.

In some of the runs as much as 40% of the initial metal atoms of the thin film coating were transmuted, which makes it very unlikely that the observed elements are stemming from "contamination" with impurities during the experiment.

The lighter elements could have been created only by fission (i.e. spallation) of the host material. The heavier elements were most likely created by fusion of the host material with other elements.

11 References

[1] **Shoulders, Ken** and **Shoulders, Steve** 1999: *"Charge Clusters in Action"*, http://www.svn.net/krscfs/Charge%20Clusters%20In%20Action.pdf (currently offline) http://www.keelynet.com/shoulders/charge%20clusters%20in%20action.pdf (a mirror to the same content)

[2] **Shoulders, Kenneth R.** 1987: *"EV – A Tale of Discovery"*, Jupiter Technologies, Austin, Texas, USA

[3] **Boor, Nathan** of Aimed Research 2012: Video showing a bolt of lightning at 6,200 frames per second, creative commons license, http://upload.wikimedia.org/wikipedia/commons/a/ad/Lightning_Trumbull_County_Ohio.ogv

[4] **Storms, Edmund** 2003: *"A Student's Guide to Cold Fusion"*, http://www.lenr-canr.org/acrobat/StormsEastudentsg.pdf

[5] **Storms, Edmund** 2002: *"The Nature of the Nuclear-Active-Environment Required for Low Energy Nuclear Reactions"*, Submitted to Infinite Energy, http://www.lenr-canr.org/acrobat/StormsEthenatureoa.pdf

[6] **Rodinov, B. and Savvatimova, Irina** 2005: *"Unusual Structures on the Material Surfaces Irradiated by Low Energy Ions"*, archived at LENR-CANR.org, http://www.lenr-canr.org/acrobat/RodionovBunusualstr.pdf

[7] **Lochak, Georges and Urutskoev, Leonid** 2004: *"Low-energy nuclear reactions and the leptonic monopole"*, in Eleventh International Conference on Condensed Matter Nuclear Science http://www.lenr-canr.org/acrobat/LochakGlowenergyn.pdf

[8] **LeClair, Mark L. and Lebid, Serge**: The document reporting on cavitation-induced LENR used to be at https://nanospireinc.com/Fusion.html, but has been removed from the web. Their new web site is at https://nanospire.com

[9] **Karabut, Alexander B.** 2004: *"Research into Characteristics of X-Ray Emissions Laser Beams from Solid-State Cathode Medium of High-Current Glow Discharge"*, ICCF-11, http://lenr-canr.org/acrobat/KarabutABresearchin.pdf

[10] **Lewis, Edward H.** 2008: *"Traces of Ball Lightnings in Apparatus"*, Unconventional Electromagnetics and Plasmas, 1&2, 89-97, http://www.lenr-canr.org/acrobat/LewisEtracesofba.pdf

[11] **Lewis, Edward H.** 2008: *"Evidence of Ball Lightning – A Survey of Some Recent Experimental Papers Describing Microscopic Objects Associated with Transmutation Phenomena"*, ICCF-14, http://www.lenr-canr.org/acrobat/LewisEevidenceofb.pdf

[12] **Robert A. Nelson**: *"The Transmutation of Hydrogen to Helium & Neon"*, Adept Alchemy, Part II. Chapter 6 http://www.alchemywebsite.com/nelson2_6.html

[13] **Schakhparonov, I. M.** and **Evstigneev, N. M.** 2012: *"Mechanism of Artificial Ball Lightning Generation by Undirected Möbius Strip Circuit"*, Proceedings '12th International Symposium on Ball Lightning' and '5th International Symposium on Unconventional Plasmas', http://www.belres.ru/data/documents/big012.pdf

[14] **Geneste, Jean-François** 2015: *"LENR: from experiment to theory"*, 11th International Workshop on Anomalies in Hydrogen Loaded Metals, Airbus, Toulouse, http://www.iscmns.org/work11/23%20Geneste%20LENR%20from%20experiment%20to%20theory.pdf. This document shows a high-resolution image of a CP, which was originally presented at the EADS colloquium in 2010 by Claude Daviau, Didier Priem and Guillaume Racineux

[15] **Davis, Eric W.** 2003, *"Ball Lightning Study"*, Final Report AFRL-PR-ED-TR-2002-0039, Air Force Research Laboratory, Air Force Materiel Command, Edwards AFB, CA. http://documents.theblackvault.com/documents/weather/AFRL_2002-0039_Ball_Lightning_Study.pdf This originally secret document was released under the US Freedom of Information Act.

[16] **Daviau, Claude; Fargue, Daniel; Priem, Didier; Racineux, Gulliaume** 2013: *"Tracks of magnetic monopoles"* Annales de la Fondation Louis de Broglie, Volume 38 http://aflb.ensmp.fr/AFLB-381/aflb381m778.pdf

[17] **Jaitner, Lutz** 2015-2019: *"The Physics of Condensed Plasmoids and Low-Energy Nuclear Reactions (LENR)"*, the author's web site
http://condensed-plasmoids.com

[18] **Jaitner, Lutz** 2016-2019: *"CP Simulator"*, online program
https://condensed-plasmoids.com/dyn?cmd=retrieve_simulation_form

[19] **Jaitner, Lutz** 2016-2019: *"History of Condensed Plasmoids and LENR"*,
http://condensed-plasmoids.com/history.html

[20] **Correa, Alexandra and Paulo N.** 1996: *"Direct Current Energized Pulse Generator Utilizing Autogenous Cyclical Pulsed Abnormal Glow Discharges"*, US-Patent 5,502,354",
http://aetherometry.com/Patents/US5502354A1.pdf

[21] **Correa, Alexandra und Paulo N.** 1993: *"Metallographic & Excess Energy Density Studies of LGEN^{TM} Cathodes Subject to a PAGD Regime in Vacuum"*, Labofex Technical Report S1-007
http://www.aetherometry.com/publications/free/LS1-07.pdf

[22] **Wendt, G. L. and Irion, C. E.** 1922, Amer. Chem. Soc. 44

[23] **Stephanakis, S. et al.** 1972, Phys. Rev. Let. 29, 568

[24] **Young, F. et al.** 1977, J. Appl. Phys. 48, 3642

[25] **Ohsawa, George and Kushi, Michio** 1964: *"Transmutations of Carbon"*,
http://www.alchemywebsite.com/nelson2_3.html

[26] **Miley, George H. and Patterson, James A.** 1996: *"Nuclear Transmutations in Thin-film Nickel Coatings Undergoing Electrolysis"*, Journal of New Energy,
http://www.newenergytimes.com/v2/library/1996/1996MileyG-XMT-ThinFilmNickel.pdf

[27] **Miley, George H.** 1997: *"Possible Evidence of Anomalous Energy Effects in H/D-Loaded Solids – Low Energy Nuclear Reactions (LENRs)"*, Journal of New Energy

[28] **Mizuno, Tadahiko** 2009: *"Isotopic changes of elements caused by various conditions of electrolysis"*, presented at American Chemical Society

[29] **Srinivasan, Mahadeva; Miley, George; Storms, Edmund** 2011: *"Low Energy Nuclear Reactions: Transmutations"*, Preprint of review article distributed to participants of ICCF-16 Conference,
http://lenr-canr.org/acrobat/Srinivasanlowenergyn.pdf

[30] **Karabut, A. B.** 2006: *"Experimental Research on 0.5 - 10 keV High-Energy Process Resulting from H2 and D2 Ions Flux Interaction with Cathode Solid in Electric Discharge"*, 7th International Workshop on Anomalies in Hydrogen/Deuterium-Loaded Metals
https://lenr-canr.org/acrobat/KarabutABexperimentb.pdf

[31] **Klimov, Anatoly I., Belov N., Tolkunov B., Chistolinov A.** 2017, *"Interaction of Hydrogen Atoms and Ions with Erosive Metal Clusters in Heterogeneous Plasmoid"*, 12th IWAHLM, Italy,
http://www.iscmns.org/work12/KlimovAinteractionof.pdf

[32] **Zhang, W.-S.** and **Dash, J.** 2007: *"Excess Heat Reproducibility and Evidence of Anomalous Elements after Electrolysis in Pd/D2O+H2SO4 Electrolytic Cells"*, 13th International Conference on Condensed Matter Nuclear Science,
http://www.lenr-canr.org/acrobat/ZhangWSexcessheat.pdf

[33] **Nardi, V.; Bostick, Winston H.; Fenglas, J.; and Prior, W.** 1980: *"Internal structure of electron beam filament"*, Physical Review A, vol. 22, pp. 2211-2217
https://sci-hub.tw/10.1103/PhysRevA.22.2211

[34] **Mizuno, Tadahiko** 2017: *"Observation of Excess Heat by Activated Metal and Deuterium Gas"*, Journal of Condensed Matter Nuclear Science 25 1–25
http://lenr-canr.org/acrobat/MizunoTpreprintob.pdf

[35] **Graneau, Peter** 1997: *"The amazing discovery of Cold Fog Explosions - Extracting Intermolecular Bond Energy From Water"*, Proceedings of the Fourth International Symposium on New Energy,
http://www.infinite-energy.com/images/pdfs/GraneauIE13-14.pdf

[36] **Fredericks, Keith A.** 2015, *"Possibility of Tachyon Monopoles Detected in Photographic Emulsions"*. Journal of Condensed Matter Nuclear Science 15, pages 203-230, http://lenr-canr.org/acrobat/BiberianJPjcondensedn.pdf (short version)

[37] **Fredericks, Keith A.** 2013, *"Possible detection of tachyon monopoles in photographic emulsions"*, Engineering Physics 6 http://restframe.com/downloads/tachyon_monopoles.pdf (long version)

[38] **Mosier-Boss, Pamela A.; Forsley, Lawrence P.; McDaniel, Patrick J.** 2016: *"Investigation of Nano-Nuclear Reactions in Condensed Matter – Final Report"*, Defense Thread Reduction Agency, http://lenr-canr.org/acrobat/MosierBossinvestigat.pdf

[39] **Matsumoto, Takaaki** 1995, *"Cold Fusion Experiments Using Sparking Discharges In Water"*, ICCF-5 Proceedings, page 390, http://lenr-canr.org/acrobat/PonsSproceedinga.pdf

[40] **Matsumoto, Takaaki** 1995, Bulletin of the Faculty of Engineering, Hokkaido Univ. No. 175, 73

[41] **Mitsuno, Tadahiko and Toriyabe, Yu** 2005, *"Anomalous energy generation during conventional electrolysis"*, http://lenr-canr.org/acrobat/MizunoTanomalouse.pdf

[42] **Beaudette, Charles G.** 2002, *"Excess Heat: Why Cold Fusion Research Prevailed"*, Oak Grove Press LLC, Second Edition

[43] **Levi, Giuseppe; Foschi, Evelyn; Höistad, Bo; Pettersson, Roland; Tegnér, Lars; Essén, Hanno** 2014: *"Observation of abundant heat production from a reactor device and of isotopic changes in the fuel"*. This document has been leaked to the public. It is circulating under the name *"Lugano report"* of the Rossi E-Cat. https://thenewfire.files.wordpress.com/2016/05/lenr_ecat_rossi_lugano_report.pdf

[44] **Sadowski, M. J.** 2006, *"Formation and role of filaments in high-current discharges of the pinch type"*, Czechoslovak Journal of Physics, https://www.researchgate.net/publication/225885113_Formation_and_role_of_filaments_in_high-current_discharges_of_the_pinch_type

[45] **Bogdanovich, B. Yu. *et al.*** 2019, *"Video Recording of Long-Lived Plasmoids near Objects Exposed to Remote and Direct Effects of High-Current Pinch Discharges"*, Technical Physics Vol. 64, No. 4, pp. 465–469, Pleiades Publishing, Ltd., http://sci-hub.tw/10.1134/S1063784219040066

[46] **Vachaev, Anatoly**, *Energoniva Reactor*, https://blog.synthestech.com/achievements-of-russian-scientists-that-can-change-the-world-from-the-cradle-of-lenr-to-modernity-592bbcbd5207 https://www.lenr-forum.com/forum/thread/4802-energoniva-a-water-plasma-transmutation-technology-from-russia/

[47] **Bennett, W. H.** 1934, *"Magnetically Self-focusing Streams"*, Phys. Rev. 45, 890

[48] **Pease, R. S.** 1957, *"Equilibrium Characteristics of a Pinched Gas Discharge Cooled by Bremsstrahlung Radiation"*, Proc. R. Soc. London Ser. B, 70, 11–13

[49] **Braginskii S. I.** 1957, *"On the Behavior of a Completely Ionized Plasma in a Strong Magnetic Field"*, Zhur. Eksptl'. i Teoret. Fiz. 33 645

[50] **Braginskii, S. I.** 1957, *"Contribution to the Theory of Spark Channels"*, Sov. Phys. JETP, 6, 494–501

[51] **Cohen, Robert S.; Spitzer, Lyman; McR. Routly, Paul** 1950, *"The Electrical Conductivity of an Ionized Gas"*, Physical Review. 80 (2): 230-238, http://ayuba.fr/pdf/spitzer1950.pdf

[52] **Koshelev, K. N.; Pereira, N. R.** 1991, *"Plasma points and radiative collapse in vacuum sparks"*, Journal of Applied Physics 69(10): R21 - R44, https://www.researchgate.net/publication/224546528_Plasma_points_and_radiative_collapse_in_vacuum_sparks

[53] **Va'vra, J. ; Maly J. A.; Va'vra P.M.** 1997, *"Soft X-Ray Production in Spark Discharges in Hydrogen, Nitrogen, Air, Argon and Xenon Gases"*, SLAC-PUB-7683, Nuclear Instruments and Methods in Physics Research Section A: Accelerators, Spectrometers, Detectors and Associated Equipment, Volume 418, Issues 2–3, 1 December 1998, Pages 405-419
https://www.slac.stanford.edu/pubs/slacpubs/7500/slac-pub-7683.pdf

[54] **Mesyats, Gennady A. and Mesyats, V.** 2018, *"The sequence of processes in the ecton cycle of a vacuum arc"*, Journal of Physics Conferences Series **1115** 022020,
https://www.researchgate.net/publication/329212025_The_sequence_of_processes_in_the_ecton_cycle_of_a_vacuum_arc